



Provided by the author(s) and University of Galway in accordance with publisher policies. Please cite the published version when available.

Title	Ship Borne Direct Eddy Covariance Flux Measurements
Author(s)	Landwehr, Sebastian Johannes Heinz-Josef
Publication Date	2015-01-28
Item record	http://hdl.handle.net/10379/4912

Downloaded 2024-04-27T04:17:22Z

Some rights reserved. For more information, please see the item record link above.



Ship Borne Direct Eddy Covariance Flux Measurements

A DISSERTATION SUBMITTED IN ACCORDANCE WITH THE
REQUIREMENTS FOR THE DEGREE OF DOCTOR OF PHILOSOPHY
IN THE COLLEGE OF SCIENCE

by

Sebastian Johannes Heinz-Josef Landwehr



School of Physics
National University of Ireland, Galway

Supervisor: Dr. Brian Ward

January 2015

Contents

Abstract	iv
Declarations	vi
Dedication	viii
Acknowledgements	viii
List of Figures	xv
List of Tables	xxix
1 Introduction and Motivation	1
2 Theory and Literature Review	5
2.1 Introduction	5
2.2 Flux-Profile Relationship	6
2.3 Turbulence Spectra	10
2.4 Model Description of Gas Exchange at the Air-Sea Interface	14
2.4.1 Two-Film Model	15
2.4.2 Surface Renewal Model	18
2.4.3 Bubble-Mediated Gas Transfer	20
2.4.4 Wind speed parameterisation	21

2.4.5	Water Side Convection	22
2.4.6	Mean square slope	23
2.4.7	Turbulent Dissipation Rate and Gas Exchange	25
2.4.8	Summary of Transfer Velocity Models and Schmidt Number Scaling	26
2.5	Bulk Flux Formulations	27
2.5.1	The COARE-Algorithm	29
2.6	The Eddy Covariance Method	30
2.6.1	Principle	30
2.6.2	The Air-Sea CO ₂ Flux Package	31
2.6.3	Time Resolution and Averaging Time	32
2.6.4	Spatial Sensor Separation	33
2.6.5	Motion Correction	34
2.6.6	Air-Flow Distortion	34
2.6.7	LICOR Open- and Closed-Path Systems for CO ₂ Flux Measurements	35
2.6.8	Cross Sensitivity to Water Vapour	37
2.6.9	Resolution Requirement for the CO ₂ Sensor	38
3	Field Experiments and Data Analysis	40
3.1	Ship Borne Experiments	41
3.1.1	Knorr11 Gas-Exchange Study in the North Atlantic	41
3.1.2	Surface Ocean Aerosol Production Study (SOAP)	44
3.1.3	SPURS-MIDAS experiment	46
3.2	Flux Data Analysis	47
3.2.1	Motion Correction	47
3.2.2	Stream Line Coordinate System	53

3.2.3	Air Density Correction	53
3.2.4	IRGA-Motion Sensitivity Correction	54
3.2.5	Cross-Covariance and Flux Calculation	56
3.2.6	Scalar Co-Spectra Example	57
3.2.7	Frequency Corrections	58
3.2.8	Calculation of Gas Transfer Velocity	62
4	Development of a New Motion and Flow Distortion Correction	
	Algorithm	63
4.1	Introduction	64
4.2	Theory	71
4.2.1	Parameterisation of the Wind Vector Distortion	71
4.2.2	Height displacement of the air flow	72
4.2.3	Motion Correction and Rotation into the mean flow	74
4.3	Methods	77
4.3.1	Quality Control	80
4.3.2	Estimation of the wind vector pitch and roll	82
4.3.3	Estimation of Yaw Bias and Acceleration	86
4.3.4	Correction for Platform Motion and Air Flow Distortion	89
4.4	Discussion of Results	89
4.4.1	Intercomparison of the Bow Mast Wind Speed Measurements	89
4.4.2	Intercomparison of the Bow Mast Fluxes to the Buoy	91
4.4.3	Drag Coefficient and Stress Angle	91
4.4.4	Errors in the Direct Fluxes due to the Standard Motion Correction	98
4.4.5	Effect of the Tilt on the Covariance Spectra	101

4.5	Conclusions for the Motion-Tilt Correction	105
5	Analysis of the PKT correction for direct CO₂ fluxes	108
5.1	Introduction	109
5.2	Experiment and methods	117
5.2.1	Data analysis and flux calculations	119
5.3	Results	120
5.3.1	Primary CO ₂ flux results	122
5.3.2	Application of the PKT Correction	126
5.3.3	Application of the Spectral Correction	129
5.3.4	Humidity Bias and Transfer Velocities	131
5.4	Analysis of the PKT correction	133
5.5	Discussion	137
5.5.1	Humidity Bias - Correcting versus Drying	137
5.5.2	Air-Flow Distortion	140
5.5.3	Residual Humidity Bias after drying	141
5.5.4	High Frequency Attenuation	144
5.6	Conclusions	146
6	Conclusions and Future Work	148
	Bibliography	152
	Bibliography	152
	The Last Page	168

Abstract

Ship borne direct eddy covariance flux measurements of momentum, heat (latent and sensible), and the trace gas CO₂, were conducted during three open ocean experiments. The methods for data analysis and interpretation were adapted from the literature, and reviewed carefully. Two major sources of measurement errors were studied in detail: the air-flow distortion by the platform superstructure and the cross-sensitivity of the CO₂ signal to water vapour. For both topics a revision of the treatment, as suggested in the literature, was found necessary.

Air-flow distortion can lead to a tilt of the wind vector as well as acceleration of the wind speed. Eddy covariance measurements are additionally affected by the platform motion. The classic approach is to first correct for the platform motion and thereafter rotate the wind vector into the mean flow. For moving ships, this causes an over-estimation of the tilt, because the flow distortion-induced vertical velocity is proportional to the relative wind speed. The overestimated tilt leads to biased flux estimates. This may explain the common observation that flux estimates from moving ships have lower quality than measurements taken on station. An alternative method is presented here, where the flow distortion-induced tilt is estimated from the wind speed measurements and applied after correcting for the platform motion, but before removing the ship's mean velocity. This significantly

reduced the flow distortion error in the direct flux measurements.

With respect to CO₂, the flux measurements are affected by cross-sensitivities to water vapour, resulting in order-of-magnitude biases. Well established cause are (i) band-broadening and spectral overlap, and (ii) air density fluctuations. Both can be corrected. A further bias related to humidity fluctuations has recently been observed with the widely used CO₂/H₂O open-path sensors produced by LICOR, attributed to sea salt build-up and water films on the sensor optics. Two different approaches have been used: *Miller et al.* (2010) employed a membrane drier to physically eliminate 97% of the water vapour fluctuations in the sample air before it entered a closed-path gas analyser. *Prytherch et al.* (2010a) formulated the PKT (Peter K. Taylor) post-processing correction. Here these methods are compared using four closed-path analysers, two of which were positioned down-stream of membrane dryers. The CO₂ fluxes from the dried analysers matched each other and were in general agreement with common parameterisations. The measurements from the un-dried sensors agreed only when the humidity flux was low and exhibited order-of magnitude biases otherwise. The PKT correction did not remove the bias. The results demonstrate the validity of measuring CO₂ fluxes at pre-dried air and disprove the PKT correction.

Declarations

The work of this thesis is based on research carried out in the Air-Sea Physics Lab, School of Physics, NUI Galway. No part of this thesis has been submitted elsewhere for any other degree or qualification. This thesis reports my own work, unless referenced differently in the text.

Copyright © 2015 by Sebastian Landwehr. The copyright of this thesis belongs to the author. No quotations from it should be published without the author's prior written consent and information derived from it should be acknowledged.

Dedication

Diese Arbeit ist meinen Eltern Klaus und Hildgard Landwehr gewidmet. Ich bin ihnen unendlich dankbar für ihre bedingungslose Liebe und fortwährende Unterstützung.

Acknowledgements

My thanks go first to my supervisor Brian Ward, for his support and advice throughout the work, for the trust and great freedom I was given, for promoting me where he could and giving me all these marvellous opportunities. Due to various travels we worked at different places about half the time, but Brian was always ready to help, whether he was next door or far away.

I am also very grateful to my fellow PhD students Niall O'Sullivan, João de Almeida, Graig Sutherland, Brian Scanlon, Anneke ten Doeschate, and Leonie Esters, for the fellowship on the long way, on our travels and during the field experiments, and for all the fun we had at and after work.

Thanks to the postdocs Adrian Callaghan, Marc Defossez, Xavier Sanchez-Martin, Danielle Wain, Chiara Uglietti, and Kieran Walesby who joined our group.

Thanks to Giovanni Martucci, Darius Ceburnis, Jurgita Ovadnevaite, Tomas Grigas, for inviting me into their 12:30 lunch and espresso tradition. And for the warm welcome every-time I returned to Galway.

Thanks to my temporary colleagues in GASERA Ltd, Turku, Finland, especially Sauli Sinsalo for the joint suffering, and Juho Uotila for all his help, Jari for his sympathy and the wise counsels and Jukka Nakari for teaching me about 'yes, but no'. Niko, Megha, Ksenia and Gayathri for the light hours in the middle of the dark Finnish winter - kiitti!

Acknowledgements

Thanks to Fritz Sonnichsen for his help during the setup for Knorr11 and for his hospitality.

I am grateful to Scott Miller from the State University of New York at Albany, for teaching me about direct flux measurements and for entrusting me with his instruments; to Chris Sager for the bike, Sergey Kivalov and Matt Czikowsky for the hikes and the tea breaks, Dave and Zane Fitzjarrald for opening their house and hearts.

My thanks go to Murray Smith from NIWA Wellington, New Zealand, for key inputs about Eddy Covariance, and for the ride in his sail boat across Cook Strait that I really enjoyed, despite being sick to the bottom of my stomach for most of the time.

Special thanks to our technician Stuart Harries for his great help with setting up the flux equipment on the R/V *Saramiento de Gamboa*, and for the good company on our unexpected train journey from Vigo to Barcelona.

I also want to acknowledge the scientific teams and crews of the R/Vs *Knorr*, *Tangaroa* and *Saramiento de Gamboa* for the exceptional work they do and for their great support.

Special thanks to Tom Bell, Cyril McCormick from UC Irvine, and Warren deBruyn from Chapman University, whose company I was delighted to enjoy on both cruise Knorr 11 and SOAP.

Thanks to Manuela Hürlimann for cheering me up and on, and inspiring me, for not minding me being quite absorbed in my work at times, and for carefully proof reading each part of this thesis for spelling, grammar and clarity.

My family have supported me and have in many ways contributed to this work. My parents have always encouraged (and endured) my curiosity. They have taught me and my siblings with love and by living examples and take

part in our lives.

Finally I want to say thanks to all the pilots, train and bus drivers, and all the other people involved in the worldwide network of transport systems, without whom this work would never have been possible.

This research was funded by Science Foundation Ireland as part of the US-Ireland R&D Partnership Programme under Grant Number 08/US/I1455 and a SFI Short-term Travel Fellowship under Grant 09/US/I1758-STTF-11, the EU FP7 project CARBOCHANGE under grant agreement no. 264879, US National Science Foundation Award 0851407, and by NIWA under the Ocean-Atmosphere Programme in the Atmosphere Centre.

We would like to thank Tom Farrar at WHOI for making available the buoy data (<ftp://ftp.whoi.edu/pub/users/jfarrar/SPURS/>).

This thesis was written in L^AT_EX.

Sebastian Johannes Heinz-Josef Landwehr

Galway, January 2015

List of Symbols

Symbol	Units	Description
B_w	$\text{m}^2 \text{s}^{-3}$	Water side buoyancy flux
C_D	-	Drag coefficient
C_E, C_H	-	Exchange coefficients of moisture, and sensible heat
C_a, C_w	mol m^{-3}	Air-, and water-side bulk concentration of a trace gas
C_{ai}, C_{wi}	mol m^{-3}	Air-, and water-side concentration of a trace gas at the air-water interface
D_a, D_w	$\text{m}^2 \text{s}^{-1}$	Gas diffusivity in air, and water
F	$\text{mol m}^{-2} \text{s}^{-1}$	Gas flux across the interface
g	m s^{-2}	Acceleration due to gravity
k_a, k_w	cm h^{-1}	Air-, and water-side transfer velocity contribution
K_a, K_w	cm h^{-1}	Overall air-, and water-side transfer velocity
k_i, k_b	cm h^{-1}	Inter-facial, and bubble-mediated transfer velocity
L_*	m	Monin-Obukhov stability length scale
L_{ev}	J g^{-1}	Latent heat of vaporization
P	Pa	Pressure
$Q_{\text{sen}}, Q_{\text{lat}}$	W m^{-2}	Sensible, and latent heat flux
Q_{net}	W m^{-2}	Net surface heat flux

q	kg kg^{-1}	Specific humidity of air
q_*	kg kg^{-1}	MOST scaling parameter for humidity
R	$\text{J mol}^{-1} \text{K}^{-1}$	Ideal gas constant
$R_{l\uparrow}, R_{l\downarrow}$	W m^{-2}	Up-welling, and down-welling long wave radiation
S	m s^{-1}	Scalar time average of the wind speed
Sc	-	Schmidt number (ratio of viscosity and diffusivity)
T	K	Temperature (air)
t_*	K	MOST scaling parameter for temperature
U	m s^{-1}	Vector time average of the wind speed
u_{10N}	m s^{-1}	Average wind speed normalized to a height of 10 meter above the surface and neutral stability
(u, v, w)	m s^{-1}	3 dimensional wind vector
u_*	m s^{-1}	MOST scaling parameter for velocity (air-side friction velocity)
u_{*w}	m s^{-1}	Water-side friction velocity
w_g	m s^{-1}	Gustiness (wind variability) parameter
W_*	m s^{-1}	Convective scaling velocity
W_w	m s^{-1}	Water side convective velocity scale
WCF	%	White cap fraction
x_c, x_v	mol mol^{-1}	CO_2 and H_2O mixing ratio
$x_{c,m}, x_{v,m}$	mol mol^{-1}	Measured CO_2 and H_2O mixing ratio
z	m	Measurement height above ground or above mean sea level
z_0	m	Roughness length
α	-	Charnock parameter
α	°	Relative wind direction

Acknowledgements

α_T, α_S	-	Thermal, and haline expansion coefficients of sea water
δ_ν^w	m	Thickness of the viscous sub-layer (water-side)
ϵ	$\text{m}^2 \text{s}^{-3}$	Dissipation rate of turbulent kinetic energy
$\Phi_\chi \left(\frac{z}{L_*} \right)$	-	Dimensionless stability function of the scalar $\chi = u, T, q$
$\Psi_\chi \left(\frac{z}{L_*} \right)$	-	Integrated form of the stability function $\Phi_\chi \left(\frac{z}{L_*} \right)$ of the scalar $\chi = u, T, q, x_{\text{CO}_2}, \dots$
γ	-	Roughness Reynolds number
ν_a, ν_w	$\text{m}^2 \text{s}^{-1}$	Kinematic viscosity of air, and water
ρ_a, ρ_w	kg m^{-3}	Density of air, and water

List of Acronyms

CR	Cavity ring down (spectrometer)
DMS	Dimethyl Sulfide
DR	Double rotation
DRx	Alternative double rotation
ECMWF	European Centre for Medium-Range Weather Forecasts
IRGA	Infra-red gas analyser
MOST	Monin-Obukov similarity theory
PF	Planar fit
PKT	Correction method named after Peter K. Taylor
RMS	Root mean square
rPF	Radial planar fit

List of Figures

2.1	Empirical curves for power- and co-spectra densities for neutral conditions ($z/L = 0$). Reproduced from <i>Kaimal et al.</i> (1972)	14
2.2	Physical processes controlling the air-sea gas exchange. Reproduced from <i>Bock et al.</i> (1999)	15
2.3	Two-layer model of gas-liquid interface. Following (<i>Liss and Slater</i> , 1974)	17
2.4	Schematic of the transport of a quantity c by turbulent motion. Adapted from (<i>Burba and Anderson</i> , 2010).	30
2.5	On the left photo of a Licor 7500 open-path gas analyser side by side with a 3RA (Gill) sonic anemometer. On the right a drawing of a Licor 7200 closed-path gas analyser (from the Licor 7200 manual). The 7500 and the 7200 model have the same optical setup.	36
3.1	Map showing the cruise track of the Knorr11 experiment, starting from the Woods Hole Oceanographic Institute on June 24 th and returning there in July 18 th . Start and end of the cruise and selected dates under-way are marked in black as day of the year (doy) 2011.	42

3.2	Air-sea flux setup as deployed during the knorr11 experiment. Wind speed and ship motion were measured at the bow mast. CO ₂ and H ₂ O concentrations, pressure and temperature were measured using closed-path gas analysers situated in a laboratory van on the foredeck. The sample air was collected via a 35 m long inlet tubing.	43
3.3	Map showing the cruise track of the SOAP experiment (February/March 2012) west of New Zealand. The cruise started and ended in Wellington, with a short stop in Lyttleton harbour near Christ Church. Dates of certain ship positions are indicated as days of the year 2012 and can be used for comparison with the time series in Figs. 5.2-5.4.	45
3.4	Map showing the cruise track of the SPURS-MIDAS experiment in spring 2013. The position of the permanent mooring is indicated as a red dot. The part of the track where the flux system was up and running is marked in dark green. The ship left port in Las Palmas on March 16 th and arrived the Azores on April 17 th . These dates and the period during which the ship was close to the mooring are indicated as days of the year 2013. Compare also the time series in Fig. 4.2.	46
3.5	Averages of five consecutive 12 min momentum co-spectra from 7.4.2013 3am-4am. Shown are spectra computed from (i) \mathbf{u}_{me} corrected for mean ship velocity and wind vector tilt (blue) and (ii) fully motion and tilt corrected (red). The sign of C_{wv} was inverted in order to save white ink. The expected shape of C_{wu} as per (<i>Kaimal et al.</i> , 1972) is shown for comparison.	51

3.6	Averages of five consecutive 12 min momentum co-spectra and wind vector power-spectra from 7.4.2013 3am-4am for motion corrections performed with a delayed motion signal. Shown are delays of -1 sec, 0 and +1 sec. The expected (<i>Kaimal et al.</i> , 1972) shapes are shown as black lines.	52
3.7	Normalised co-spectra of the sonic temperature (red), water vapour (blue), and CO ₂ (green). The water vapour spectrum from a dried and un-dried CP IRGA are show. The dry spectrum was normalised against the flux measured by the un-dried IRGA. The spectra are averages of 10 consecutive 25 min flux measurements recorded during the SOAP experiment.	58
3.8	Normalized ogive of the sonic temperature (red), water vapour (blue), and CO ₂ (green) co-spectra, which are shown in Fig. 3.7. The frequency $n_{50\%}$, where the normalised ogive of the temperature flux reaches 50% and the observed flux fractions of CO ₂ and H ₂ O at this frequency are indicated with dashed lines.	60
3.9	Same as in Fig. 3.7, but with gains applied to the normalisation of the CO ₂ and water vapour co-spectra.	61

-
- 4.1 Photograph of the bow of the R/V *Saramiento de Gamboa* with indications of the positions of the 3D sonic and the 2D vane anemometers. Also shown is an illustration of the over-estimation of the pitch of the relative wind vector by the classic motion-tilt correction (4.4). The relative wind vector $\mathbf{u} - \mathbf{v}_{\text{ship}}$ is tilted by the angle θ due to the presence of the ship and measured as \mathbf{u}_{me} with vertical component w . Applying the double rotation after the correction for \mathbf{v}_{ship} gives θ_{DR} which overestimates the tilt. 78
- 4.2 Time series of (a) normalized wind speed and significant wave height; (b) friction velocity; (c) measured relative wind direction and ship speed; (d) true wind direction and distance between ship and buoy position. The buoy values are COARE 3.0 bulk flux results calculated from 1 minute measurements on the mooring, which were averaged to 12 minutes and interpolated on the bow mast time series using the GPS time stamps. Bow mast u_{10N} , true wind direction and u_* are calculated using (4.14) and (4.15), respectively. The shaded areas mark periods that were selected for the estimation of the yaw and acceleration bias in the measured relative wind direction and speed on the bow mast. These periods are also used for the comparison of the direct measurements of u_* on the bow mast with the COARE 3.0 estimates from the buoy. 79

4.3	Pitch and roll angles (θ and ϕ respectively) and the vertical wind speed residual c_3 , determined by the linear regression (4.20) over 15° wind direction bins, are plotted as functions of the measured relative wind direction. The shading shows the 95% confidence intervals of the regression.	84
4.4	Wind vector pitch at the 3D sonic calculated using the classic DR (\circ) and using the alternative method DRx (\diamond) as function of the measured relative wind direction and the ratio of ship velocity and measured wind speed. The results for pitch and roll from the rPF method (see Fig. 4.3) are shown for comparison (black and blue lines).	85
4.5	Ratio of the measured relative wind speed and the expected relative wind speed, calculated from the buoy wind speed and the ship velocity using (4.23) as function of the measured relative wind direction. The uplift was assumed to be zero ($\Delta z = 0$). Individual measurements and averages that were taken over 15° relative wind direction bins are shown as black dots and red line, respectively. The blue dashed line shows the bin average values for an assumed uplift $\Delta z = 4$ m. The error bars show the standard deviation of the mean.	87
4.6	Expected relative wind direction calculated from the buoy wind speed and the ship velocity using (4.23) as function of the measured relative wind direction. Individual measurements and averages that were taken over 15° relative wind direction bins are shown as black dots and red line, respectively. The error bars show the standard deviation of the mean.	88

- 4.7 Observed ratio (r) of the wind speed measured by the 3D sonic (10 masl) and the 2D vane anemometer (16 masl), as function of the measured relative wind direction. Also shown are the bin averages of r and the ratio of the accelerations $r \cdot (1 - x_a) \approx a_1 a_2^{-1}$, calculated with (4.13), for $\Delta z_1 = \Delta z_2 = 0$ and $\Delta z_1 = \Delta z_2 = 4$ m. 90
- 4.8 Ratio of the EC measurements of u_* on-board the R/V *Saramiento de Gamboa* and the COARE 3.0 bulk flux estimates from the mooring as a function of the measured relative wind direction measured on the ship. Individual 12 min measurements are shown as scatter and average values as lines. Results from the rPF method (4.15) are shown as (blue ■ and —) and results using (DR) as (black ◇ and --), and (DRx) as (red ○ and --), respectively. For this comparison, the data were restricted to the selected time periods marked in Fig. 4.2. 92
- 4.9 Direct measurements of u_* as a function of u_{10N} and the measured relative wind direction: panel (a) shows results obtained using the standard motion correction and rotation into the stream (4.4), and panel (b) shows the results using the rPF method (4.15). Individual measurements (12 min) are shown as (○) and bin averages over 30° wind direction and 2 m s^{-1} wind speed bins are shown as thick lines and big ● (error bars show the standard deviation). The COARE3.0 and COARE3.5 bulk flux predictions calculated from u_{10N} are shown as green and black line, respectively. 93

4.10	Same as fig. (4.9) but for the sign-preserving square root of the cross-wind stress component $-\langle vw \rangle \langle vw \rangle^{-0.5}$. Note positive values indicate downward cross-wind momentum flux.	94
4.11	Measured stress angle α_τ (using rPF results) as a function of the measured relative wind direction and u_{10N} . The bin averages (shown as black line) are taken for $u_{10N} \geq 6 \text{ m s}^{-1}$ over 15° wind direction bins. Error bars indicated standard deviation from the mean.	95
4.12	Ratio of the u_* measured with EC and the COARE 3.5 bulk flux prediction using u_{10N} as a function of the relative wind direction and the wind speed. The ratios are presented as bin-averaged values over 15° wind direction and 1 m s^{-1} wind speed bins (minimum 6 measurements per bin). Also shown are 15° wind direction bins for $6 \text{ m s}^{-1} \leq u_{10N} \leq 10 \text{ m s}^{-1}$ (minimum 12 measurements per bin). The errorbars indicate the standard deviation. Panel (a),(b), and (c) show the results using DR, DRx, and rPF respectively.	96
4.13	The bin average ratios from Fig. 4.12 for DR, DRx, and rPF, for the wind speed range $6 \text{ m s}^{-1} \leq u_{10N} \leq 10 \text{ m s}^{-1}$. Also shown are the results for setting the roll angle to zero in the rPF correction method (rPF $\phi=0$). Each bin average is based on a minimum of 12 individual measurements.	97
4.14	Ratios of u_* computed with DR, DRx, and rPF $\phi=0$ and u_* computed with rPF as function of the relative wind direction. The data is presented as bin averages with the standard deviation indicated as shaded area or error bars. Used are the same 15° wind direction bins as in Fig. 4.3.	99

4.15	Same as Fig. 4.14 but for the ratios of the sonic sensible heat flux $\langle wT_{\text{sonic}} \rangle$	100
4.16	Average of 24 12 minute frequency weighted co-spectra from April 7 th , 2013 (02:24 - 07:12), a period of constant wind speed ($u_{10N} = 7.1 \pm 0.4 \text{ m s}^{-1}$) and ship velocity ($v_{\text{ship}} = 5.1 \pm 0.1 \text{ m s}^{-1}$). The relative wind direction was ($\alpha = 25.6 \pm 3^\circ$). Shown are nC_{wu} and nC_{wv} , calculated using (4.15) with flow distortion Euler angles ($\phi = 2^\circ$), ($\theta = 8^\circ$) and ($\psi = -12^\circ$). Co-spectra calculated using (4.4), whit estimated pitch ($\theta_{\text{DR}} = 15^\circ$), are shown in blue. The black line shows the Kaimal spectrum and the grey lines show the expected Kaimal spectra for the tilted (DR) coordinate system estimated using (4.24) and (4.25).	103
4.17	Same as Fig. 4.16 but for the covariance of the vertical wind speed and the speed of sound temperature fluctuations. . . .	104
5.1	Schematic of the Eddy Covariance setup for the SOAP experiment on the R/V <i>Tangoroa</i> . The sample air line is colour-coded in blue and the colour is changed to red downstream of the membrane dryers to indicate that the air is dried at this point.	118

5.2 Overview of conditions encountered during the SOAP experiment. Shaded areas mark low latent heat fluxes ($Q_{\text{lat}} \leq 7 \text{ W m}^{-2}$). The wind speed measurement was taken on the ship's main deck and is corrected for air-flow-distortion (*Popinet et al.*, 2004) and normalised to standard conditions (10 m height and neutral stability). This wind speed was used to calculate the bulk fluxes with the TOGA COARE 3.0 algorithm. All direct EC fluxes are measured at the bow mast using the Csat3 sonic anemometer and the IRGA in the science container on the fore-deck. 121

5.3 Time series of the direct CO₂ fluxes and the flux calculated with the parameterisation of *Sweeney et al.* (2007), plotted on logarithmic scale with sign. Values between $\pm 2 \text{ mol m}^{-2} \text{ yr}^{-1}$ are plotted on linear scale. Shaded areas mark low latent heat fluxes ($Q_{\text{lat}} \leq 7 \text{ W m}^{-2}$). Top: fluxes from *dryA* and *dryB* parallel measurements are linked with vertical lines; middle: fluxes from *wetA* and *wetB*; bottom: fluxes from *wetA* and *wetB* after the PKT correction has been applied to the CO₂ measurements and the results from Eq. (5.11), which are overlaid with the PKT results. 122

5.4	Time series of the bias fluxes in Eq. 5.3, caused by air density fluctuations (<i>Webb et al.</i> , 1980). Top: Bias flux caused by humidity fluctuations F_q upstream of the dryer <i>wet</i> and downstream <i>dry</i> and the CO_2 flux F_c as measured by the IRGA <i>dry</i> (there are only small differences between <i>A</i> and <i>B</i>). Bottom: Bias flux caused by temperature fluctuations F_T as measured by the bow mast sonic and as measured by the CP-IRGAs, and the bias flux caused by pressure fluctuations F_P	123
5.5	Difference between the CO_2 flux calculated from the measured signals x_{cm} from the un-dried gas analysers to the flux from <i>dryB</i> as a function of the EC latent heat flux measurement from the un-dried gas analysers. Different scales are used for the two sub-plots.	125
5.6	Scatter plot of the CO_2 flux measurements (without PKT correction) from <i>wetA</i> , <i>wetB</i> and <i>dryA</i> against those from <i>dryB</i> . For <i>wetA</i> and <i>wetB</i> , only measurements with $Q_{\text{lat}} \leq 7 \text{ W m}^{-2}$ are used. Linear fit coefficients with standard deviation and the R^2 value are shown in the legend.	126

5.7 Scatter plot of the CO₂ flux measurements from *wetA* against those from *dryB* before (left) and after the PKT correction was applied to the *wetA* measurements (right). Bin averages of 15 bins with an equal number of data points are shown as black circles, with error bars indicating the standard deviation from the bin average. A linear regression to the data is shown as a solid black line and the 1 : 1 agreement is indicated with a grey dashed line. Only intervals for which the PKT correction provided a result for both, *wetA* and *wetB*, were used for this plot. 127

5.8 Same as Fig. 5.7, but for *wetB*. 128

5.9 Panel a: Correction factor, $\mu\langle x_v w \rangle$ for $\Gamma = 1$, for IRGA *wetA* plotted as function of the bias estimated by the PKT correction. Both axes are weighted with the cruise average CO₂ flux ($-7.2 \text{ mol m}^{-2}\text{yr}^{-1}$), which was measured by the IRGA *dry*. The correction factor Γ is estimated as linear fit with the y-intercept forced to zero, for latent heat fluxes below, and above 100 W m^{-2} , and for the whole data set Γ_l , Γ_h , and Γ respectively. Panel b: same, but the bias to the CO₂ fluxes measured on dry air is used as x-axis. The latent heat flux measured by the IRGA *wet* is used as color code for both panels. 130

5.10 Same as Fig. 5.9 but for the IRGA *wetB*. 131

-
- 5.11 Normalised transfer velocities calculated using the preliminary flux results from the *wet* and *dry* IRGA (left and bottom right, respectively) and after application of the PKT correction (top right) plotted as functions of the normalised wind speed u_{10N} . Shown are individual 25 min measurements and wind speed-bin averages (mean in red) and (median in grey). The quadratic and cubic parametrisations from *Sweeney et al.* (2007) and *Wanninkhof and McGillis* (1999), respectively are shown as black lines. 132
- 5.12 Scatter plot of the results from Eq. (5.11) against the results of the PKT correction for IRGA *wetB*, individual (blue) and binned (black). 135
- 5.13 Bin-averaged heat fluxes plotted against the standard EC sensible heat flux results (to be compared with Fig. 2 in *Prytherch et al.*, 2010a): “sonic flux” calculated from T_{sonic} (light grey - -); flux after detrending against humidity (black -.); “PKT-corrected” flux (red -.); results of a PKT correction with step width 0.75 and $\beta \approx 4$ (“PKT 4”) (blue -). Error bars show standard deviation from the mean. 1 : 1, 1 : 2 and 2 : 1 agreement are indicated. 136
- 5.14 Ratio of the detrended CO_2 fluxes F_c^0 from *wetA* and *wetB* as used for the PKT correction to the CO_2 flux calculated from *dryB* (purple +, blue +). Two values of the same sample interval are connected with a grey line; the factor $\beta = \left(1 - 0.5 \frac{\langle \text{RH}' w' \rangle}{\langle x_v' w' \rangle} \frac{\partial \langle x_v \rangle}{\partial \langle \text{RH} \rangle}\right)^{-1}$ as in Eq. (5.11), calculated from the latent heat flux and relative humidity, as measured by *wetB*, (grey •). 139

5.15 Wind vector pitch estimated from the double rotation of u_{true} (θ_{DR}) as function of the relative wind direction and of the ratio $v_{\text{ship}}u_{\text{me}}^{-1}$, which is used as colour code. This figure should be compared with Fig. 4.4. 140

5.16 Preliminary gas transfer velocity estimates from the *dry* IRGA as a function of $u_{10\text{N}}$ using the standard DR method. The colour code shows the ratio of ship speed and measured relative wind speed. The measurements are separated into two subsets $v_{\text{ship}}u_{\text{me}}^{-1} \leq 0.1$ (station) and $v_{\text{ship}}u_{\text{me}}^{-1} > 0.1$ (underway) and bin average over 2 m s^{-1} wind speed bins; the error bars represent the standard deviation. 141

5.17 Scatter plot of the CO_2 flux measurements from *dryA* against those from *dryB*. The magnitude of the larger one of the two humidity Webb-correction terms from *dryA* and *dryB* is used as color code with logarithmic scaling. 142

5.18 Average co-spectra of CO_2 (-) and H_2O (- -) from *dryA* as function of the non dimensional frequency. The H_2O co-spectra are weighted with the CO_2 mixing ratio to obtain the magnitude of the Webb-correction. The average co-spectra for the two subsets are shown in different colours: red showing an average from 41 intervals where $F_q \leq 1 \text{ mol m}^{-2} \text{ yr}^{-1}$; blue for 28 intervals with $F_q \geq 1 \text{ mol m}^{-2} \text{ yr}^{-1}$. To avoid flow distortion effects, the ratio $v_{\text{ship}}u^{-1}$ was limited to less than 0.1 and the relative wind direction was limited to $\alpha \leq 30^\circ$. The wind speed range was $7 - 15 \text{ m s}^{-1}$, the average 12 m s^{-1} , and the average relative wind direction $\alpha \leq 15^\circ$ for both subsets. 143

5.19	Scatter plot of the frequency containing 50% of the sonic sensible heat flux ($n_{50\%}$) and u_{10N} . The stability parameter z/L_* serves as colour code. A liner fit to the data fulfilling $z/L_* \leq 0.01$ is shown as black line.	144
5.20	Scatter plot of the gains of H ₂ O (top) CO ₂ (bottom) and u_{10N} . The stability parameter z/L_* serves as colour code. The gains were estimated with $n_{50\%}$ and $n_{20\%}$ for g_{CO_2} and g_{H_2O} , respectively. The average values are shown as black line and stated together with the standard deviation.	145
6.1	Travelling that was involved in this PhD. Flights are marked in red, train rides in green, and cruise tracks in orange, for the MIDAS experiment dashes are used, since I was not on the ship. The numbers indicate routes that I travelled more than twice (return).	168

List of Tables

3.1	Center wavelengths of the optical filter as per LI-840A Manual (ftp://ftp.licor.com/perm/env/LI-840A/Manual/LI-840A_Manual.pdf). These are the same for the LI-7500 and LI-7200 utilized in this thesis (Frank Griessbaum, personal communication).	55
3.2	Probing frequencies and estimated gain factors for the CO ₂ and H ₂ O co-spectra examples (see Fig. 3.8).	62
5.1	Publications addressing the bias in NDIR CO ₂ measurements that is related to relative humidity.	116
5.2	Average CO ₂ fluxes in [mol m ⁻² yr ⁻¹] for the complete experi- ment, and for subsets (Subset 1 [$-7 \text{ W m}^{-2} \leq Q_{\text{lat}} \leq +7 \text{ W m}^{-2}$]; Subset 2 [$-35 \text{ W m}^{-2} \leq Q_{\text{lat}} \leq -7 \text{ W m}^{-2}$]; Subset 3 [$+7 \text{ W m}^{-2} \leq Q_{\text{lat}} \leq 340 \text{ W m}^{-2}$]) based on the EC latent heat flux measured by the un-dried gas analysers. To make the values comparable, only intervals with results from the PKT loop are used for the calculating the mean flux values.	128

1 Introduction and Motivation

The ocean and atmosphere are two fluids in constant interaction, exchanging gases, heat, and momentum. Both the upper ocean with a length scale of 10 m to some 100 m and the lower atmosphere (length scale of several kilometers) are well mixed by turbulent motions which inhibit the establishment of strong gradients (*Liss and Slater, 1974*). Turbulent motions however need space, thus they cannot exist at the very border of the two fluids. The transport of substances through the air-sea interface (submillimetre scale) happens, therefore, only by molecular diffusion, which is a slow process (*Liss and Slater, 1974*). This means that the air-sea interface represents the bottleneck, which ultimately limits the exchange from one fluid to the other. In calm conditions the sub-layers become more developed and air-sea exchange is constrained. Surface turbulence and breaking waves in turn lead to an erosion of the sub-layers and significantly enhance the exchange (*Soloviev and Schlüssel, 1994*). The understanding of the small scale processes in this realm is therefore important for accurate weather and climate predictions (*Brunke et al., 2003*). For example, the strength of hurricanes is controlled by the latent and sensible heat fluxes across the air-sea interface, which supply the rising of convective cells over several kilometres in the atmosphere. In contrast to solid surfaces, the ocean surface friction changes with increasing wind speed due to the development of wind

waves and swell (*Charnock, 1955*). The air-sea exchange rate of trace gases like carbon dioxide is (CO_2) and its dependence on parameters, like the wind speed, is not well constrained, with parameterisation differing by over 100% at high wind speeds (*Ho et al., 2006*)

The key task for the modelling of air-sea interaction is to calculate the air-sea fluxes from the more readily-available meteorological/oceanographic parameters (*Fairall et al., 1996a*). This is achieved by predicting the corresponding exchange rates from relevant bulk parameters e.g. wind speed, sea state, temperature, i.e., the flux of a quantity equals its air-sea gradient times a, potentially variable, exchange coefficient. These parametrisations require input from combined direct flux and air-sea gradient measurements with sufficient temporal and spatial resolutions. The most direct way to measure air-sea fluxes is the eddy covariance (EC) method that allows for short averaging times (10 min – 1 h) and relatively small length scales (1 – 10 km) (*Edson et al., 1998*).

EC requires accurate and fast ($\geq 10 \text{ Hz}$) measurements of the vertical wind speed to resolve all the necessary scales of turbulent motion. Turbulence measurements on board a moving platform (e.g. a ship) require corrections for platform motion (*Edson et al., 1998*) and distortion of the air flow by the platform structure (*Oost et al., 1994*), which can be larger in magnitude than the actual turbulent fluxes. For the measurement of CO_2 fluxes in particular, small fluctuations (in the order of (1 – 10) ppb) need to be resolved against a large background concentration (400 ppm). The available gas analyser technology limits the measurements to areas of relatively large air-sea fluxes (*Rowe et al., 2011*). Additionally, the measurement quality suffers from a weakly-understood cross-sensitivity to the much larger and omnipresent humidity flux. This cross-sensitivity can lead to biases which are an order

of magnitude larger than the CO_2 flux itself (Prytherch *et al.*, 2010a). It is therefore not surprising that results from direct CO_2 flux measurements exhibit large scatter and sometimes lead to gas-transfer velocities that must be considered unrealistic (Broecker *et al.*, 1986). However in the medium to long term, this method will likely become the state-of-the-art for air-sea flux measurements, in a similar fashion to atmosphere-land fluxes.

The aim of the work presented in this thesis was to improve the EC measurement technique for the air-sea exchange of CO_2 , focussing on the following aspects:

- The treatment of air-flow distortion, which is a key problem for wind speed and direct flux measurement from large structures, such as ships or platforms.
- The treatment of the cross-talk between CO_2 and H_2O signals from the current commercially-available gas analysers.

The outline of this thesis is as follows: the scientific background and the current state of the field are outlined in Chapter 2. Chapter 3 then gives an overview of the conducted field experiments, and a description of the eddy covariance instrumentation and data analysis. Chapters 4 and 5 present two articles that were written within the framework of this PhD. The first article, presented in Chapter 4, introduces an improved treatment of air-flow distortion for direct flux measurements on moving platforms and was submitted to the *Journal of Atmospheric and Oceanic Technology*. This method removes an error from the direct EC fluxes that is in the order of 10%. The second article, presented in Chapter 5, is published in *Atmospheric Chemistry and Physics* (Landwehr *et al.*, 2014). It discusses the water vapour cross-sensitivity of the infra red gas analyser, which are commonly used to

measure CO₂ fluxes. This cross-sensitivity is currently the largest error source for direct CO₂ flux measurements and can even change the sign of the measured CO₂ fluxes. In Chapter 6 the work is summarised and conclusions as well as suggestions for further work are provided.

2 Theory and Literature Review

2.1 Introduction

This chapter summarises the theoretical and experimental background, which is relevant to this thesis. In Section 2.2 the basic ideas of boundary-layer theory are introduced. These concepts link the surface fluxes of momentum, heat, humidity, and trace gases with their height profiles and thus allow for ‘bulk parameterisations’, i.e., linking the surface flux with the air-sea gradient via a transfer coefficient. The definition of the relevant parameters to predict these transfer coefficients is the key to accurate modelling of local and global transport processes across the air-sea interface. The nature of the turbulent transport in the atmosphere and the empirical laws for the spectral distribution of turbulent motions are presented in Section 2.3. This is followed by an overview about different models describing air-sea gas exchange in Section 2.4. In Section 2.5 the TOGA COARE model is taken as an example for a bulk flux formulation of air-sea fluxes with more easily performed bulk concentration measurements. The eddy covariance method, which was used for the flux measurements presented in this thesis, is described in Section 2.6.

2.2 Flux-Profile Relationship

Monin and Obukhov (1954) proposed non-dimensional relationships between the turbulent surface fluxes and the vertical profiles of the meteorological quantities: vector averaged wind speed ($U = \sqrt{\langle u \rangle^2 + \langle v \rangle^2 + \langle w \rangle^2}$), temperature (T) and humidity (q). This is known as Monin-Obukhov Similarity Theory (MOST), described with the following equations:

$$\frac{z}{u_*} \frac{\partial U}{\partial z} \kappa = \Phi_m\left(\frac{z}{L_*}\right) \quad (2.1)$$

$$\frac{z}{t_*} \frac{\partial t}{\partial z} \kappa = \Phi_t\left(\frac{z}{L_*}\right) \quad (2.2)$$

$$\frac{z}{q_*} \frac{\partial q}{\partial z} \kappa = \Phi_q\left(\frac{z}{L_*}\right) \quad (2.3)$$

where z is the measurement height, $u_* = (\langle w'u' \rangle^2 + \langle w'v' \rangle^2)^{1/4}$ is the friction velocity, and $t_* = -\langle w'T' \rangle / u_*$ and $q_* = -\langle w'q' \rangle / u_*$ are the MOST scaling parameters for velocity, temperature and humidity, respectively. The angular brackets $\langle \cdot \rangle$ denote a time average and the prime indicates the deviation from the mean of a quantity ($\chi' = \chi - \langle \chi \rangle$). The van Kármán constant (κ) is determined empirically to be about 0.4 and appears to be the same for all three scalars (*Högström*, 1996). The empirical stability functions Φ_m , Φ_t , and Φ_q account for the effect of the surface buoyancy flux:

$$\langle w'b' \rangle = \frac{g}{T} \langle w'T' \rangle + 0.61g \langle w'q' \rangle \quad (2.4)$$

where $g \approx 9.81 \text{ m s}^{-2}$ is the gravitational acceleration. The stability functions, (2.1), (2.2), and (2.3), depend only on the height above the surface

and the stability length scale, which is defined as

$$L_* = -\frac{u_*^3}{\kappa \langle w'b' \rangle}. \quad (2.5)$$

Positive buoyancy flux ($1/L_* < 0$, *unstable* conditions) implies convective turbulence that reduces the steepness of the scalar profiles. If the buoyancy flux is negative ($1/L_* > 0$, *stable* conditions), the turbulent motion have to work against the stratification of the atmosphere and are suppressed. This leads to steeper mean velocity gradients. If the buoyancy flux is small compared to the turbulent transport, the stability functions approach unity. This is called *neutral* condition.

Over land, the stability functions have been determined empirically, and a large variety can be found in the literature. The most widely used forms are those following *Dyer and Hicks* (1970); *Dyer* (1974), which were developed semi-empirically based on data from the Kansas experiment. For the unstable case $L_* < 0$ the stability functions take the form:

$$\Phi_\chi = \gamma_\chi \left(1 - \alpha_\chi \frac{z}{L_*}\right)^{N_\chi} \quad (2.6)$$

and for the stable case $L_* > 0$:

$$\Phi_\chi = \gamma_\chi + \beta_\chi \frac{z}{L_*} \quad (2.7)$$

were χ substitutes any of the scalars u , q , T . Due to the large difficulties related with making direct flux measurements, published values for coefficients cover a relatively wide range. Here $\gamma_u = 1$, $\gamma_T = 0.95$, $\alpha_u = 19$, $\alpha_q = \alpha_T = 11.6$, $\beta_u = 5.3$, $\beta_T = 8$, $N_u = 1/4$, and $N_q = N_T = 1/2$ are used as proposed by (*Högström*, 1996) for $\kappa = 0.4$. The dimensionless profiles

of all variables are found to become proportional to $(-z/L_*)^{1/3}$, for the limit of free convection ($L_* \rightarrow -\infty$). This is achieved by blending the *Dyer and Hicks* (1970) form with another empirical functionality that fulfils this condition (e.g *Fairall et al.*, 1996a). Over the ocean, the data base of flux profile measurements and suggestions for the stability function are much more limited. *Edson et al.* (2004) reported coefficients for the open ocean humidity profile that are in general agreement with the values observed over land ($\alpha_q = 13.4 \pm 1.7$).

Integration of the velocity profile leads to the form:

$$\frac{u(z)}{u_*} + \kappa^{-1}\Psi_m\left(\frac{z}{L_*}\right) = \kappa^{-1}\ln\left(\frac{z}{r}\right) + C = \kappa^{-1}\ln\left(\frac{z}{\alpha \cdot r}\right) \quad (2.8)$$

where the length scale r and the constant $C = \ln(\alpha^{-1})\kappa^{-1}$ need to be determined empirically. The left hand side in (2.8) is the sum of the ratio of the wind speed profile to the friction velocity and the stability correction Ψ_m , which is the integrated form of Φ_m :

$$\Psi_m\left(\frac{z}{L_*}\right) = \int_{z_0}^z \left[1 - \Phi_m\left(\frac{z}{L_*}\right)\right] \frac{d(z/L_*)}{z/L_*} \quad (2.9)$$

It is general practice report wind speed measurements normalize to a standard height of $z = 10$ m and neutral stability (u_{10N}).

The value of $z_0 = \alpha \cdot r$ can be interpreted as the roughness length of the sea surface. A higher value of z_0 means increased drag and consequently, a steeper wind speed profile. *Charnock* (1955) suggested the length scale $r = u_*^2 g^{-1}$ and determined $C \approx 12.5$ or $\alpha \approx 0.007$. For low wind speeds the air-sea interface is better described as a smooth surface, with the ratio of the viscosity of air (ν_a) and u_* as appropriate length scale. *Smith* (1988)

combined rough and smooth length scales

$$z_0 = \frac{\alpha u_*^2}{g} + \frac{\gamma \nu_a}{u_*} \quad (2.10)$$

and suggested $\alpha = 0.011$. The roughness Reynolds number for smooth flow, γ , is widely accepted to be 0.11 (e.g. *Smith, 1988; Fairall et al., 1996a*). However, *Andreas and Treviño (2000)* suggested $\gamma = 0.135$. *Yelland (1996)* determined u_* with the inertial dissipation method (IDM), and found α to increase with wind speed. They revised their results using corrections for air-flow distortion and height displacement (*Yelland et al., 1998*), and improvements in the IDM (*Taylor, 2000*), to find $\alpha = 0.011$ independent of the wind speed. *Fairall et al. (2003)* and *Edson et al. (2013)*, on the other hand, used a wind speed-dependent Charnock parameter for the COARE bulk flux algorithm (see Sec. 2.5). In the latest version (COARE 3.5) $\alpha = 0.017u_{10N}[\text{m s}^{-1}] - 0.005$ is used for wind speeds below 18 m s^{-1} , and a constant $\alpha = 0.028$ for higher wind speeds.

Equation (2.8) is classically used in the form of the neutral drag coefficient $C_{D10N} = u_*^2 u_{10N}^{-2}$. This leads to the relation:

$$C_{D10N} = \kappa^2 \ln \left(\frac{10}{z_0} \right)^{-2} \quad (2.11)$$

From (2.10) it is apparent that the drag coefficient varies with the friction velocity. But it is more common to report the drag coefficient as a function of the wind speed, as u_{10N} and u_* are ultimately linked.

2.3 Turbulence Spectra

The turbulent motion and transport in the atmosphere span a wide range of length and time scales. The turbulent energy of a scalar quantity like u is given by the integral of the power-spectrum (F_u) over all wave numbers in direction of the mean flow (κ_u), or over all frequencies ($n = \kappa_u U (2\pi)^{-1}$):

$$\langle u'u' \rangle = \int_0^\infty F_u(\kappa_u) d\kappa_u = \int_0^\infty S_u(n) dn. \quad (2.12)$$

Here, the second equal sign is based on Taylor's hypothesis and S_u denotes the power-spectrum in the frequency domain.

For two quantities (e.g. w and u) the cross-covariance can be defined

$$R_{wu}(\delta x) = \langle w'(x)u'(x + \delta x) \rangle \quad (2.13)$$

where δx denotes a separation in space (equivalent to a separation in time for co-located time series measurements). The cross-spectrum can be defined as the Fourier-transformation into wave number space that can be separated into a real- and imaginary parts (the variances of u and w that are out of phase):

$$\int_{-\infty}^{\infty} R_{wu}(\delta x) \exp(-i\kappa_u \delta x) d(\delta x) = C_{wu}(\kappa_u) - iQ_{wu}(\kappa_u). \quad (2.14)$$

The real and imaginary part are called co-spectrum and quadrature-spectrum, respectively. The integral of $Q_{wu}(\kappa_u)$ is identical to zero and the integral over $C_{wu}(\kappa_u)$ returns the covariance of u and w , i.e., the vertical momentum

flux:

$$\int_{-\infty}^{\infty} C_{wu}(\kappa_u) d\kappa_u = 2 \int_0^{\infty} C_{wu}(\kappa_u) d\kappa_u = \langle w'u' \rangle \quad (2.15)$$

The co-spectrum therefore provides information about the contribution of different size eddies to the total flux. If $nC_{wu}(n)$ is plotted over $\log(n)$, the contribution of a range of frequencies to the momentum flux can be calculated from the area under the curve.

It is common practice to plot co- and power-spectra as functions of the dimensionless frequency

$$f = \frac{nz}{U}. \quad (2.16)$$

This makes spectra measured at different heights or wind speeds comparable.

In the frequency domain, atmospheric motions can be divided into synoptic scales (hours to month) and microscales (minutes to fractions of seconds). The two domains are separated by the mesoscale gap i.e. an observed minimum of turbulence activity at the time scale of about 1 hour. The turbulent fluxes, which are studied in this thesis reside in the microscale domain below 1 hour. Motions beyond this time scale are treated as 'mean flow'.

Within the microscale domain is the energy-containing or production range for $f \leq 0.01$. Here the turbulent motions are fed by the mean flow (the large scale motions from the synoptic scale). The range ($0.01 \leq f \leq 5$) is called the inertial subrange. Here the flow is isotropic (no mean flow direction can be defined), no turbulence is produced, and the large eddies are broken down into ever smaller eddies by viscous forces. However, the kinetic energy is conserved. Beyond $f \geq 5$ is the viscous subrange, where

the eddies dissipate into thermal energy due to the viscous forces. When the boundary layer can be described with by law-of-the-wall theory (assuming a constant stress layer), the dissipation rate of turbulent kinetic energy at a height z is given by:

$$\epsilon(z) = \frac{u_*^3}{\kappa z}. \quad (2.17)$$

According to Kolmogorov's law the one-dimensional spectrum of u , in the inertial subrange, is given by:

$$F_u(\kappa_u) = a_u \epsilon^{2/3} \kappa_u^{-5/3}. \quad (2.18)$$

Here $a_u \approx 0.52$ is the Kolmogorov constant, according to a review of field experiments by *Högström* (1996).

Assuming that an inertial subrange also exists for temperature, *Corrsin* (1951) gives a similar equation for the temperature spectra F_T :

$$F_T(\kappa_u) = a_T \epsilon^{-1/3} N_T \kappa_u^{-5/3}. \quad (2.19)$$

Here N_T is the dissipation rate of the temperature variance [$\text{K}^2 \text{s}^{-1}$] and a_T is the Kolmogorov constant for temperature ($a_T \approx 0.8$ according to *Högström* (1996)). Spectra of other scalars like q or CO_2 are found to obey the same functionality, with their respective dissipation rates N_q and N_c and equal Kolmogorov constants $a_q = a_c = a_T = 0.8$ (*Hill*, 1989).

Kaimal et al. (1972) show that the power spectra can be normalized using the dimensionless frequency and the dimensionless dissipation rates $\Phi_\epsilon = \kappa z \epsilon u_*^{-3}$, $\Phi_{N_\chi} = \kappa z N_\chi u_*^{-1} \chi_*^{-2}$ (with $\chi = q$ or T or c), that are all

functions of z/L :

$$\frac{nS_u(n)}{u_*^2 \Phi_\epsilon^{2/3}} = \frac{a_u}{(2\pi\kappa)^{2/3}} f^{-2/3} \quad (2.20)$$

$$\frac{nS_\chi(n)}{\chi_*^2 \Phi_\epsilon^{-1/3} \Phi_{N_\chi}} = \frac{a_\chi}{(2\pi\kappa)^{2/3}} f^{-2/3} \quad (2.21)$$

Thus, when normalized accordingly and plotted in log-log representation, all spectra should coincide in a $-2/3$ slope.

Similarly, the normalised co-spectra follow a $-4/3$ slope in the inertial subrange,

$$\frac{nC_{uw}(n)}{u_*^2 G(z/L)} \propto f^{-4/3} \quad (2.22)$$

where $G(z/L)$ is another empirical function (*Kaimal et al.*, 1972). Based on data from the Kansas experiments, *Kaimal et al.* (1972) provide empirical functions for Φ_ϵ , and Φ_{N_χ} and for the full shapes of the co- and power spectra of u, v, w and T in neutral conditions over the frequency range $0.01 \leq f \leq 4$. The empirical Kaimal spectra for neutral conditions are plotted in Fig. 2.1 in log-log representation. For unstable conditions, the peaks of the spectra are higher and shifted to higher frequencies and for stable conditions, large eddies are suppressed and the spectral peaks are lower and shifted to lower frequencies (*Kaimal et al.*, 1972).

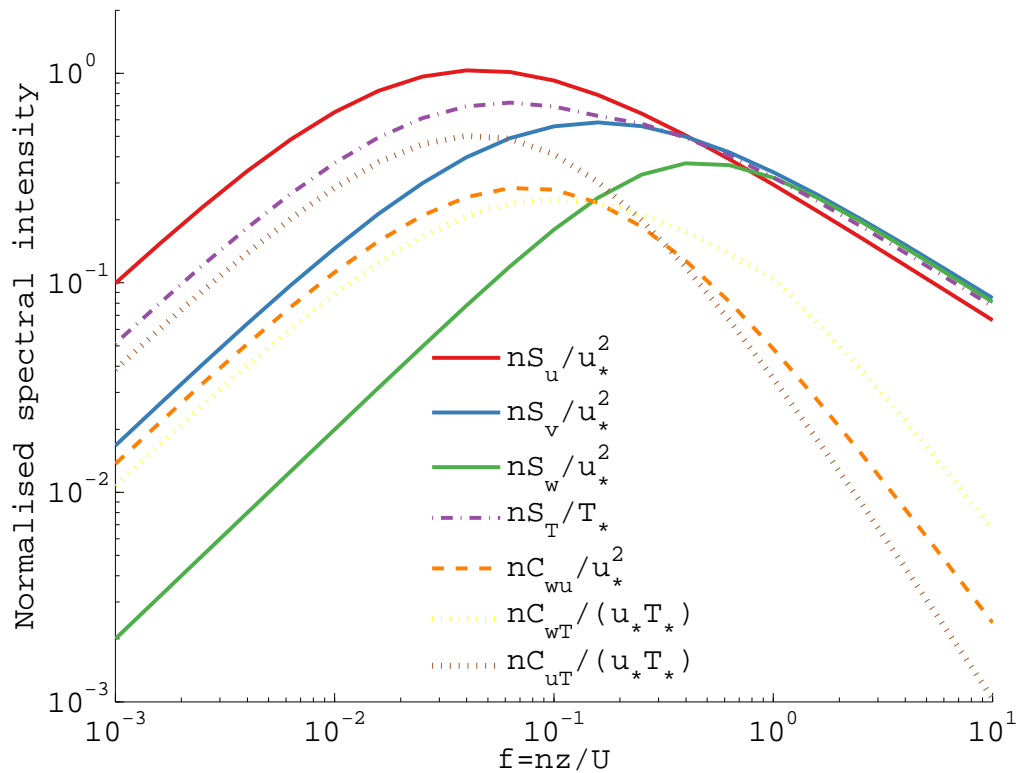


Figure 2.1: Empirical curves for power- and co-spectra densities for neutral conditions ($z/L = 0$). Reproduced from *Kaimal et al.* (1972)

2.4 Model Description of Gas Exchange at the Air-Sea Interface

The gas transfer velocity at the air-sea interface is influenced by many processes like turbulent mixing at the surface, wave breaking, bubble creation, the presence of surfactant films, and possible chemical reactions of the gas with the fluid. It also depends on gas-specific properties like the diffusivity in air and seawater. Figure 2.2 summarises the relevant physical processes and their interaction.

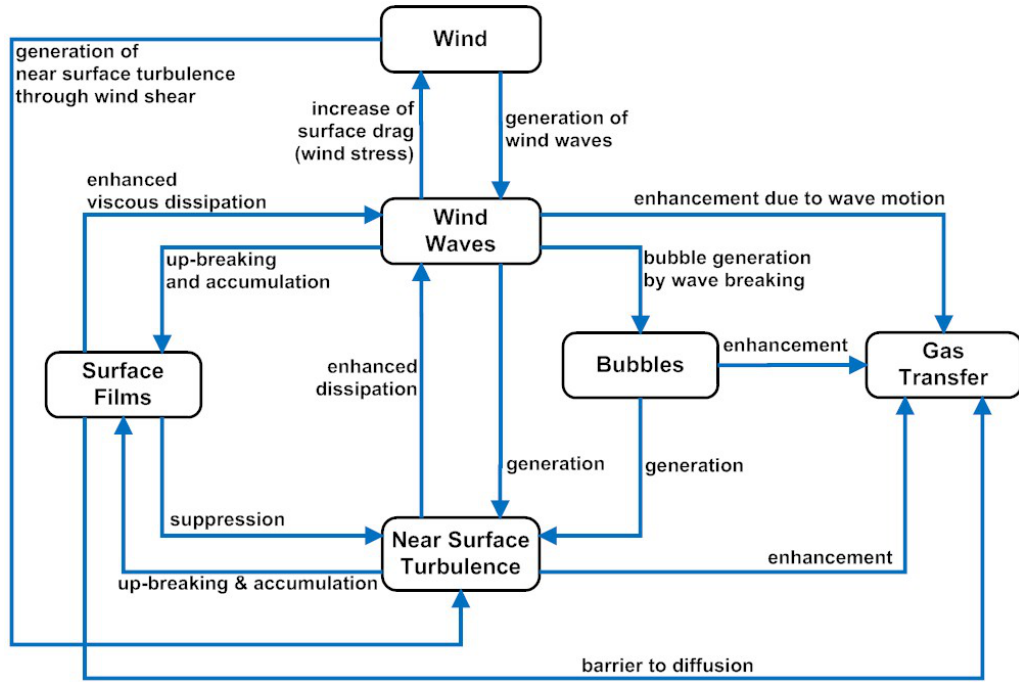


Figure 2.2: Physical processes controlling the air-sea gas exchange. Reproduced from *Bock et al. (1999)*

2.4.1 Two-Film Model

A simple model for gas transfer across the air-water interface was developed by *Liss and Slater (1974)*, see Fig. 2.3 for illustration. The main bodies on the air and water side are assumed to be well-mixed, leading to uniform concentrations in each phase. Concentration gradients only occur in the thin films at the boundary layer. Here the transport is given by molecular diffusion and will be proportional to the concentration gradient:

$$F = k_w(C_{wi} - C_w) = k_a(C_a - C_{ai}) \quad (2.23)$$

The transfer velocities k_a and k_w are proportional to the diffusivity of the gas in air (D_a) and water (D_w), and inversely proportional to the thickness of the diffusive layers at the air side (δ_D^a), and at the water side (δ_D^w).

The parameters C_a and C_w are the bulk air and seawater concentrations respectively, while C_{wi} and C_{ai} are the concentrations directly at the air-sea interface, which are linked by Henry's Law coefficient (H):

$$C_{ai} = H \cdot C_{wi} \quad (2.24)$$

H varies with temperature and salinity. Using (2.24) in (2.23) leads to:

$$F = K_w(C_a/H - C_w) = K_a(C_a - HC_w) \quad (2.25)$$

where $1/K_w = 1/k_w + 1/(k_a H)$ and $1/K_a = H/k_w + 1/k_a$. The flux is given by the bulk concentration gradient (after correction for solubility by using Henry's Law) and the overall transfer velocity (K) that is given as the inverse sum of the air and water side transfer velocities. For poorly soluble gases like O_2 , CO_2 , CH_4 , and SF_6 the waterside diffusion is much smaller than on the air side and K_w can be approximated with k_w .

For the smooth surface (solid boundary layer - this also applies to a calm sea) the thickness of the viscous sub-layer (δ_ν) is given by the ratio of the kinematic viscosity of the medium (ν) and the friction velocity:

$$\delta_\nu^w = 11 \frac{\nu_w}{u_{*w}} \quad (2.26)$$

where $u_{*w} = u_* (\rho_a \rho_w^{-1})$ is the water side friction velocity and the constant is taken from *Chriss and Caldwell* (1984).

The diffusive sub-layer is proportional to thickness of the viscous sub-layer and also depends on the Schmidt number,

$$Sc = \nu_w / D_w. \quad (2.27)$$

The dependency is generally assumed to take the form:

$$\delta_D^w \propto \delta_\nu^w Sc^{-n}. \quad (2.28)$$

The thin-film model predicts $n = 1$ and thus:

$$k_w \propto u_* Sc^{-1} \quad (2.29)$$

The conditions assumed by the thin-film model are however rarely met over the open ocean, since buoyancy or wind-induced turbulence leads to an erosion of the diffusive sub-layer. The Schmidt number coefficients found in wind tunnel studies vary between $2/3$ and $1/2$ (*Jähne et al.*, 1987).

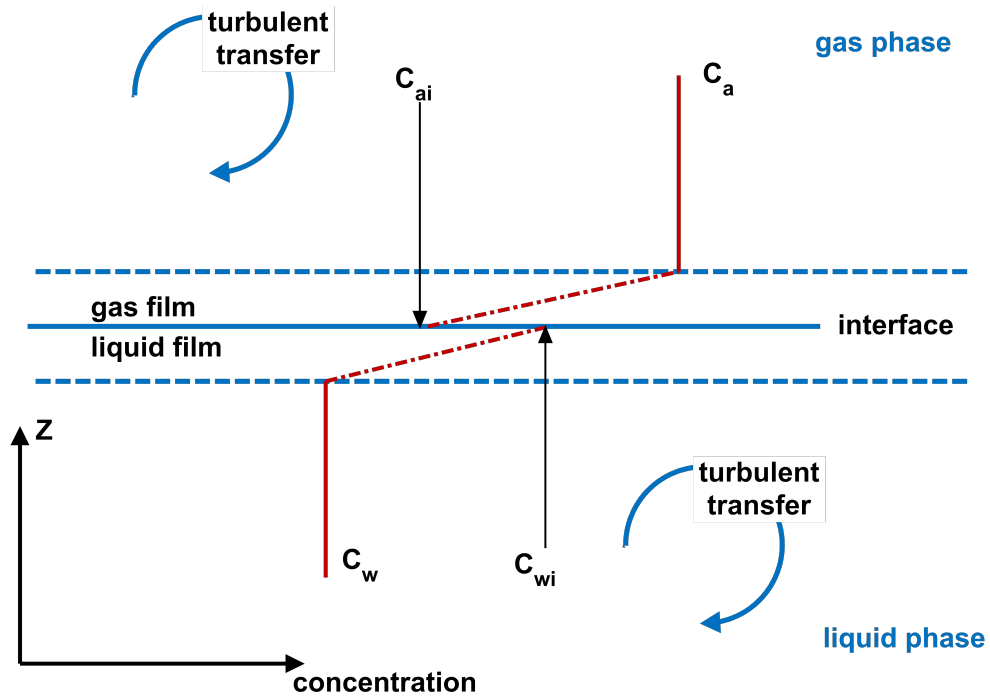


Figure 2.3: Two-layer model of gas-liquid interface. Following (*Liss and Slater*, 1974)

2.4.2 Surface Renewal Model

A more realistic representation of air-sea gas transfer is given by the surface renewal model (e.g. *Higby, 1935; Danckwerts, 1951; Soloviev and Schlüssel, 1994; Soloviev, 2007*). The model assumes that a diffusion- and a thermal sub-layer (cool skin) form within the viscous sub-layer at the ocean-atmosphere interface. Parcels of fluid at the interface are intermittently replaced with parcels from the bulk fluid by bursting motions. From the high water side resistance for the gas flux, *Soloviev and Schlüssel (1994)* concluded that for the time between two bursts, the concentration difference across the diffusive sub-layer can be assumed constant and equal to the bulk concentration difference. They also assume that the net surface heat flux Q_{net} , defined as:

$$Q_{\text{net}} = Q_{\text{lat}} + Q_{\text{sen}} + (R_{l\uparrow} - R_{l\downarrow}) \quad (2.30)$$

can be assumed constant during this time. This follows from the fact that Q_{net} is largely controlled by latent heat flux (Q_{lat}) and the net long wave radiation ($R_{l\uparrow} - R_{l\downarrow}$). Therefore Q_{net} does not depend on the (local) temperature gradient across the cool skin ($\Delta T(t)$), which controls the sensible heat flux (Q_{sen}). The parameters $\Delta T(t)$ and $F(t)$ of the fluid parcel consequently decay in time until a new burst occurs. The average temperature gradient and the reciprocal of the average interfacial gas transfer velocity $k_i = \langle F(t) \rangle \Delta C^{-1}$ are therefore both proportional to square root of the mean time between the bursts (t_{burst}):

$$k_i \propto t_{\text{burst}}^{-1/2} S C^{-1/2} \quad (2.31)$$

$$\Delta T \propto t_{\text{burst}}^{1/2} Q_{\text{net}} \quad (2.32)$$

Soloviev and Schlüssel (1994) describe three regimes:

$$t_{\text{burst}} \propto \left(\frac{\nu_w}{B_w}\right)^{1/2} \quad \text{for } u_{10N} \approx 0 - 5 \text{ m s}^{-1} \quad (2.33)$$

$$t_{\text{burst}} \propto \frac{\nu_w}{u_*^2} \quad \text{for } u_{10N} \approx 5 - 10 \text{ m s}^{-1} \quad (2.34)$$

$$t_{\text{burst}} \propto \frac{u_*}{g} \quad \text{for } u_{10N} \geq 10 \text{ m s}^{-1}. \quad (2.35)$$

In the first, low wind speed regime (2.33), convection, driven by the water side buoyancy flux (B_w), governs the renewal of the surface layer. The water side buoyancy flux is defined according to *Jeffery et al.* (2007):

$$B_w = \frac{g\alpha_T Q_{\text{net}}}{c_{pw}\rho_w} + \frac{g\alpha_S Q_{\text{lat}}}{L_{ev}\rho_w}. \quad (2.36)$$

Here α_T and α_S denote the thermal and haline expansion coefficient of sea-water, ρ_w is the sea-water density, and L_{ev} is the latent heat of vaporization. In moderate wind speed conditions (2.34), the surface renewal is caused by viscous surface-stress variations associated with rollers on breaking wavelets (*Csanady*, 1990), and gas transfer becomes proportional to u_* . At high wind speeds (2.35), shadowing effects and long surface wave breaking suppress the short wavelets and therefore reduces the interfacial gas transfer velocity (*Soloviev and Schlüssel*, 1994).

The onset of wave breaking does however open a new pathway of gas exchange due to the formation of sea spray and the injection of air-bubbles (*Wanninkhof et al.*, 1995; *Woolf*, 1997) (See also Sec. 2.4.3). For less soluble gases like CO_2 , this new pathway can more than offset the roll-off that is predicted by (2.35). The surface renewal model is supported by observations of convergence and divergence in the interfacial layer (e.g. *Jähne et al.*, 1987), as well as by the results of *Yang et al.* (2011) and *Bell et al.* (2013), who

observed a sea state dependent suppression of the exchange of Dimethyl Sulfide (DMS) at high wind speeds. DMS is more soluble than CO_2 and therefore less sensitive to bubble enhancement.

2.4.3 Bubble-Mediated Gas Transfer

Studies at sea (*McGillis et al.*, 2001a), in wind tunnels (*Broecker and Siemens*, 1984), and in a surf pool (*Wanninkhof et al.*, 1995), have shown large increase in gas fluxes at high wind speeds (above 10 m s^{-1}) due to breaking waves, whitecap production, and the injection of bubbles into the sea surface that present an additional pathway for the flux. The flux can be described as the sum of (i) the flux through the unbroken surface with the transfer velocity k_i and (ii) the bubble-mediated flux through the area fraction covered by whitecaps (WCF) with the bubble-mediated transfer velocity k_b :

$$k_w = k_i \cdot (1 - WCF) + k_b \cdot WCF \quad (2.37)$$

Monahan and Spillane (1984) found that the white-cap fraction WCF scales roughly with $(u_{10N})^3$; parameterisations obtained by later studies however vary over an order of magnitude (see *Anguelova and Webster*, 2006). This might be partly due to the evolution of measurement techniques: while (*Monahan and Spillane*, 1984) manually weighed the fraction of photographs that was covered by whitecaps, the WCF can nowadays be determined using automated image processing (*Callaghan and White*, 2009) or remote sensing (*Anguelova and Webster*, 2006). It is also important to distinguish between active breaking waves (stage A) and mature white caps (stage B), since gas exchange is enhanced mostly by the active breaking waves (*Scanlon and*

Ward, 2013). The lifetime of mature whitecaps and thus the ratio of stage A to stage B varies with salinity, temperature, and the presence of surfactants (Callaghan *et al.*, 2012; Scanlon and Ward, 2013).

Gases with very low solubility in sea-water such as CO₂ are expected to experience a greater enhancement than gases with higher solubility like DMS (Keeling, 1993). This is reflected in the different wind speed dependencies of DMS and CO₂ for wind speeds above 6 m s⁻¹ (Blomquist *et al.*, 2006). Miller *et al.* (2009), who obtained transfer velocities from parallel direct air-sea flux measurements of CO₂ and DMS, found no significant enhancement of $k(\text{CO}_2)$ over $k(\text{DMS})$ for wind speeds below 10 m s⁻¹. Contemporaneous measurements of the gas transfer rate of CO₂ and DMS promise to provide a better understanding of the influence of bubble mediated transport on air-sea gas exchange at higher wind speeds.

2.4.4 Wind speed parameterisation

Over the open ocean, surface turbulence and thus the erosion of the diffusive sub-layer is mostly driven by the surface wind speed. This led to the most common approach, which is to parameterise transfer velocities as function of u_{10N} . The most widely used wind speed parameterisation was derived by (Wanninkhof, 1992) assuming a quadratic wind speed dependence $k \propto u_{10}^2$ and using (2.25) with flux estimates from the ¹⁴C bomb invasion and global wind speed and $\Delta p\text{CO}_2$ estimates. Gas transfer measurement by dual tracer (³He/SF₆) methods over the open ocean find a similar dependency of k_{660} on the wind speed (Nightingale *et al.*, 2000; Ho *et al.*, 2011). Experiments using the direct eddy covariance flux method with CO₂ as tracer often predict a stronger, cubic dependency of k_{660} on wind speed (Wanninkhof and McGillis,

1999; Prytherch *et al.*, 2010b). This observed enhancement of the gas transfer of CO₂ is attributed to bubble mediated gas transfer in the presence of wave breaking (*Wanninkhof and McGillis, 1999*). At high wind speeds ($\geq 15 \text{ m s}^{-1}$), where a significant part of the flux occurs, the predictions for k_{660} from various published parameterisations differ by a factor of two (*Ho et al., 2006*) and leave large uncertainty about the expected magnitude of the air-sea flux. These large discrepancies could be caused by regional differences, surface films, limited fetch, or by measurement errors. At low wind speeds other processes such as convection can enhance the mixing and thus the transfer rate (e.g. *McGillis et al., 2004; Rutgersson and Smedman, 2010*, see also Sec. 2.4.5). Wind speed only parameterisations are attractive due to the simplicity of their application; they neglect, however, the underlying complexity of the processes that govern the air-sea gas exchange. Considering the multiple parameters, which have been found to influence gas transfer, a wind speed only parameterisation appears to be a somewhat oversimplified approach.

2.4.5 Water Side Convection

Surface cooling and evaporation cause water side convection. In a low wind environment this process can control the surface mixing and lead to an increase of the mixed-layer depth. This can significantly enhance the gas transfer (*McGillis et al., 2004*). *Rutgersson and Smedman (2010)* derive an additional term (k_c) that should be added to wind speed only transfer velocities (k_u), in order to account for water side convection:

$$k_{660} = k_u + k_c \tag{2.38}$$

k_c is proposed to be a function of the convective velocity scale W_w which is defined by *Jeffery et al.* (2007) in analogy to the atmospheric mixed layer scaling (2.49) as a product of the mixed layer depth z_{ml} and the water-side buoyancy flux:

$$W_w = (B_w z_{ml})^{1/3}. \quad (2.39)$$

Based on measurements in the Baltic sea over a wind speed range between 2.5 and 6.5 m s⁻¹ *Rutgersson and Smedman* (2010) propose for k_c to take the form:

$$k_c = 3022W_w - k_{c0} \quad (2.40)$$

for $W_w > 0.006$ ms⁻¹ and $k_c = 0$ cm·hr⁻¹ otherwise; here $k_{c0} = 20$ cm·hr⁻¹.

There is a notable difference to *Soloviev* (2007), who scale k_c with $(B_w \nu_w)^{1/4}$. The findings of *Rutgersson and Smedman* (2010) attribute relevance to processes in the mixed layer, while the surface renewal model predicts that the gas exchange rate is solely controlled by processes in the interfacial layer.

2.4.6 Mean square slope

Surface waves have significant impact on air-sea gas exchange. The boundary layer model predicts a Schmidt number dependency of $n = 2/3$ for smooth surfaces (*Deacon*, 1977), while for surfaces ruffled by waves *Csanady* (1990) predicts a $n = 1/2$ dependency. Laboratory measurements by *Jähne et al.* (1987) confirm the transition in the Schmidt number dependency of the gas transfer velocity from $n = 2/3$ to $n = 1/2$.

Waves support the formation of local convergences and divergences that lead to a thinning of the diffusive sub-layer (see *Csanady, 1990*). Further, the wind energy is more efficiently transferred due to the increased roughness length (wind-wave interaction). This increases surface turbulence and, therefore, the gas transfer.

The wave field can be described by the mean square wave slope ($\langle S^2 \rangle$), which was found to explain field measurements of the transfer velocity of heat much better than wind speed alone (*Frew et al., 2004*). *Frew et al. (2004)* reported that $\langle S^2 \rangle$ explains 89 – 95% of the observed variance in k_{heat} measurements in coastal and offshore sites with a wide range of biological activity, while wind speed only accounted for 75 – 77% of the observed variance and tended to over-predict the transfer in the presence of surface films. *Bock et al. (1999)* presented results from laboratory studies which suggest that gas transfer is mainly influenced by short waves (wavelength ≤ 3 cm). *Bock et al. (1999)* also reported a suppression of the gas transfer velocity by surface films of up to 60% in accordance with a suppression of short waves. Information on wave slope can be obtained from satellite-based instruments like altimeters and scatterometers, e.g., QuikSCAT. Recently *Goddijn-Murphy et al. (2012)* published a study about the correlation between satellite based wave height measurements and ship borne measurements of the DMS transfer rate. They found that the correlation of k_{gas} with $\langle S^2 \rangle$ can be improved by excluding wave lengths ≥ 5 cm, confirming that gas transfer is mostly influenced by short wind waves. While satellites appear to be a powerful tool to obtain air-sea interaction measurements with nearly global coverage, it should be kept in mind, that the remote sensing techniques always require validation with ground based measurements.

2.4.7 Turbulent Dissipation Rate and Gas Exchange

The thickness of the diffusive sub-layers and thus the gas transfer velocity can be described in terms of the turbulent dissipation rate at the interface $\epsilon_0 = \epsilon(z = \delta_\nu)$ (e.g. *Lorke and Peeters, 2006*). The dissipation rate within the viscous sub-layer can be regarded as constant (*Lorke and Peeters, 2006*). The eddy cell model of gas transfer at the interface of two fluids, which was presented by *Lamont and Scott (1970)*, results in a scaling relationship of the form

$$k \propto Sc^n (\epsilon_0 \nu)^{1/4}. \quad (2.41)$$

This dependency is assumed to hold in a much wider range of conditions, than the parameterisation of k with u_* (*Lorke and Peeters, 2006*). For example for strong convection or in the presence of wave breaking. In these conditions the relation of ϵ to u_* , given with (2.17), cannot be used to interpolate the surface value ϵ_0 .

Lorke and Peeters (2006) derive (2.41) for interfacial gas transfer (air-water and water-sediment), from the scaling of the viscous and diffusive sub-layer heights and find a proportionality constant of $(2\pi)^{-1}$.

The energy dissipation rate can be measured in the field using Doppler velocimeters. *Zappa et al. (2007)* reported field measurements of k_w and ϵ_0 made over a wide range of conditions, in a coastal zone, a river estuary, a large tidal freshwater river, and an artificial ocean (Biosphere2). The authors find good agreement with (2.41) and derived a proportionality constant of 0.42 ± 0.13 . This is 1% of the answer to life, the Universe, and everything (*Adams, 1979*). The relationship (2.41) remains to be tested on the open

ocean.

2.4.8 Summary of Transfer Velocity Models and Schmidt Number Scaling

The different air-sea gas transfer models can be summarised in the form

$$k_w \propto u_* Sc^{-n} \quad (2.42)$$

Thus the Schmidt number, which depends on temperature, salinity and the molecular properties of the gas, can be used to scale k_w for different physical conditions and gases using:

$$k_{w1}/k_{w2} = (Sc_1/Sc_2)^{-n} \quad (2.43)$$

with the Schmidt number dependency n . The two-film model (Sec. 2.4.1) implies $n = 1$, because of $k_w = D/Z$, while measurement results from wind-tunnels indicate Schmidt number dependencies of $n = 2/3$ for smooth surfaces as predicted by (Deacon, 1977) and $n = (0.5 - 0.6)$ for a surface ruffled by waves (Jähne *et al.*, 1984), as also used by the surface renewal model (Soloviev, 2007). Gas transfer velocities are typically normalised to a common Schmidt number (either 600 or 660; the values for CO₂ in fresh and salt water at 20°C, respectively). This allows comparison between the transfer of different gases and under different physical conditions.

Wind tunnel studies show a transition from the smooth to the rough surface regime at wind speeds of approximately 3 – 4 m s⁻¹ (Jähne *et al.*, 1987). For field studies at low wind speeds the transition of the Schmidt number exponent from 2/3 to 1/2 can add additional uncertainty to the

estimation of the scaled transfer velocity k_{660} .

2.5 Bulk Flux Formulations

Knowledge of the sea surface turbulent fluxes (momentum, latent and sensible heat, trace gases) is important for understanding air-sea interaction, forcing of ocean and atmosphere models, as well as numerical weather prediction (*Brunke et al.*, 2003). Direct eddy covariance measurement of surface fluxes are however limited to rare, relatively short field experiments and a few long term measurement sites. For modelling purposes and if direct measurements are not available during an experiment, it is necessary to use bulk aerodynamic algorithms to estimate the fluxes from more easily measured bulk meteorological variables (e.g. air and sea temperature, humidity, wind speed, and gas concentration gradients).

These bulk algorithms are based on MOST, which links the surface fluxes to the logarithmic profiles (see (2.1) - (2.3)). The turbulent fluxes are directly related to the bulk measurements by defining exchange coefficients:

$$C_D = \frac{u_*^2}{SU} \quad (2.44)$$

$$C_E = \frac{u_* q_*}{S(q_s - q_a)} \quad (2.45)$$

$$C_H = \frac{u_* t_*}{S(T_s - T_a)} \quad (2.46)$$

where C_D , C_E and C_H are the exchange coefficients for momentum, moisture, and sensible heat, respectively. The subscripts s and a mean ocean surface and bulk air values. Temperature and gas concentrations are usually not

measured exactly at the surface but in the bulk water body (e.g. at 5 m depth) and the surface values are extrapolated. U is the vector average wind speed relative to the sea surface, and

$$S = \langle \sqrt{(u^2 + v^2)} \rangle = \sqrt{\langle u \rangle^2 + \langle v \rangle^2 + w_g^2} \quad (2.47)$$

is the scalar average wind speed relative to the sea surface that includes the gustiness (wind variability) parameter w_g . Gustiness allows the scalar fluxes to remain non-zero and promotes smooth variation of the scalar transfer coefficients as the mean vector average wind speed approaches zero (*Fairall et al.*, 2011). The gustiness is assumed to be proportional to the convective scaling velocity,

$$w_g = \beta_g W_* \quad (2.48)$$

with $\beta_g \approx 1.25$ (*Fairall et al.*, 1996a) and,

$$W_*^3 = \langle w'b' \rangle z_i \quad (2.49)$$

where $\langle w'b' \rangle$ is given by (2.4) and z_i is the height of the atmospheric boundary layer (ABL), which is often assumed to be 600 m.

Bulk algorithms differ in how the exchange coefficients are parameterised and how waves are considered in the parameterisation of the roughness length for momentum flux (*Brunke et al.*, 2003).

2.5.1 The COARE-Algorithm

One of the most reliable and widely used bulk flux algorithms is COARE 3.0 (Brunke *et al.*, 2003). The first version of the Coupled Ocean-Atmosphere Response Experiment flux algorithm (COARE 2.0) was published by Fairall *et al.* (1996a). Inputs are the bulk measurements of wind speed, humidity, bulk air and water temperature, rain rate R_r , down welling radiation, long and short wave, (R_{\downarrow} , $R_s \downarrow$). The COARE algorithm approximates surface values T_s and q_s , atmospheric stability, gustiness, and the aerodynamic roughness length (2.10) in iterations, and incorporates submodels to represent the millimeter-scale cool skin near the interface and the diurnal warm layer in the upper few meters of the ocean (Fairall *et al.*, 1996b).

The first version COARE 2.0 was tuned to 1622 (50 min average) measurements of surface fluxes of momentum, heat, and sensible heat on board the R/V *Moana Wave* in the equatorial pacific, covering a wind speed range from 0.5 to 10 m s⁻¹. Version 3.0 was based on 2777 1-hour covariance flux measurements and tested with 4439 independent measurements (Fairall *et al.*, 2003). The Charnock coefficient α in (2.10) was modified from a constant value to a piecewise linear function. Fairall *et al.* (2003) stated an accuracy of 5% for wind speeds of 0 to 10 m s⁻¹ and of 10% for the range 10 to 20 m s⁻¹. Hare *et al.* (2004) added an air-sea gas transfer parameterisation for CO₂ based on the surface renewal model (Fairall *et al.*, 2000; Soloviev and Schlüssel, 1994), utilizing direct measurements from the GasEx experiments (McGillis *et al.*, 2001a,b, 2004). This was extended by Fairall *et al.* (2011) for Ozone and DMS (COARE 3.1). The most recent update, COARE 3.5, was made by Edson *et al.* (2013), who excluded all ship based measurements from the determination of α in (2.10), in order to

minimise uncertainty caused by air flow distortion.

2.6 The Eddy Covariance Method

2.6.1 Principle

The vertical flux of a scalar quantity c can be measured directly as the covariance of the turbulent fluctuations of the vertical wind speed w and of the scalar concentration n_c . This is called eddy covariance (EC). The principle is illustrated in Fig. 2.4.

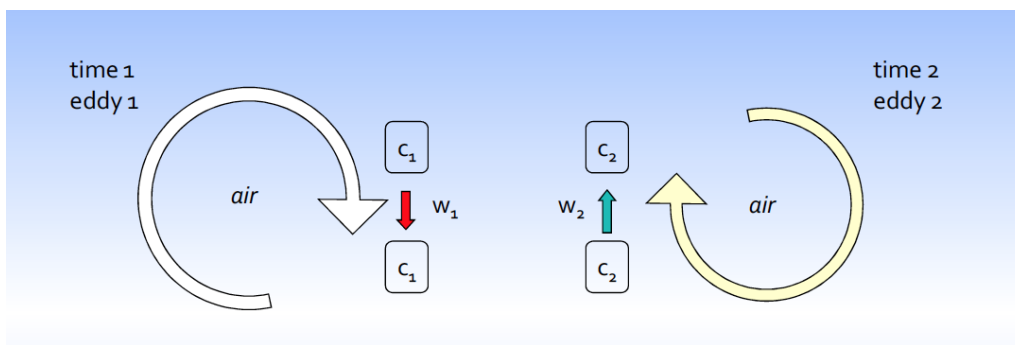


Figure 2.4: Schematic of the transport of a quantity c by turbulent motion. Adapted from (*Burba and Anderson, 2010*).

The validity of the EC method is based on several assumptions: (i) A spacially homogeneous and temporally stationary turbulence field is required, so that a time series measured at a single point can be used instead of the theoretically required ensemble of simultaneous measurements. (ii) The measurement height must be within the constant flux layer. (iii) The wind field must be described in the stream line coordinated system, where the average wind speed is given by $U = \langle u \rangle$ and the averages of the cross wind

and the vertical wind speed are zero ($\langle v \rangle = \langle w \rangle = 0$).

If these requirements are fulfilled, the vertical flux of the scalar (e.g. the CO₂ concentration) is the given by:

$$F_c = \langle w' n'_c \rangle + \langle w \rangle \langle n_c \rangle \quad (2.50)$$

where the Reynolds decomposition of the vertical wind speed $w = \langle w \rangle + w'$ and of the scalar concentration $n_c = \langle n_c \rangle + n'_c$ is used. The first term is the covariance of the quantity of interest with the vertical wind speed. The second term represents the mean flow contribution. For trace gases, this term can be significant and needs to be accounted for (*Webb et al.*, 1980). Alternatively the flux can be computed from the fluctuations of the mixing ratio in respect to the dry air density $x_c = n_c \rho_d^{-1}$:

$$F_c = \langle \rho_d \rangle \langle w' x'_c \rangle. \quad (2.51)$$

The density correction term in (2.50) can be of the order of 10% for moisture fluxes. For CO₂ the correction can be larger than the flux itself (*Webb et al.*, 1980). The effect of air density fluctuations on the direct CO₂ flux measurements is discussed in more detail in Sec. 5.1.

2.6.2 The Air-Sea CO₂ Flux Package

A minimal setup for Eddy Covariance flux measurements from a moving platform consists of the following components (*Edson et al.*, 1998)

- 3D sonic anemometer for fast wind speed measurement
- 3D motion sensor, compass, and GPS for correction of the wind vector

for platform motion and tilt

- Fast responding gas-analyser(s) and temperature and pressure sensors

There are two different ways for measuring the fluctuations of the H₂O and CO₂ concentrations:

- a) An open-path gas analyser (OP) is positioned close to the sonic anemometer to directly measure the trace gas concentrations in the atmosphere. This is the most direct way to measure the flux, but air density fluctuations and sea spray lead to extremely large biases in the flux measurement (see Sec. 2.6.8).
- b) The air is sampled with a long tube and measured away from the intake with a closed-path gas analyser (CP). This requires the usage of a pump and can lead to degradation of the flux signal by the attenuation of fast fluctuation through interaction with the tubing walls. On the other hand the accuracy of the gas measurement can be enhanced by preconditioning the sample air, mainly via attenuation of the temperature and water vapour fluctuations.

Both approaches have their specific advantages as will be discussed in Sec. 2.6.7.

2.6.3 Time Resolution and Averaging Time

The calculation of fluxes with (2.50) or (2.51) requires the wind speed and gas concentration to be measured fast enough to cover high frequency turbulent motion, and averaged over a time period long enough to include the low frequency turbulence. To minimize aliasing, the sample frequency has to be twice the highest frequency, which needs to be resolved. The relative

importance of fast and small eddies compared to the large and slower ones depends on the measurements height: the closer to the surface, the higher the measurement frequency needs to be. On the other hand, the eddy size is limited roughly by the measurement height, thus the contribution of large eddies to the flux and the error made by a limited averaging time is reduced. The optimal length of the time averaging interval is a trade-off between making it long enough for capturing the contribution from large eddies, while still fulfilling the requirement for stationarity. Typical averaging times range between 10 minutes and 1 hour.

2.6.4 Spatial Sensor Separation

The wind speed and the scalar of interest (e.g. humidity or CO₂ concentration) are measured with two different instruments. Thus a separation of the measurement volumes cannot be completely avoided. If the separation is parallel to the mean wind vector, it results in a delay between the two recorded time series for w' and x'_c and can be accounted for by shifting the two time series to obtain the maximum covariance of the two signals. Any separation orthogonal to the wind vector leads to a loss of small scale correlation between the two signals. This can be accounted for by applying corrections for the loss of high frequency fluctuations (see Section 3.2.7). To avoid large corrections the sensors should be closely collocated, however under careful consideration of the potential distortion of the air-flow (see Section 2.6.6).

2.6.5 Motion Correction

Wind measurements taken on a moving platform need to be corrected for:

1. tilt of the anemometer due to the pitch, roll, and heading variations of the platform;
2. relative velocities at the anemometer due to rotation of the platform about its local coordinate system axes;
3. translational velocities of the moving platform with respect to a fixed frame of reference

Edson et al. (1998) present two methods to measure the platform motion and correct the wind speed measurement. *Miller et al.* (2008) improved the motion-correction procedure by accounting for misalignment between anemometer and motion sensor. This is discussed in more detail in Chapter 4.

2.6.6 Air-Flow Distortion

Air-sea flux measurements require a platform, typically a vessel or buoy. The presence of the platform superstructure and the instruments itself cause a distortion of the wind field and lead to acceleration or deceleration of the wind speed. This can lead to errors in the wind speed in the order of 10%, even at well exposed measurement locations, (e.g *Yelland et al.*, 2002; *Popinet et al.*, 2004). Besides the bias in the mean wind speed measurements, the flow distortion can also lead to biased flux measurements (*Wyngaard*, 1981; *Oost et al.*, 1994). *Edson et al.* (1998) reported an overestimation of 15% in the momentum flux, when they compared simultaneous measurements on the R/V *Wecoma* and the research platform R/P *Flip*, which they assumed

to have minimal flow distortion effect. Similar findings were reported by *Pedreros et al.* (2003) for comparisons between a Vessel and an ASIS buoy.

In order to minimise the effect of flow distortion, the flux instrumentation is usually mounted at an arm pointing out from the bow mast and flux measurements are restricted to a wind sector where minimal flow distortion effects are expected.

Numerical air-flow distortion models for mean wind speed and height displacement of the air flow are reported by *Yelland et al.* (1998); *Popinet et al.* (2004); *O'Sullivan et al.* (2013). Usually the direct flux measurements themselves are only corrected for the mean tilt of the airflow. However *Oost et al.* (1994) performed additional air flow distortion corrections to the direct flux measurements similar to the corrections proposed by *Wyngaard* (1981). A tilt and flow distortion correction method for fluxes based on Large Eddy Simulation (LES) was presented by *Griessbaum and Schmidt* (2009), who found corrections of 8 – 15% for scalar fluxes and 27% for the momentum flux during a study on a tower (inland). A more detailed review about air-flow distortion is given in Sec. 4.1 and a new approach to reducing the flow distortion error in direct flux measurements on moving platforms is presented in Sec. 4.2.

2.6.7 LICOR Open- and Closed-Path Systems for CO₂ Flux Measurements

The gas analyser used in this thesis are broadband non-dispersive infrared gas analysers (IRGAs) of the types LI-7500 and LI-7200 manufactured by the company LICOR. They offer a robust sensor design and allow for open-path (OP) configurations where the absorption path is freely ventilated (e.g.

LI-7500) and can be situated close to the anemometer measurement volume (see Fig. 2.5).

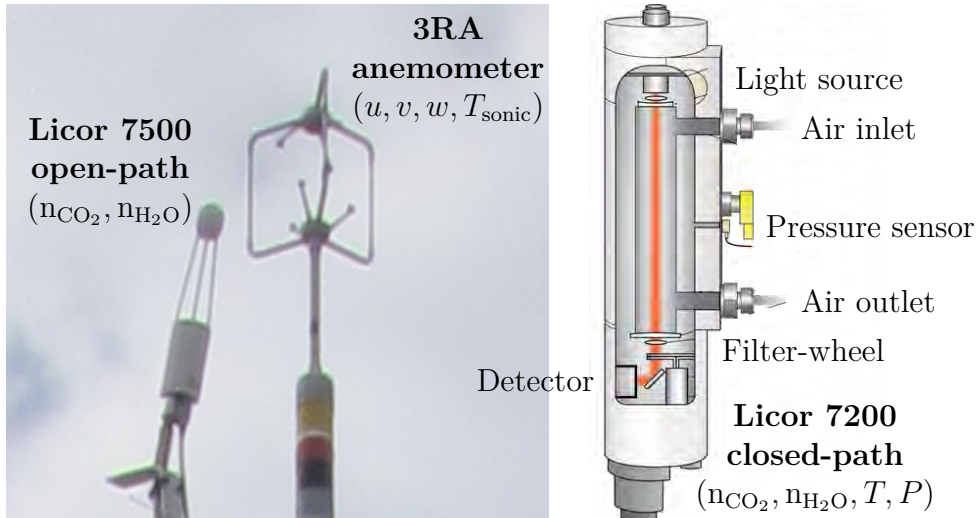


Figure 2.5: On the left photo of a Licor 7500 open-path gas analyser side by side with a 3RA (Gill) sonic anemometer. On the right a drawing of a Licor 7200 closed-path gas analyser (from the Licor 7200 manual). The 7500 and the 7200 model have the same optical setup.

The same IRGA system can also be deployed as a closed-path system where the measurement volume is situated in a closed chamber that is ventilated with sample air by means of a pumping system. A clear advantage of this system, relative to the open-path, is that the air density fluctuations i.e. pressure, temperature, and humidity can be controlled and measured more accurately to reduce the magnitude of the Webb-correction (e.g *Rannik et al.*, 1997; *Miller et al.*, 2010). Recently, *Miller et al.* (2010) showed that the application of a Nafion diffusion dryer upstream of the gas analyser can significantly increase the quality of the CO₂ flux estimate by reducing water vapour fluctuations by 97%, and thus making corrections for density fluctuation or cross sensitivity caused by water vapour negligible (see Sec. 2.6.8). Another advantage is that the tubing, which is used to draw the

sample air to the instrument, can be located much closer to the anemometer sample volume than a bulky gas analyser. Clear disadvantages are potential loss of high frequency fluctuations and increased power and maintenance requirements of a pumping system. The attenuation of the trace gas signal can be minimised by appropriate selection of tubing length, diameter, and pumping speed. Several methods to estimate the undersampling of high frequency turbulence are reported by (*Marandino et al.*, 2007; *Blomquist et al.*, 2010). Recently, fast responding cavity ring down spectrometers (CR) for CO₂ have become available (e.g. PICARRO) and are being used for air-sea flux measurements (see *Blomquist et al.*, 2014). Other trace gas fluxes, such as DMS can, at present time, only be measured with closed-path instrumentations.

2.6.8 Cross Sensitivity to Water Vapour

Over land, CO₂ flux estimates obtained by open-path sensors are considered the standard against which closed-path setups are evaluated to determine the effects of the tubing (*Leuning and King*, 1992). In contrast, the use of open-path sensors over the ocean gives gas transfer rates that are an order of magnitude larger than those deduced with the tracer methods (e.g. *Kondo and Osamu*, 2007). *Prytherch et al.* (2010a) argued that this discrepancy is due to cross sensitivity to water vapour. They presented a novel correction method, named after Peter K. Taylor (PKT), for open-path sensors. *Lauvset et al.* (2011) applied the PKT correction to open-path flux measurements made in the Greenland Sea and found the fluxes estimates comparable with the established parameterisations. The PKT method, however, is an order of magnitude correction without clear physical foundation - the obtained

data sets show much larger scatter than for closed-path measurements. By now the only comparative study of open- and closed-path EC systems at sea was published by (*Kondo and Tsukamoto, 2012*), who measured CO₂ and water vapour fluxes at low wind speeds (2.5 – 5.4) m s⁻¹ in the equatorial Pacific using a Licor 7500 open-path and a Licor 7000 closed-path sensor. No PKT correction was applied to the data set. The authors argued that the lenses of the open-path sensor were cleaned regularly. The CO₂ flux results for both analysers are similar to those obtained in a previous study with an open path (*Kondo and Osamu, 2007*) and an order of magnitude higher than expected from established parameterisations. Chapter 5 provides an in-depth discussion of the cross sensitivity effect and the PKT correction method.

2.6.9 Resolution Requirement for the CO₂ Sensor

At sea, where the concentration gradients in CO₂ are typically an order of magnitude smaller than over source or sink areas on land, additional platform motion and water vapour flux present strong noise sources. This leads to much higher requirements for the gas sensor resolution for EC flux measurements. *Rowe et al. (2011)* estimated for typical conditions over the ocean, that for a CO₂ sensor with a resolution of (0.2 – 0.3)ppm, a partial pressure gradient of $\Delta p\text{CO}_2 > 100\text{ppm}$ would be necessary to obtain a contribution of the sensor noise of less than 10% to the flux uncertainty. However, the air-sea gradient over most of the open ocean is smaller than 20ppm, leading to a strong need for a sensitivity improvement. In the above estimation *Rowe et al. (2011)* assumed that the root mean square (RMS) noise of the sensor is not correlated with the wind speed signal and is thus

reduced by the long time averaging in the covariance calculation. This implies that the resolution of the analog-to-digital (A/D) conversion is the ultimate limit of the sensors capability to resolve gas fluctuation: for the LI-7500 sensor this is 0.003 ppm instead of the RMS of 0.11 ppm (*Miller et al.*, 2010).

3 Field Experiments and Data Analysis

This chapter provides an overview of the field work conducted within the framework of this thesis. The three campaigns took place in very different parts of the ocean (North Atlantic, South Pacific, and Subtropical North Atlantic) and were guided by different research objectives (physics of air-sea gas exchange, influence of the marine biota on aerosol production, and the North Atlantic salinity maximum, respectively). The three experiments are described in Sec. 3.1.

Eddy Covariance at sea is a method based on many assumptions (see Sec. 2.6) and requires large corrections (*Edson et al.*, 1998). The EC method requires elaborate filtering (quality control) which is necessary in order to avoid biased results. The reported measurements of air-sea CO₂ fluxes exhibit tremendous scatter and require significant and (partially empirical) corrections (*Prytherch et al.*, 2010a). Section 3.2 describes in detail the multiple steps of the analysis involved in the EC method. This is illustrated with examples taken from the collected data sets.

3.1 Ship Borne Experiments

3.1.1 Knorr11 Gas-Exchange Study in the North Atlantic

The Knorr11 experiment aboard the Woods Hole Oceanographic Institution (WHOI) R/V *Knorr* in the North Atlantic Ocean was specially designed to increase the observational data base for gas transfer in a region of the oceans where biological activity results in exceptionally large air-sea DMS and CO₂ fluxes (*Bell et al.*, 2013). The cruise started June 24th, 2011 at Woods Hole, Massachusetts, USA (41.53° N, 70.68° W; Fig. 3.1) and ended in the same place on July 18th of the same year. Roughly half of the cruise was spent in the highly productive, high latitude waters of the North Atlantic algae bloom. Special care was taken not to miss any of the passing low-pressure systems. This was achieved by observing storm forecasts provided by the European Centre for Medium-Range Weather Forecasts (ECMWF) and navigating the ship into the predicted storm tracks, ahead of time.

During this experiment, continuous measurements of air-sea gradients and fluxes of DMS and CO₂ were conducted by the teams of Professor Eric Saltzman (UC Irvine), Dr. Scott Miller (SUNY) and Dr. Brian Ward (NUIG). Two independent camera systems recorded sea state and whitecap-coverage. The Air Sea Interaction Profiler (ASIP) was deployed several times during the experiment. The ship's crew provided continuous measurements of mean meteorological parameters, as well as profile measurements of conductivity temperature and density (CTD).

Figure 3.2 shows the setup used during the Knorr11 experiment. The apparent 3D-wind speed was measured at 10 Hz with two Csat3 sonic

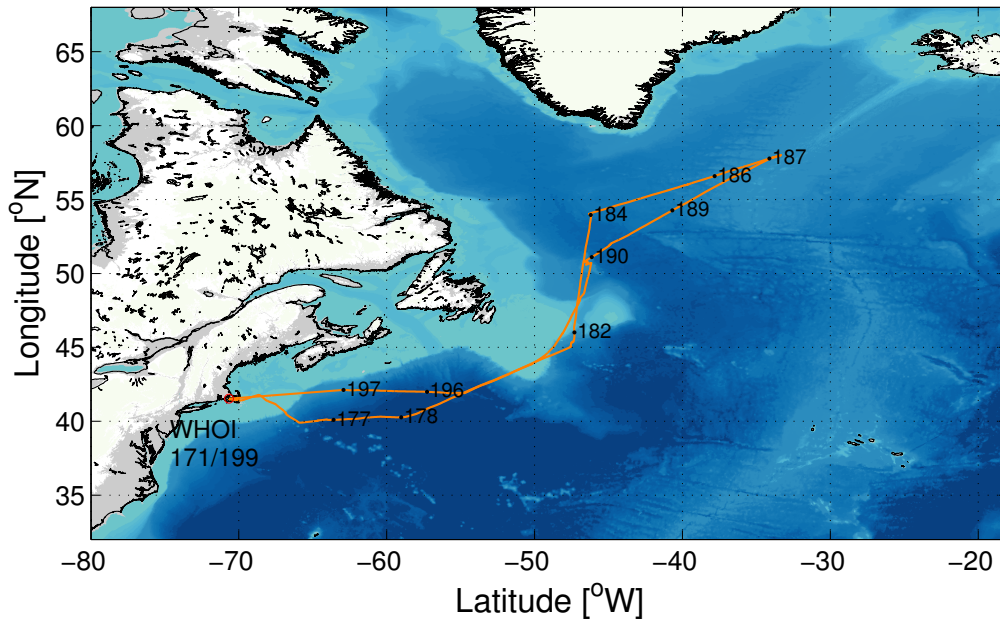


Figure 3.1: Map showing the cruise track of the Knorr11 experiment, starting from the Woods Hole Oceanographic Institute on June 24th and returning there in July 18th. Start and end of the cruise and selected dates under-way are marked in black as day of the year (doy) 2011.

anemometers mounted on the bow-mast. A 3D Inertial Motion Unit (IMU) located half a meter behind the anemometers recorded instantaneous 3D accelerations $\ddot{\mathbf{x}} = (\ddot{x}, \ddot{y}, \ddot{z})$ and angular rates $\boldsymbol{\Omega} = (\Omega_x, \Omega_y, \Omega_z)$ at the same sample frequency. A GPS unit was used to obtain slow (1 Hz) variations of course (COG) and position of the ship. These measurements were provided by Dr. Scott Miller. The data were recorded on a CR3000 data logger (Campbell). The heading (HDG) was obtained from the ship's own navigation system.

Carbon dioxide and water vapour concentrations were recorded by two dispersive Infra Red Gas Analysers (IRGA) situated in a laboratory van on the foredeck, which were connected with the bow mast via a 35 meter long tubing, 1 cm inner diameter (ID). A rotary van pump (Gast) was used to maintain a high flow rate of 17 slpm (standard litre per minute). The

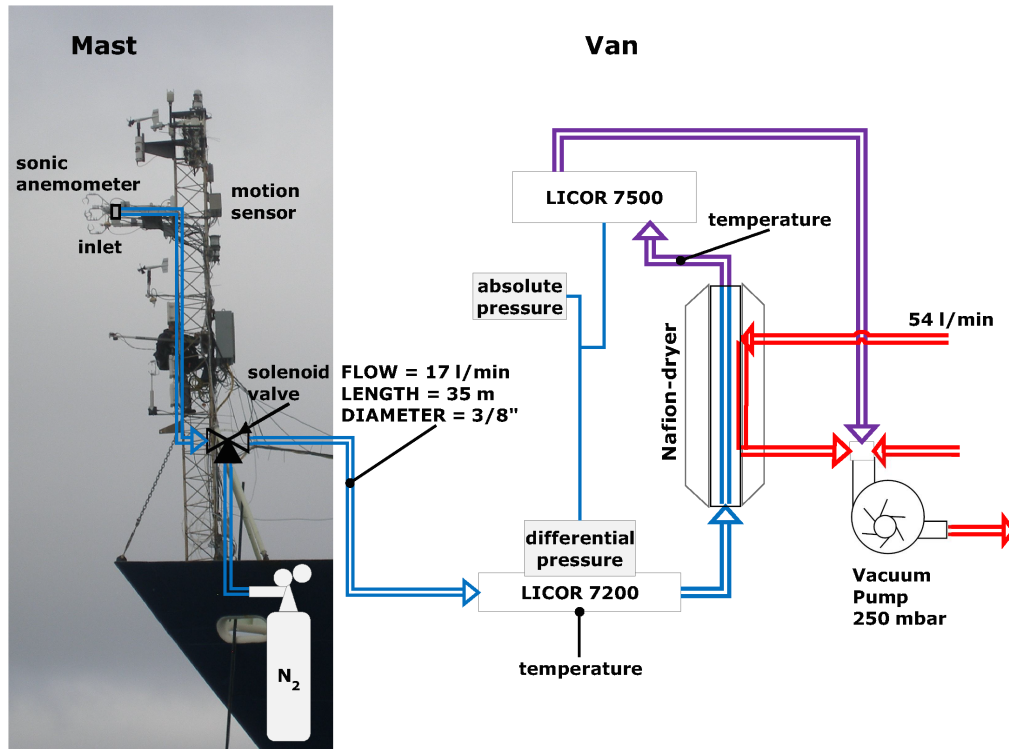


Figure 3.2: Air-sea flux setup as deployed during the knorr11 experiment. Wind speed and ship motion were measured at the bow mast. CO_2 and H_2O concentrations, pressure and temperature were measured using closed-path gas analysers situated in a laboratory van on the foredeck. The sample air was collected via a 35 m long inlet tubing.

first IRGA, a LI-7200 (Licor), measured the CO_2 and H_2O densities in the unchanged sample air. Here, built-in differential pressure and temperature sensors were used for the conversion to gas mixing ratios. The second IRGA, a LI-7500, was situated down-stream of a diffusion dryer (Nafion), in order to improve the quality of the CO_2 signal by removing the ambient water vapour fluctuations (as per *Miller et al.*, 2010). External pressure CPT6100 (Mensor) and temperature SEB39 (Seabird) sensors were used with this LI-7500. All measurements were recorded at 10 Hz with an embedded Linux computer (UC 7420 Moxa). The fast measurements at the bow mast and the concentration measurements in the Laboratory van were later synchronized

using an analogue sawtooth signal that was recorded by both systems. Further, a solenoid t-valve was installed in the sample line, close to the sample inlet, to allow for a sudden change of gas concentration (injection of Nitrogen) at a recorded moment in time. This “puff-test” was used estimate the travel time of the sample air from the inlet to the IRGAs.

The knorr11 experiment has so far led to the following publications (*Bell et al.*, 2013; *Sutherland et al.*, 2013, 2014). An insight to the life on board can be gained from the on-line blog, which was written in team effort by the science crew (<http://bloomcruise.blogspot.ie/>).

3.1.2 Surface Ocean Aerosol Production Study (SOAP)

This experiment was conducted on board the R/V-*Tangaroa* from February to March 2012 in the South Pacific, south west of New Zealand (Fig. 3.3). Like for the Knorr11 cruise, this experiment took place during high biological productivity. The Sub-Tropical Front that runs eastwards along the Chatham Rise is characterised by intensive phytoplankton blooms that provide large sinks for CO₂ and sources for DMS. A preliminary survey of the area during the PreSOAP voyage revealed that the blooms of different phytoplankton groups have different characteristics in there DMS emissions and CO₂ consumption. In order to conduct parallel DMS/CO₂ gas exchange measurements it is necessary to find sufficiently strong gradients for both gases. The main objective of SOAP was to analyse the influence of marine biota on aerosol production and size distributions as well as the influence of aerosol abundance and size distribution to the formation of clouds (e.g. *Quinn and Bates*, 2011). My research aim for this cruise was to study sources of uncertainties in the direct eddy covariance measurements of

the CO_2 flux and particular to compare open- and closed path flux setup, to test the PKT correction (*Prytherch et al.*, 2010a).

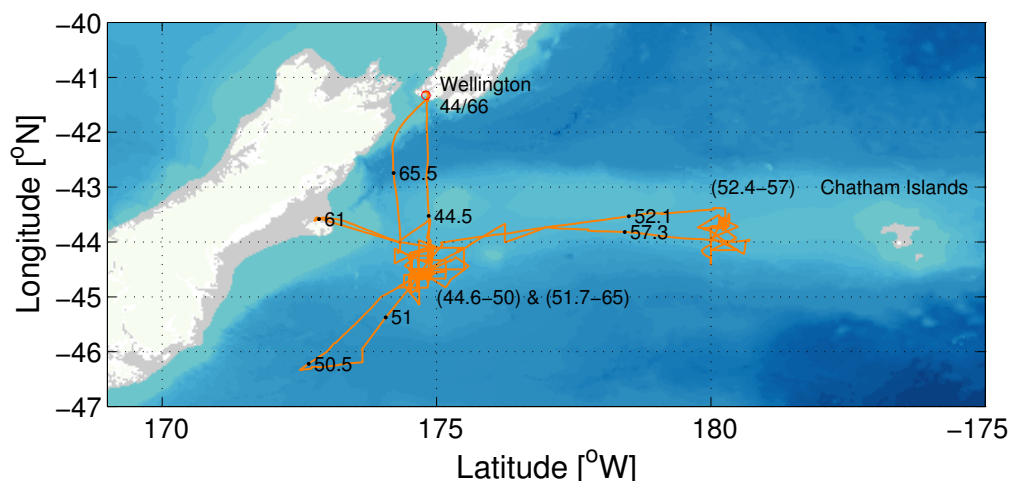


Figure 3.3: Map showing the cruise track of the SOAP experiment (February/March 2012) west of New Zealand. The cruise started and ended in Wellington, with a short stop in Lyttleton harbour near Christ Church. Dates of certain ship positions are indicated as days of the year 2012 and can be used for comparison with the time series in Figs. 5.2-5.4.

The international science team brought in a large range of complementary measurement capabilities, e.g., Volatile Organic Compounds (VOC), atmospheric halocarbons, condensation nuclei counts, cloud condensation nuclei, direct DMS-, aerosol-, and CO_2 -flux measurements, near surface mixing and turbulence, gas-concentration gradients, whitecap-coverage, and in-vitro studies on sea water samples*. The CO_2 flux setup and measurements during SOAP are described in detail in Section 5.2.

*A special issue in Applied Chemistry and Physics http://www.atmos-chem-phys-discuss.net/special_issue197.html combines all present and future publications emerging from SOAP. More information about SOAP can also be found under <http://www.niwa.co.nz/atmosphere/research-projects/soap>.

3.1.3 SPURS-MIDAS experiment

The MIDAS experiment was an in-situ contribution to the international Salinity Processes in the Upper ocean Regional Study (SPURS) (Fig. 3.4). It took place on board the R/V *Sarmiento de Gamboa* leaving port in Las Palmas on March 16th and returning to the Azores on April 17th 2013.

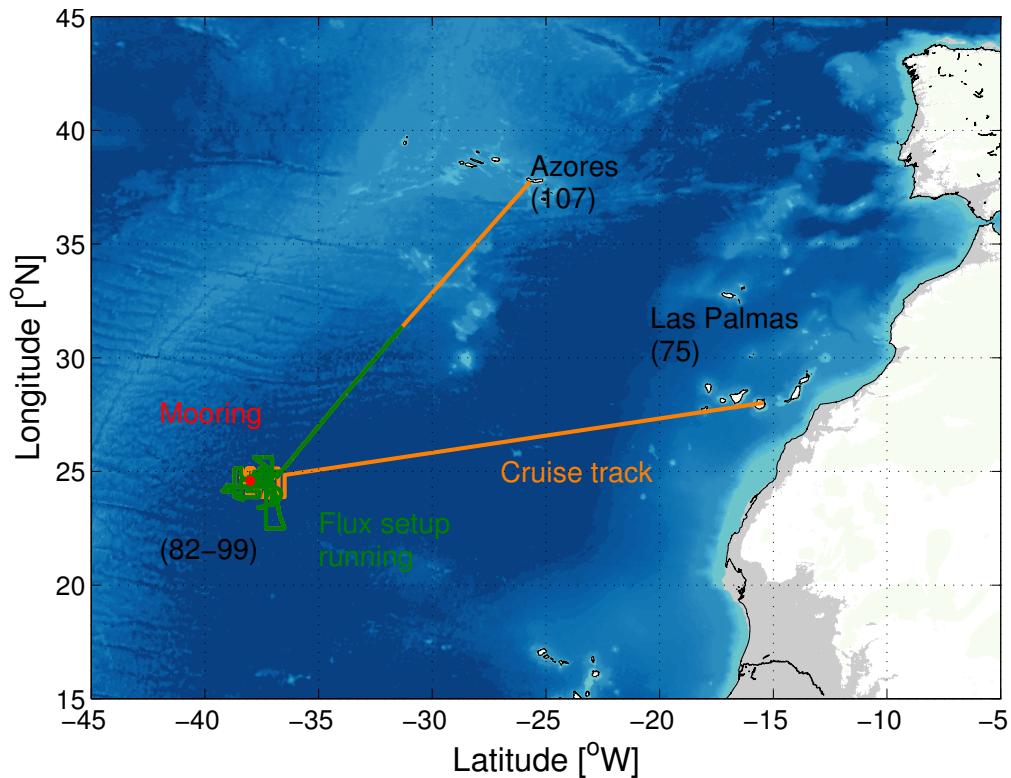


Figure 3.4: Map showing the cruise track of the SPURS-MIDAS experiment in spring 2013. The position of the permanent mooring is indicated as a red dot. The part of the track where the flux system was up and running is marked in dark green. The ship left port in Las Palmas on March 16th and arrived the Azores on April 17th. These dates and the period during which the ship was close to the mooring are indicated as days of the year 2013. Compare also the time series in Fig. 4.2.

The majority of the time was spent within the Salinity Maximum of the Tropical North Atlantic, and in the proximity of a permanent surface mooring at (24.58° N, 38° E), which was deployed by WHOI. The goals

of the SPURS experiments, which were conducted in 2012 and 2013, were (i) to study the mechanisms of formation and permanence of the largest ocean salinity maximum in the centre of the North Atlantic subtropical gyre, and (ii) to validate remote sensing products for salinity information, i.e., Soil Moisture and Ocean Salinity (SMOS). The Air-Sea Physics Lab, NUIG contributed by operating ASIP and with continuous EC flux measurements of momentum, sensible and latent heat, and CO_2 . For this purpose and the NUIG flux mast was installed at the bow of the R/V *Sarmiento de Gamboa*.

In Chapter 4, the wind speed and momentum flux measurements from the bow mast are compared with wind speed measurements and COARE 3.0 bulk flux estimates from the surface mooring. I also used these observations to develop a new concept for motion-tilt correcting the 3D-wind velocity measurements to allow direct EC flux measurements from moving platforms.

3.2 Flux Data Analysis

This section describes how the direct flux measurements are obtained from the raw measurements of platform motion, apparent wind speed, gas concentrations, pressure, and air temperature. Examples from the three experiments are used to illustrate the magnitude of the performed corrections.

3.2.1 Motion Correction

As described in Sec. 2.6.1, it is fundamental to all flux calculations to find the stream line coordinate system for the true wind field (u, v, w) . However, as the wind measurements are performed on a moving platform, the apparent

wind vector \mathbf{u}_m first needs to be rotated into the earth coordinate frame, i.e., corrected for platform tilt, on a sample by sample basis and then corrected for the platform velocity, in order to obtain the true wind speed in a fixed earth coordinate frame:

$$\mathbf{u}_{\text{true,e}} = \mathbf{T}_{ep} \mathbf{u}_m + \mathbf{v}_{\text{ship}} \quad (3.1)$$

Here \mathbf{T}_{ep} denotes the rotation from the platform coordinate system (indicated by subscript p) into the earth reference system (indicated by e), and \mathbf{v}_{ship} is the platform motion relative to earth.

Equation (3.1) is implemented using the motion correction script *motion.m*[†], written by Scott Miller. The script follows the methodology suggested by *Edson et al.* (1998) for an IMU that is fixed to the moving platform, but additionally allows for a mounting offset (distance and tilt) between the motion sensor and the anemometer, (see *Miller et al.*, 2008).

The platform-earth transformation matrix is described by three rotations about the Euler angles,

$$\mathbf{T}_{ep} = \boldsymbol{\Psi}_{ep} \boldsymbol{\Theta}_{ep} \boldsymbol{\Phi}_{ep} \quad (3.2)$$

where the first rotation (roll ϕ_{ep}) is about the x-axis, the second rotation (pitch θ_{ep}) is about the new y-axis, and the last rotation (yaw or heading ψ_{ep}) is about the new z-axis. In a right handed coordinate system, and here only right handed coordinate systems are used, the explicit forms of the

[†]The script *motion.m* is available upon request at <http://asrc.albany.edu/people/faculty/miller/software.php>.

Euler angles are defined as follows:

$$\boldsymbol{\Psi}_{ep} = \begin{bmatrix} \cos(\psi_{ep}) & -\sin(\psi_{ep}) & 0 \\ \sin(\psi_{ep}) & \cos(\psi_{ep}) & 0 \\ 0 & 0 & 1 \end{bmatrix} \quad (3.3)$$

$$\boldsymbol{\Theta}_{ep} = \begin{bmatrix} \cos(\theta_{ep}) & 0 & \sin(\theta_{ep}) \\ 0 & 1 & 0 \\ -\sin(\theta_{ep}) & 0 & \cos(\theta_{ep}) \end{bmatrix} \quad (3.4)$$

$$\boldsymbol{\Phi}_{ep} = \begin{bmatrix} 1 & 0 & 0 \\ 0 & \cos(\phi_{ep}) & -\sin(\phi_{ep}) \\ 0 & \sin(\phi_{ep}) & \cos(\phi_{ep}) \end{bmatrix} \quad (3.5)$$

Ideally the Euler angles could be calculated from a step by step integration of the angular rates observed in the platform frame. In practise, however, this approach can lead to large errors due to small drifts in the angular rate signals (*Edson et al.*, 1998). Alternatively, *Edson et al.* (1998) suggest to use high-pass filtered integration of the angular rates in combination with low-pass filtered heading from the ship's gyroscope and platform orientation calculated from the measured accelerations:

$$\psi = \psi_{LF} + \psi_{HF}, \quad \theta = \theta_{LF} + \theta_{HF}, \quad \phi = \phi_{LF} + \phi_{HF} \quad (3.6)$$

The bias in the apparent wind velocity at the measurement location is given by the sum of: (i) the angular velocity at the relative position of the anemometer with respect to the motion sensor $\mathbf{r}_{ap} = \mathbf{x}_a - \mathbf{x}_p$, and (ii) the linear platform velocity. The latter in turn can be calculated from the integral of the high-pass filtered linear accelerations and the low-pass filtered

velocity obtained from the GPS sensor:

$$\mathbf{v}_{\text{ship}} = \boldsymbol{\Omega} \times \mathbf{r}_{\text{ap}} + \text{HF} \left[\int (\mathbf{T}_{\text{ep}} \ddot{\mathbf{x}} - \begin{pmatrix} 0 \\ 0 \\ g \end{pmatrix}) \right] + \text{LF} [\mathbf{v}_{\text{GPS}}] \quad (3.7)$$

In the original script *motion.m* it is assumed that for \mathbf{v}_{GPS} , the ship's course always equals its heading. This is, however, not always the case; e.g. when the ship is drifting with surface currents. Our data sets, include a significant amount of station measurements, where the ship was pointed into the wind, but potentially drifted sideways. Therefore, *motion.m* was modified to allow for low frequent ship motion where $\text{COG} \neq \text{HDG}$.

Figure 3.5 shows the average of five 12-minute momentum co-spectra, C_{wu} and C_{wv} (along- and cross-wind respectively), with the motion and tilt correction applied. Also shown are the ‘uncorrected’ co-spectra, where only the mean ship velocity was removed from the measured wind speed. The uncorrected co-spectra show large concentrations of energy in the frequency range of the ship motion [0.08 0.25] Hz; for the corrected co-spectra these structures are removed.

The synchronisation of the wind and motion measurements is crucial to the quality of the motion correction. During the SOAP experiment the IMU signal was recorded in analogue and digitised by the CR3000 data logger. It exhibited a 0 – 0.2 second (0-2 sample) delay to the digitally recorded wind speed measurements from the Csat3 anemometers. When not adjusted, the delay leads to a residual motion peak, whose magnitude was about 5 – 10% of the uncorrected peak. To illustrate this effect the example spectra from Fig. 3.5 are shown again in Fig. 3.6, but with artificial delays of ± 1 sec. The power spectra S_u^2 , S_v^2 and S_w^2 are also shown. Curiously, the optimal delay

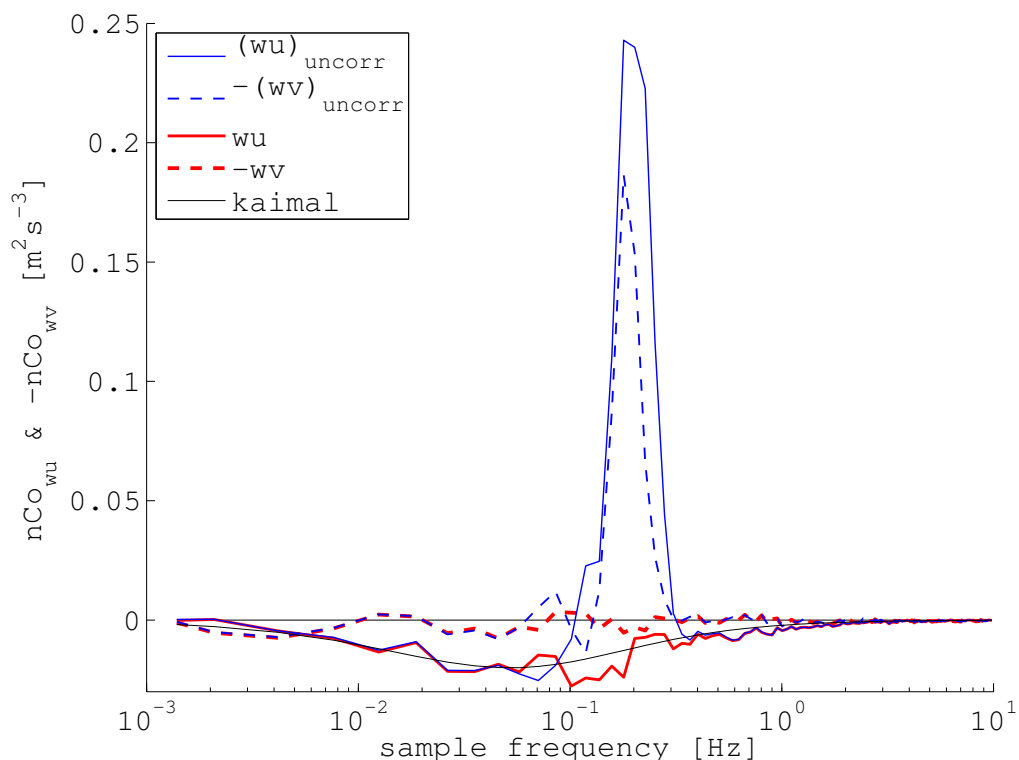


Figure 3.5: Averages of five consecutive 12 min momentum co-spectra from 7.4.2013 3am-4am. Shown are spectra computed from (i) \mathbf{u}_{me} corrected for mean ship velocity and wind vector tilt (blue) and (ii) fully motion and tilt corrected (red). The sign of C_{wv} was inverted in order to save white ink. The expected shape of C_{wu} as per (*Kaimal et al., 1972*) is shown for comparison.

between the IMU signal and $(u, v, w)_m$ is not the same for the three wind speed components. *Schulz et al. (2005)* also reported similar residual motion signals in the two horizontal power spectra (S_u^2 and S_v^2). For the SOAP dataset the delay was optimised by searching for the maximum covariance between w'_{me} and $v'_{ship,z}$. This provided the most successful removal of the motion-peaks from C_{wu} and C_{wv} . For the MIDAS experiment, where both IMU and sonic were recorded digitally, a fixed delay of 0 sec was found to be optimal.

The power spectra exhibit large amounts of energy contained in the low frequency part ($n \leq 0.01$ for S_u^2 , $n \leq 0.1$ for S_v^2 & S_w^2) that are an order of

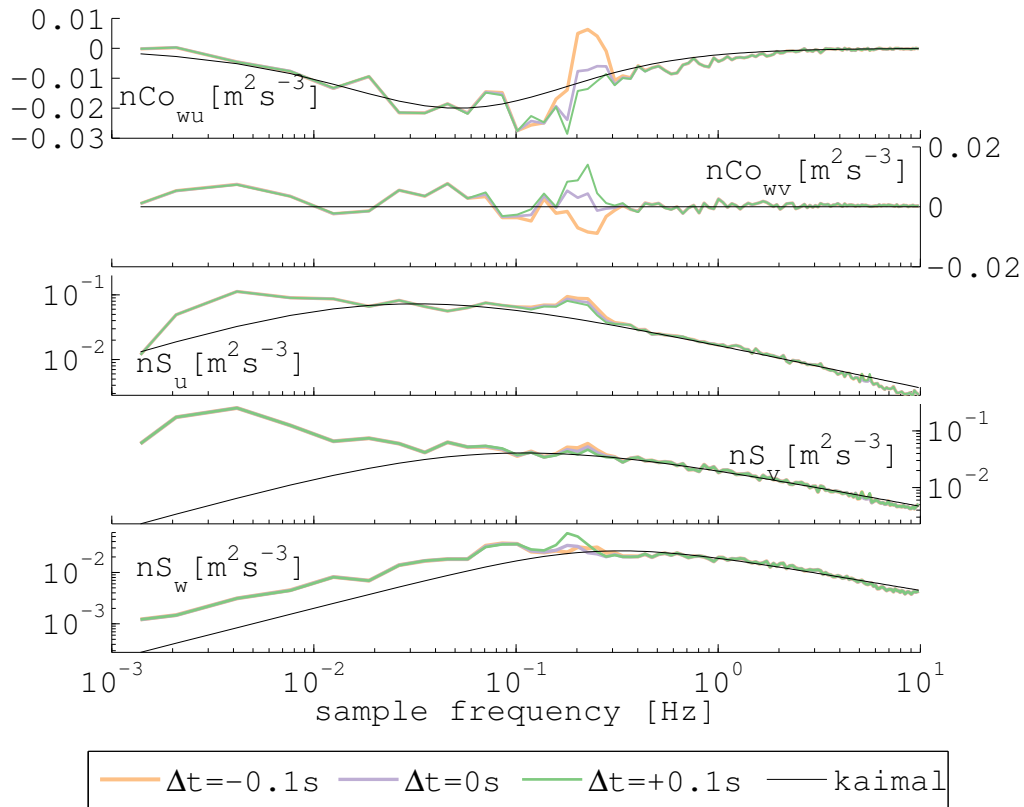


Figure 3.6: Averages of five consecutive 12 min momentum co-spectra and wind vector power-spectra from 7.4.2013 3am-4am for motion corrections performed with a delayed motion signal. Shown are delays of -1 sec, 0 and +1 sec. The expected (*Kaimal et al.*, 1972) shapes are shown as black lines.

magnitude higher than for the average spectra as per *Kaimal et al.* (1972). Power spectra shown by *Schulz et al.* (2005) and *Miller et al.* (2008) exhibit similar features. These authors, however, do not compare them with the Kaimal shapes or discuss the increased energy levels in the power-spectra. These high energy levels in the self-covariances do not show up in the co-spectra which are used to calculate the momentum flux. This makes it unlikely that low frequency ship motion could be the cause for the increased energy levels, since the 3D-ship motions are naturally correlated. The matter was not further investigated, since the direct flux estimates appeared to be unaffected.

3.2.2 Stream Line Coordinate System

After the ship motion is removed from the measured wind speed, the subsequently corrected wind speed ($\mathbf{u}_{\text{true},e}$) needs to be rotated into the stream line coordinate system. *Edson et al.* (1998) adapted the double rotation approach from land based measurements. The wind vector is first yawed around the z -axis to achieve $\langle v \rangle = 0$ and then pitched over the new x -axis to maintain $\langle w \rangle = 0$. This is symbolised by the double rotation matrix (**DR**):

$$\mathbf{u} = \mathbf{DR}(\mathbf{u}_{\text{true},e}) \quad (3.8)$$

In Chapter 4 it will be explained that this approach can lead to biased estimates of the stream line coordinate system and, therefore, to errors in the direct flux measurements. Alternative methods to estimate the tilt of the wind vector are presented there.

3.2.3 Air Density Correction

The two IRGA types (LI-7500 and LI-7200) measure the CO_2 and H_2O number densities n_c and n_v within the measurement volume. Parallel measurements of air temperature T and pressure P in the sample cell were used to calculate the gas mixing ratios on a sample-by-sample basis using:

$$x_c = n_c \left(\frac{P}{RT} - n_v \right)^{-1} \quad (3.9)$$

where $R = 8.31 \text{ J mol}^{-1}\text{K}^{-1}$ is the ideal gas constant.

The pressure sensor provided by the LI-7500 unit does not have a sufficient resolution, therefore a high resolution pressure sensor CPT-6100 is connected

to the sample cell during the experiments. The LI-7200 unit is equipped with the same low resolution pressure sensor to measure ambient air pressure, but a high resolution differential pressure sensor is provided to measure the pressure difference between the sample cell and ambient air. Unfortunately, the range of the differential unit ± 30 mbar is not sufficient for the pressure drop of typically 100 – 200 mbar due to the high flow rate requirement. To overcome this, an absolute pressure unit CPT-6100 was used to measure pressure at a reference point, on a sufficiently close pressure potential, to which the differential sensor is connected (see Fig. 3.2). The pressure in the Licor cell ($P_{LI-7200}$) is then calculated according to:

$$P_{LI-7200} = P_{CPT-6100} + P_{diff} \quad (3.10)$$

where $P_{CPT-6100}$ and P_{diff} are the pressure measurements from the CPT-6100 and the LI-7200 differential pressure sensor, respectively.

3.2.4 IRGA-Motion Sensitivity Correction

The power spectra of the gas mixing ratios $x_{c,m}$ and $x_{v,m}$ obtained from (3.9) show typically increased energy in the frequency range of the ship motion. This has been observed by *Edson et al.* (1998) and *Miller et al.* (2010) and is related to (i) the inertial forces acting on the filter-wheel of gas analyser and (ii) flexing of the structures that separate the detector from the light source. The wheel is positioned between the broad-band IR light source and the measurement volume. It carries four different narrow band filters, which pass wavelength ranges of strong CO₂ and H₂O absorptions and close by reference ranges with weak absorption. The center wavelengths of the band filters for the LI-7200 and LI-7500 are listed in Table 3.1.

Table 3.1: Center wavelengths of the optical filter as per LI-840A Manual (ftp://ftp.licor.com/perm/env/LI-840A/Manual/LI-840A_Manual.pdf). These are the same for the LI-7500 and LI-7200 utilized in this thesis (Frank Griessbaum, personal communication).

Center Wavelength	Symbol	Description
4.26 μm	Ac	strong absorption band for CO ₂
3.95 μm	Ac0	reference for CO ₂
2.595 μm	Av	strong absorption band for H ₂ O
2.35 μm	Av0	reference for H ₂ O

The wheel rotates at a frequency of 140 Hz and the ratios of the absorptances $Ac/Ac0$ and $Av/Av0$ are used to determine the gas concentrations. Due to the inertial forcing by the platform motion the wheel rotates slightly faster or slower, which leads to variations in the ratios that are correlated with the platform motion. The bias signal in the gas concentrations can be of the order of 1 ppm, depending on the individual instrument (see *Miller et al.*, 2010).

During the Knorr11 experiment, the bias in the CO₂ fluxes measured by the LI-7200 was on the order of 1%. The bias in the LI-7500, which has a less rigid construction, was in the order of the CO₂ flux signal and sometimes changed the sign of the flux. *Miller et al.* (2010) suggested to remove the bias signal by decorrelating $x_{c,m}$ and $x_{v,m}$ with the acceleration and rate signal from the IMU:

$$x_c = x_{c,m} - \begin{pmatrix} A_x \\ A_y \\ A_z \end{pmatrix} \cdot \ddot{\mathbf{x}} + \begin{pmatrix} B_x \\ B_y \\ B_z \end{pmatrix} \cdot \boldsymbol{\Omega} \quad (3.11)$$

where the coefficients of A and B are determined by linear regression. This approach was adapted for the analysis of the three data sets.

3.2.5 Cross-Covariance and Flux Calculation

The momentum flux vector is directly computed from the covariance of u , v and w

$$\tau = -\rho_a (\mathbf{i}\langle w'u' \rangle + \mathbf{j}\langle w'v' \rangle) \quad (3.12)$$

For the trace gas fluxes the delay of the time series from the different instruments needs to be accounted for. This delay is caused by the travel time of the sample air in the intake tubing and by potential time delays in the signal recording, in case these are not corrected by the synchronisation. In a first step, the cross-covariance $R_{wx_c}(\delta t)$ is calculated in analogy to (2.13) for time delays $\delta t \in [0 \ \Delta t_{\max}]$. The maximal tested delay (Δt_{\max}) was chosen after calculating the expected travel time from the flow rate and the volume of the tubing. Based on the observed distribution of the maxima of $R_{wx_c}(\delta t)$, and results from the puff-tests, a window of ‘credible’ time delays Δt_c was chosen and maxima of $R_{wx_c}(\delta t)$ were accepted when they were within this range. The flux was calculated as

$$F_c = n_a \langle w'(t)x'_c(t - \Delta t_c) \rangle. \quad (3.13)$$

For intervals where no Δt_c could be defined from the maximum cross-covariance, or where it lays outside of the ‘credible-delay’ interval, Δt_c was interpolated linearly from the nearest intervals.

The latent heat flux was calculated from:

$$Q_{lat} = \rho_a L_{ev} \langle w'(t)x'_v(t - \Delta t_v) \rangle \quad (3.14)$$

where L_{ev} is the latent heat of evaporation.

The sensible heat flux was calculated from the sonic temperature and a correction term (*Burns et al.*, 2012) involving the latent heat flux:

$$Q_{sen} = \rho_a \rho_{cp} (\langle w' T_{sonic} \rangle - 0.51 T Q_{lat} / (\rho_a L_{ev})) \quad (3.15)$$

where ρ_{cp} is the specific heat capacity of air.

3.2.6 Scalar Co-Spectra Example

Figure 3.7 shows normalised co-spectra (i) of temperature, measured by the 3D-sonic (open path), (ii) water vapour, measured by CP-IRGAs before and downstream of a membrane dryer (see Fig 3.2 for the experimental setup), and (iii) CO₂, measured downstream of the dryer. The dry H₂O spectrum was normalised using the flux measured by the un-dried IRGA. The diffusion dryer removed 97% of the flux signal. Also shown is the expected shape of the scalar co-spectrum, computed following *Kaimal et al.* (1972). The spectra are averages of 10 flux intervals of 25 min length, recorded within 6 hours during the SOAP experiment on February 22nd/23rd 2012 (see Chapter 5). The wind speed, heat, and CO₂ fluxes were steady ($u_{10N} = 14 \text{ m s}^{-1}$, $Q_{lat} = -50 \text{ W m}^{-2}$, $Q_{sen} = -49 \text{ W m}^{-2}$, and $F_c = -7.8 \text{ mol m}^{-2} \text{ s}^{-1}$, respectively) and the ship was on station $v_{ship} = 0.5 \text{ m s}^{-1}$ and pointed into the wind (relative wind direction $-24^\circ \leq \alpha \leq 13^\circ$). The large noise in the high frequency part of C_{wx_c} , when compared to the other spectra, is due to the low sensor resolution.

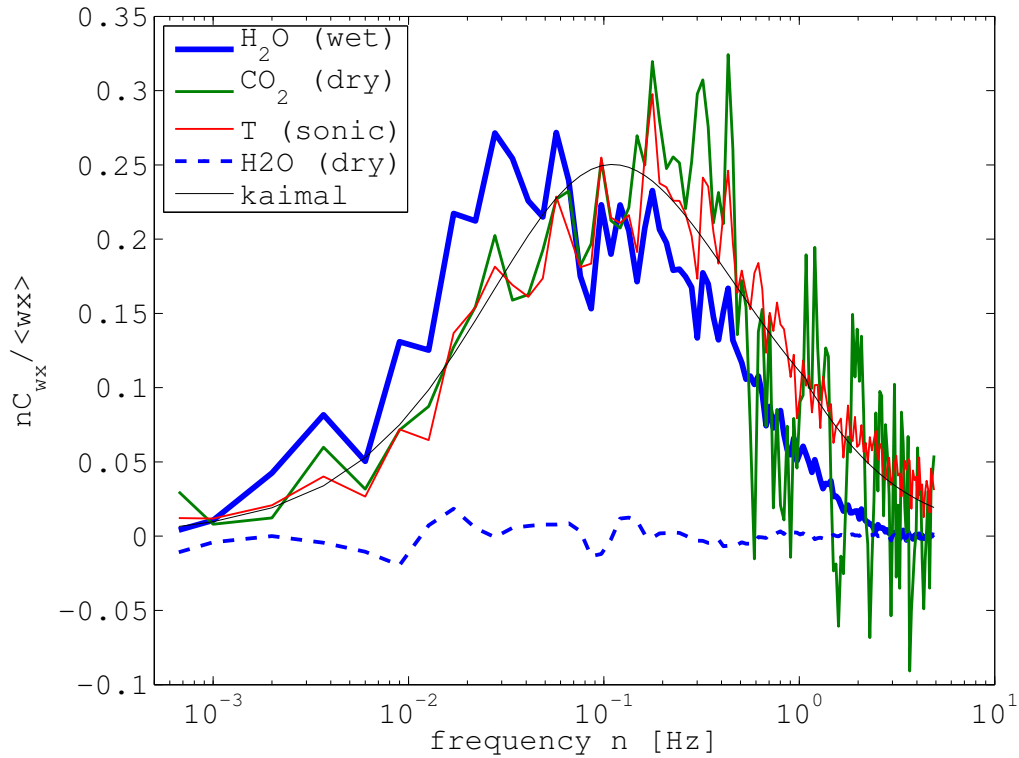


Figure 3.7: Normalised co-spectra of the sonic temperature (red), water vapour (blue), and CO₂ (green). The water vapour spectrum from a dried and un-dried CP IRGA are show. The dry spectrum was normalised against the flux measured by the un-dried IRGA. The spectra are averages of 10 consecutive 25 min flux measurements recorded during the SOAP experiment.

3.2.7 Frequency Corrections

In some of the analysed records large features in the low frequency part of the frequency-weighted co-spectra ($n \leq 10^{-2}$ Hz) were observed. Possible explanations are: (i) these features are artefacts of large eddies, which are insufficiently sampled in the 12 min to 25 min long averaging intervals (Marandino *et al.*, 2007); (ii) a passing front which violates the assumed stationarity, or (iii) manoeuvring of the ship can create turbulences and recirculation at the measurement location that are not sufficiently removed by the motion correction (see Edson *et al.*, 1998). It will be shown in

Chapter 4 that an incorrect estimation of the stream line coordinate system can reflect large signals into the low frequency part of the spectra.

The common practice to reject flux estimates if the co-spectra exhibit large structures in the low frequency range (e.g. *Marandino et al.*, 2007; *Bell et al.*, 2013), was adopted. The exact cut-off criteria vary from experiment to experiment.

If closed-path analysers are used to sample air, high frequency fluctuations can be attenuated and, therefore, flux information can be lost (*Lenschow and Raupach*, 1991). Here the empirical ogive correction method which was also employed by *Marandino et al.* (2007); *Miller et al.* (2010), is used to estimate the loss in the CO₂ and H₂O flux signals. Under typical measurement conditions ($z \approx 10$ masl, $U \leq 20$ m s⁻¹), a measurement frequency of 20 Hz allows the resolution of eddies up to $f = 5$ (compare with Fig. 2.1). Therefore, the open-path measurement of C_{wT} is assumed to be un-attenuated and can be used to estimated high frequency attenuations in the CO₂ and H₂O co-spectra. This is based on MOST i.e. the covariance-spectra of all scalars are of similar shape.

The flux loss in C_{wx_c} and C_{wx_v} was estimated by comparing the ogive, which is defined as the cumulative sum (integral) of the co-spectra

$$Og_{wx}(n_m) = \left(\sum_{j=0}^m C_{wx}(n_j) \Delta n_j \right), \quad (3.16)$$

with the ogive of C_{wT} . Figure 3.8 shows the normalised ogives of the measured temperature, CO₂, and water vapour flux, which were calculated from the co-spectra shown in Fig. 3.7. The frequency $n_{50\%}$, where the normalised ogive of the temperature flux reaches 50% of the total flux value is indicated and compared with the flux fractions reached by C_{wx_c} and C_{wx_v} at this

frequency.

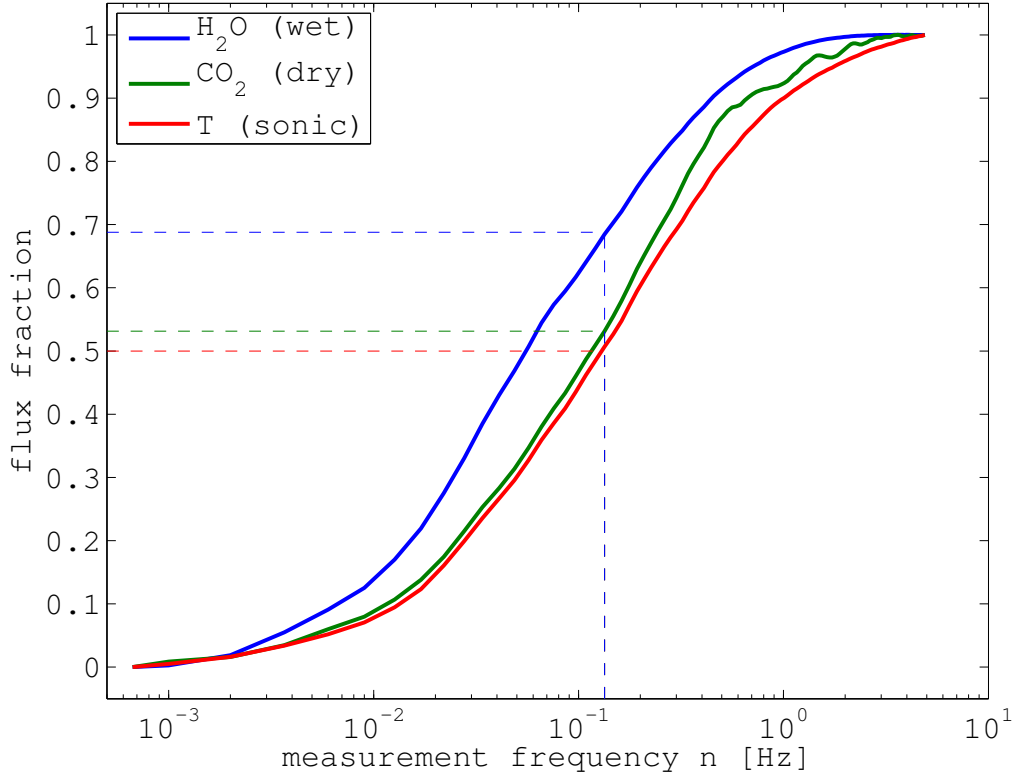


Figure 3.8: Normalized ogive of the sonic temperature (red), water vapour (blue), and CO₂ (green) co-spectra, which are shown in Fig. 3.7. The frequency $n_{50\%}$, where the normalised ogive of the temperature flux reaches 50% and the observed flux fractions of CO₂ and H₂O at this frequency are indicated with dashed lines.

Assuming that the heat flux is fully resolved, and that the spectra should have similar shapes, the frequency loss correction (or gain) can be calculated from the integral of the co-spectra up to, e.g., $n_{50\%}$:

$$g_{50\%} = \left(\sum_{j=0}^{n_{50\%}} C_{wx}(n_j) \Delta n_j \right) / 0.5. \quad (3.17)$$

For the gain to be estimated correctly it is also necessary that the frequency $n_{X\%}$ is selected so that C_{wx} is not attenuated for frequencies below $n_{X\%}$. This can be found by calculating gains using (3.17) for different frequencies

$n_{X\%}$. The results for this example are summarised in Table 3.2. Here it can be seen that the CO_2 spectrum appears un-attenuated up to $n_{80\%} = 0.5 \text{ Hz}$ and the gain estimated from $n_{50\%}$ is $g_{\text{CO}_2} = 1.06$. For the H_2O spectrum the attenuation starts at lower frequencies, here $n_{20\%} = 0.027 \text{ Hz}$ was used to estimate $g_{\text{H}_2\text{O}} = 1.66$. In order to illustrate the attenuation of the high frequency fluctuations, the spectra from Fig. 3.7 are replotted in Fig. 3.9 with the corrected fluxes being used for the normalisation. The application of the gain factors reconciles the spectra in the low frequencies range. This shows, that the spectra are indeed of similar shape (at least in the low frequency domain) and that the attenuation of C_{wxv} starts approximately at $n = 0.03 \text{ Hz}$, while C_{wx_c} is un-attenuated up to approximately 0.5 Hz .

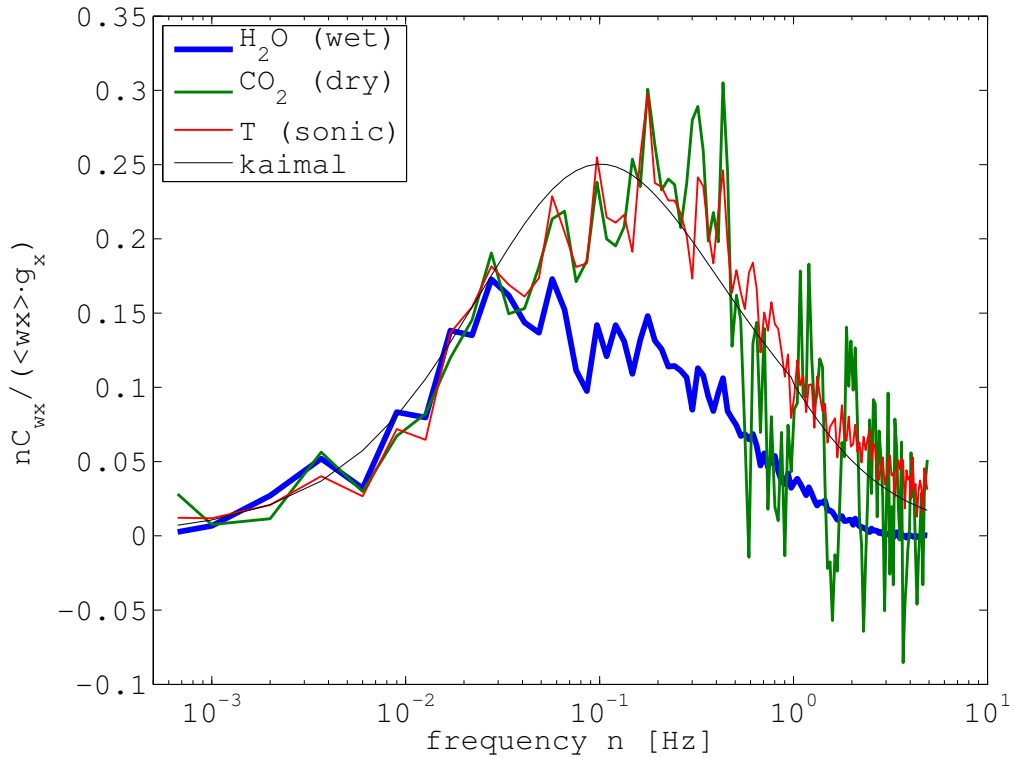


Figure 3.9: Same as in Fig. 3.7, but with gains applied to the normalisation of the CO_2 and water vapour co-spectra.

Table 3.2: Probing frequencies and estimated gain factors for the CO₂ and H₂O co-spectra examples (see Fig. 3.8).

	$n_{20\%}$	$n_{30\%}$	$n_{40\%}$	$n_{50\%}$	$n_{60\%}$	$n_{70\%}$	$n_{80\%}$
n [10^{-2} Hz]	2.7	4.8	8.6	13.4	19.3	32.1	50.8
g_{CO_2}	1.08	1.05	1.08	1.06	1.05	1.09	1.09
$g_{\text{H}_2\text{O}}$	1.66	1.57	1.50	1.38	1.27	1.21	1.15

3.2.8 Calculation of Gas Transfer Velocity

The gas transfer velocity of CO₂ was calculated from the direct CO₂ flux measurements and the air-sea partial pressure gradient $\Delta p\text{CO}_2$ [mol mol^{-1}] using the following formula:

$$k = n_a \langle w'x'_c \rangle (K_{0\text{CO}_2} \Delta p\text{CO}_2)^{-1} \quad (3.18)$$

where $K_{0\text{CO}_2}$ [$\text{mol m}^{-3} \text{atm}^{-1}$] is the solubility of CO₂ in sea water that was calculated following *Weiss* (1974) as a function of the sea surface temperature and the sea surface salinity. The transfer velocities were normalised to a common Schmidt number of 660 using (2.43).

4 Development of a New Motion and Flow Distortion Correction Algorithm

Preface

This chapter is an adopted version of a paper currently under review:

Landwehr, S., N. O'Sullivan, and B. Ward,(2014). Direct Flux Measurements from Mobile Platforms at Sea: Motion and Air Flow Distortion Corrections Revisited. *J. Atmos. Oceanic. Technol.*, submitted.

The right to share and adapt this work is freely available under the Creative Commons Attribution 3.0 License. The data analysis, the interpretation and synthesis of results, the production of figures and the writing were done exclusively by the author of this thesis. Dr. Ward contributed by supervising, assisting and reviewing the work and by providing the infrastructure (ship time, computer time, travel costs, etc.) required to carry out this research project. Mr. O'Sullivan provided ideas and discussions about air flow distortion.

4.1 Introduction

Wind speed plays an important role in all air-sea exchange processes. However, accurate measurement of the in-situ wind speed over the ocean are complicated by the fact that the large structures of ships and the meteorological instrumentation itself obstruct the air flow and thus lead to distortions in the wind field. Even at well exposed measurement positions, this can lead to errors in the wind speed by about 10% (e.g. *Yelland et al.*, 2002; *Popinet et al.*, 2004). Acceleration of the air flow was found to be mainly a function of the measurement location and the relative wind direction (*Popinet et al.*, 2004), with some evidence for a dependence on the relative wind speed (*O'Sullivan et al.*, 2013).

In addition to the acceleration, the relative wind vector is tilted and displaced when the stream lines circumvent the obstacle (*Yelland et al.*, 1998). The tilt of the wind vector is especially relevant for direct flux measurements (*Wilczak et al.*, 2001; *Griessbaum and Schmidt*, 2009). Knowledge of the displacement Δz is required for the correct normalization of the wind speed, measured at height z , to the standard height of 10 m above sea level (masl) and neutral stability. The displacement is even more important for the estimation of the momentum flux using the Inertial Dissipation Method (IDM), where the third power of the estimate of the friction velocity u_* is proportional to the effective measurement height $\tilde{z} = z - \Delta z$ (*Yelland*, 1996).

Direct flux measurements on moving platforms require accurate quantification and correction for the effects of platform motion and distortion of the air flow.

The vertical fluxes of a quantity x can be directly measured as the covariance with the vertical component (w) of the wind speed $\mathbf{u} = (u, v, w)$ in the mean stream line coordinate system:

$$F_x = \langle wx \rangle \quad (4.1)$$

The eddy covariance (EC) method exploits (4.1) to measure the vertical flux of momentum, heat and trace gases, e.g., the friction velocity u_* is defined as*:

$$u_* = \left(\langle uw \rangle^2 + \langle vw \rangle^2 \right)^{1/4} \quad (4.2)$$

Before (4.1) can be applied, the coordinate system needs to be rotated into the local mean stream line coordinate system. This is typically achieved by a double rotation (DR) that aligns the coordinate system with the mean flow by rotating it first in the horizontal plane $x - y$ to achieve $\langle v \rangle = 0$ and then in the new $x' - z'$ plane to obtain $\langle w \rangle = 0$, for a given averaging interval of typically 10 to 30 minutes.

The DR method leaves one remaining degree of freedom, the orientation in the resulting $y'' - z''$ plane. *McMillen* (1988) suggested that the angle about which the coordinate system needs to be rolled around the new x'' can be defined by requiring $\langle vw \rangle = 0$. This results in a triple rotation (TR), where the coordinate system is first yawed, then pitched and finally rolled. The underlying assumption for the TR method is that the cross-wind surface stress is zero. This might not always be valid over the open ocean when wind and swell direction are not aligned. Further more sampling errors in

It is often assumed that the cross-wind stress can be neglected ($\langle vw \rangle = 0$). This leads to the also common definition $u_ = \sqrt{-\langle uw \rangle}$.

the 10 to 30 minute measurements of $\langle vw \rangle$ can lead to erratic corrections with the TR method (*Wilczak et al.*, 2001).

Wilczak et al. (2001) found that the limited averaging time and small measurement errors in the three wind speed components can lead to large errors in the tilt corrections using the DR or TR method and proposed an alternative method, ‘Planar Fit’ (PF), to derive pitch and roll angles of the wind vector which force $\overline{\langle w \rangle} = 0$ for a large ensemble average (indicated by the overbar). Each sample interval then requires only a single rotation (SR) in the new $x' - y'$ plane to force $\langle v \rangle = 0$.

It has to be stressed here that the fluxes determined from (4.1) are highly sensitive to the correct choice of the coordinate system (*Deacon*, 1969), i.e., the tilt of the air flow due to large structures needs to be accounted for. For small tilt errors, the fractional bias in the turbulence fluxes is proportional to the tilt and can vary with stability and boundary layer depth that define the ratios of u_* and $\langle u^2 \rangle$, $\langle v^2 \rangle$, or $\langle w^2 \rangle$ (*Wilczak et al.*, 2001).

Wynngaard (1981) showed that the effect of small nearby structures (e.g. the turbulence probe itself) are not sufficiently corrected by the tilt corrections and presented a set of equations to correct flow distortion in the turbulence quantities arising from objects of size ($a \leq 10 \cdot z$). Modern sensor design and calibration tries to minimize the distortion effects of the turbulence probe itself. The corrections, which were proposed by *Wynngaard* (1981), have been applied by *Oost et al.* (1994) and *Edson et al.* (1991) to correct momentum flux measurements for the effect of a horizontal mounting pole nearby a 3D sonic anemometer. This involved measurements of the tilt of the wind vector made with the sonic anemometer in two different positions (upright and pointing down wards). *Oost et al.* (1994) and *Edson et al.* (1991) showed that applying the *Wynngaard* (1981) correction reconciled the u_* values from

the up and down measurements.

Oost et al. (1994) expanded the approach of *Wyngaard* (1981) to multiple objects but reported also that the corrections would over-estimate the air-flow distortion by objects that are, in size, comparable to the measurement height, i.e. the measurement platform. We are not aware that the corrections proposed by *Wyngaard* (1981) and *Oost et al.* (1994) have found wider application in other open ocean flux measurements. There appears to be general consensus in the meteorological community to minimize turbulent flow distortion by identifying optimal sensor locations, rather than applying empirical corrections to a complex problem. Thus generally only mean wind speed and tilt corrections are applied to the measurements.

On moving platforms the wind speed measurements are additionally biased by the changing sensor orientation (pitch and roll of the platform) and the relative velocity at the probe location. *Anctil et al.* (1993) reported direct flux measurements from a discus buoy and presented an equation for the true motion corrected wind speed using fast measurements of the tilt and acceleration of the platform. This approach was expanded to ships under way by *Edson et al.* (1998), who also presented methods to calculate the tilt angles using the angular rate and acceleration measurements from a strapped-down motion sensor. An addition to *Edson et al.* (1998) was made by *Miller et al.* (2008) to explicitly account for misalignments between the anemometer and the motion sensor. The true wind speed in the earth reference frame is computed as the sum:

$$\mathbf{u}_{\text{true,e}} = \mathbf{u}_{\text{me}} + \mathbf{v}_{\text{ship}} \tag{4.3}$$

where ($\mathbf{u}_{\text{me}} = \mathbf{T}_{ep} \mathbf{u}_{\text{m}}$) is the measured wind speed rotated from the platform

coordinate system (denoted by subscript p) into the earth reference system (denoted by e) and \mathbf{v}_{ship} is the platform motion contamination (for the explicit formulas of \mathbf{v}_{ship} and \mathbf{T}_{ep} see *Edson et al. (1998)* and *Miller et al. (2008)*). In order to rotate the wind vector into the local stream line coordinate system for the computation of fluxes, *Anctil et al. (1993)* applied a double rotation to $\mathbf{u}_{\text{true},e}$:

$$\mathbf{u} = \mathbf{DR}(\mathbf{u}_{\text{me}} + \mathbf{v}_{\text{ship}}) \quad (4.4)$$

Note that *Anctil et al. (1993)* applied (4.4) to EC measurements from a moored buoy, hence $\langle v_{\text{ship}} \rangle = 0$. Equation (4.4) has become the baseline for all direct flux measurements from mobile platforms including ships under way.

Edson et al. (1998) compared momentum flux measurements on-board two different research vessels, the *Iselin* and the *Wecoma*, with simultaneous measurements on (a) the research platform *FLIP* and (b) a small autonomous catamaran. In both cases the along-wind stress component ($-\langle uw \rangle$) measured on-board the ships was approximately 15% higher than the measurements from either *FLIP* or the catamaran. The difference was attributed to air-flow distortion biases in the ship's eddy covariance (EC) measurements, with the assumption that the measurements taken on R/P *FLIP* and the catamaran were free from air-flow distortion (*Edson et al., 1998*). For R/V *Iselin*, *Edson et al. (1998)* reported tilts in the true wind vector of approximately 3° to 5° for bow-on and beam-on wind directions, respectively.

Pedrerros et al. (2003) supported these results reporting that $-\langle uw \rangle$ measured on-board the R/V *L'Atalante* was on average 18% higher than

direct flux measurements made from an ASIS buoy, for a maximum distance of 5 km. However, this number is based on a linear regression to the direct flux measurements from the ship and from the ASIS buoy, which had a relatively large intercept (see Fig. 7a in *Pedrerros et al. (2003)*). Assuming no intercept, the average over-estimation becomes approximately 30%. *Pedrerros et al. (2003)* also reported a 30% systematic over-estimation of the neutral drag coefficient ($C_{D10N} = -\langle uw \rangle u_{10N}^{-2}$) by the ship's EC measurements, when compared to the EC measurements from the ASIS buoy and ship-borne IDM estimates (see Fig. 11 in *Pedrerros et al. (2003)*). This include all measurements made during the experiment. *Pedrerros et al. (2003)* argued that the difference between the direct measurement on the ship and the buoy might be caused by different fetches encountered by the ASIS buoy and the ship during the course of the experiment. However, the IDM results for C_{D10N} from the ship agree with the measurement of C_{D10N} from the buoy (see Fig. 11 in *Pedrerros et al. (2003)*). I therefore assume that the over-estimation of $-\langle uw \rangle$ by the EC measurements on-board the R/V *L'Atalante* was on average +30% and was due to flow distortion on the ship. *Pedrerros et al. (2003)* also reported an over-estimation of the sensible heat flux $\langle uT \rangle$ by $9(\pm 9)\%$ when compared to direct measurements from the ASIS buoy.

Pedrerros et al. (2003) restricted the dataset to relative wind directions less than $\pm 30^\circ$ and $\langle u_{me} \rangle \langle v_{ship} \rangle^{-1} \geq 2$ and corrected the measured wind speeds for mean air-flow distortion. The corrections for acceleration, relative wind direction, and tilt are reported in *Dupuis et al. (2003)*: the average vertical tilt of the wind vector was 7° and decreased slightly with increasing relative wind direction. The direct fluxes were calculated using (4.4) and no attempt was made for a flow distortion correction on the fluxes.

The apparent bias in the direct flux measurements motivated *Edson et al.*

(2013) to exclude ship-borne EC momentum flux measurements from the recent update to the COARE bulk flux algorithm (version 3.5). However, earlier versions of COARE (*Fairall et al.*, 2000, 2003) did include ship-borne EC momentum flux measurements. For $u_{10N} = 5 \text{ m s}^{-1}$ the bulk u_* values from COARE 3.0 are 10% higher than for newest version COARE 3.5 and for $u_{10N} = 10 \text{ m s}^{-1}$ COARE 3.0 predicts 2.5% higher u_* values than COARE 3.5. The ratio decreases approximately linear over the wind speed range $u_{10N} = 5 - 10 \text{ m s}^{-1}$. Direct EC flux measurements of trace gases from buoys are rare, mainly due to the usually higher power and maintenance requirements and therefore ship-borne flux measurements are still the main input to bulk flux formulations for gas exchange (*Fairall et al.*, 2011).

Here mean wind speed and direct flux measurement taken on board the R/V *Saramiento de Gamboa* during the MIDAS-SPURS field campaign in March/April 2013 are analysed and compared to the mean wind speed measurements and bulk flux estimates from a moored buoy. The wind speed and direction measurements from the buoy are used to estimate a mean flow distortion correction for the wind speed measurements taken on the bow mast of the research vessel. The wind vector tilts are estimated using an adaptation of the planar fit method and are used in a new way to correct the wind speed measurements for ship-motion and air-flow distortion, prior to the direct flux calculations.

The new approach to air-flow distortion and motion correction is presented in section 4.2, followed by the description of the experiment and the methods used to correct the mean wind speeds for acceleration and tilt of the streamlines (section 4.3). The results obtained using the classic approach (4.4) and our new method are compared in section 4.4. The conclusions are provided in section 4.5.

4.2 Theory

4.2.1 Parameterisation of the Wind Vector Distortion

Before the measured 3D wind speed can be used to calculate mean wind speed and direct fluxes it has to be corrected for air-flow distortion and ship motion. The effect of air-flow distortion on the mean wind speed measurement can be described with a flow distortion transformation matrix.

$$\mathbf{A}(\alpha) = a(\alpha)\boldsymbol{\Psi}(\alpha)\boldsymbol{\Theta}(\alpha)\boldsymbol{\Phi}(\alpha) \quad (4.5)$$

where a is the acceleration of the wind speed, α is the relative wind direction, and $\boldsymbol{\Psi}, \boldsymbol{\Theta}, \boldsymbol{\Phi}$ are the rotations of the wind vector by the Euler angles ψ, θ, ϕ . Although the relative wind direction fluctuates over time, one can assume that when the variations of α are small, the effect of flow distortion can be approximated by $\mathbf{A}(\langle\alpha\rangle)$. This means that \mathbf{A} becomes essentially a function of the relative horizontal wind direction, as the average undisturbed vertical wind speed is close to zero over the open ocean. Increased motion (heave, pitching, rolling or yawing) of the platform can potentially create large deviations from the expected mean flow distortion.

The relation between the measured 3D wind speed average and the average of the true wind vector can now be described with the following equation:

$$\langle\mathbf{u}_{me}\rangle = \mathbf{A}(\alpha)(\langle\mathbf{u}_{true,e} - \mathbf{v}_{ship}\rangle) \quad (4.6)$$

It is important to note that it is the relative wind vector $\langle\mathbf{u}_{true,e} - \mathbf{v}_{ship}\rangle$ and not $\langle\mathbf{u}_{true,e}\rangle$ which is transformed by \mathbf{A} .

4.2.2 Height displacement of the air flow

There are several reports of significant height displacements of the air flow by several meters and the wind speed measured at height z might originate from $\tilde{z} = z - \Delta z$. *Yelland et al.* (2002) found that the magnitude of the displacement varies with the relative wind direction and that variations with the relative wind speed could be neglected. In order to make wind speed measurements comparable, they need to be normalized to a height of 10 masl and neutral stability. Therefore it is necessary to know the original height of the measured wind speed. Assuming a universal logarithmic profile one can express the wind speed at height \tilde{z} as:

$$\begin{aligned} u(\tilde{z}) &= u(z) - \frac{u_*}{\kappa} \left[\ln\left(\frac{z}{\tilde{z}}\right) - \psi_u\left(\frac{z}{L_*}\right) + \psi_u\left(\frac{\tilde{z}}{L_*}\right) \right] \\ &= u(z) \left[1 + u(z)^{-1} \cdot f(z, \tilde{z}, L_*) \right] \end{aligned} \quad (4.7)$$

In (4.7) the correction function was defined as:

$$f(z, \tilde{z}, L_*) = -\frac{u_*}{\kappa} \left[\ln\left(\frac{z}{\tilde{z}}\right) - \psi_u\left(\frac{z}{L_*}\right) + \psi_u\left(\frac{\tilde{z}}{L_*}\right) \right] \quad (4.8)$$

For neutral stability (i.e. $L_* \rightarrow \infty$) and typical $z = \mathcal{O}(10 \text{ m})$ it can be estimated that $|f(z, \tilde{z}, \infty)| \approx |u_* \cdot \kappa^{-1} \cdot \ln(z \tilde{z}^{-1})| \ll u(z)$. For unstable conditions ($\frac{z}{L_*} \rightarrow -\infty$): $u(z)^{-1} \cdot f(z, \tilde{z}, L_*) \rightarrow 0$. However, for stable conditions $\left[-\psi_u\left(\frac{z}{L_*}\right) + \psi_u\left(\frac{\tilde{z}}{L_*}\right)\right]$ has the same sign as $\ln(z \tilde{z}^{-1})$ and $[u(z)^{-1} \cdot f(z, \tilde{z}, L_*)]$ can potentially become the order of 1.

For a ship under way, the measured wind speed at height z is given by:

$$\begin{aligned}
 u_{\text{me}}(z) &= a(\alpha) |\mathbf{u}(\tilde{z}) - \mathbf{v}_{\text{ship}}| \\
 &= a(\alpha) |\mathbf{u}(z) \cdot \{1 + u(z)^{-1} f(z, \tilde{z}, L_*)\} - \mathbf{v}_{\text{ship}}| \\
 &= a(\alpha) \left[u^2 - 2(\mathbf{u} \cdot \mathbf{v}_{\text{ship}}) + v_{\text{ship}}^2 + f^2 + \frac{2f}{u} (u^2 - \mathbf{u} \cdot \mathbf{v}_{\text{ship}}) \right]^{1/2} \\
 &= a(\alpha) \left[|\mathbf{u} - \mathbf{v}_{\text{ship}}|^2 \cdot \left(\frac{f^2}{u^2} \cdot c_2(\mathbf{u}, \mathbf{v}_{\text{ship}}) + \frac{2f}{u} \cdot c_1(\mathbf{u}, \mathbf{v}_{\text{ship}}) \right) \right]^{1/2} \\
 &\approx a(\alpha) |\mathbf{u} - \mathbf{v}_{\text{ship}}| \left\{ 1 + c_1(\mathbf{u}, \mathbf{v}_{\text{ship}}) \frac{f}{u} \right. \\
 &\quad \left. + [c_2(\mathbf{u}, \mathbf{v}_{\text{ship}}) - c_1(\mathbf{u}, \mathbf{v}_{\text{ship}})^2] \frac{f^2}{2u^2} \right\} \tag{4.9}
 \end{aligned}$$

Here the notation was simplified using $u \equiv u(z)$ and $f \equiv f(z, \tilde{z}, L_*)$ and the ratios:

$$c_1(\mathbf{u}, \mathbf{v}_{\text{ship}}) \equiv \frac{u^2 - u \cdot v_{\text{ship}} \cdot \cos(\alpha_{\text{true}})}{|\mathbf{u} - \mathbf{v}_{\text{ship}}|^2} \tag{4.10}$$

$$c_2(\mathbf{u}, \mathbf{v}_{\text{ship}}) \equiv \frac{u^2}{|\mathbf{u} - \mathbf{v}_{\text{ship}}|^2} \tag{4.11}$$

were defined, which depend on the true wind speed, the ship velocity, and the true relative wind direction α_{true} , which is given as the difference between the true wind direction and the ships heading:

$$\alpha_{\text{true}} \equiv \arccos \left(\frac{(-\mathbf{u}) \cdot \mathbf{v}_{\text{ship}}}{u \cdot v_{\text{ship}}} \right) \tag{4.12}$$

This gives $\alpha_{\text{true}} = 0^\circ$ for bow-on winds and $\alpha_{\text{true}} \pm 180^\circ$ for winds from the stern. The measured relative wind direction α is defined analogues to (4.12) with \mathbf{u}_{me} replacing \mathbf{u} . Both $|c_1|$ and $|c_2|$ are ≤ 1 for $|\alpha_{\text{true}}| \leq 90^\circ$. For the last step in (4.9) the approximation $\sqrt{1+x} \approx 1 + 0.5x - 0.25x^2$ was used.

The flow distorted wind speed measurements at two different heights z_1

and z_2 can be related to each other by expressing $u(\tilde{z}_1)$ and $u(\tilde{z}_2)$ based on the wind speed at height z :

$$\frac{u_{\text{me}}(z_1)}{u_{\text{me}}(z_2)} \approx \frac{a_1(\alpha)}{a_2(\alpha)} \{1 + x_a\} \quad (4.13)$$

with $x_a \equiv c_1(u(z), v_{\text{ship}}, \alpha_{\text{true}}) \cdot \frac{f(\tilde{z}_1, \tilde{z}_2, L_*)}{u(z)}$

where $1/(1+x) \approx 1-x$ was used, and the terms involving $(f(z, \tilde{z}, L_*) \cdot u(z)^{-1})^2$ and higher were omitted.

Equations (4.9) and (4.13) show that for the estimation of the wind speed acceleration $a(\alpha)$, the ship speed and atmospheric stability need to be taken into account. Further, an estimate of the height displacement Δz is required to normalize the flow distortion and ship motion-corrected true wind speed (relative to the surface current \mathbf{u}_{sc}) for height and stability.

$$u_{10\text{N}} = |\mathbf{A}(\alpha)^{-1} \mathbf{u}_{\text{me}}(z) + \mathbf{v}_{\text{ship}} - \mathbf{u}_{\text{sc}}| - \frac{u^*}{\kappa} \left[\ln\left(\frac{\tilde{z}}{10}\right) - \psi_u\left(\frac{\tilde{z}}{L_*}\right) \right] \quad (4.14)$$

If the height displacement is unknown (4.9) and (4.13) can be used to estimate the uncertainty arising from a potential Δz .

4.2.3 Motion Correction and Rotation into the mean flow

I found that rotating the wind vector after the motion correction (i.e. using (4.4)) leads to an over-estimation of the wind vector tilt and can cause potentially large errors in the computed fluxes if the ship's mean velocity is not zero.

I suggest here that the tilt of the wind vector, which is mainly caused by air-flow distortion, needs to be removed before the wind vector is corrected for the mean ship velocity. The derived true wind vector should only be

rotated within the horizontal plane.

I observed that applying the rotations $\Phi(\alpha)$, $\Theta(\alpha)$ and $\Psi(\alpha)$ before correcting the measured wind vector for pitch, roll, yaw and heave of the ship leads to a less efficient removal of the platform motion signal from the co- and power spectra. Our interpretation is that the velocity signal caused by this fast platform motion is imprinted on the measurements of the already distorted wind vector and therefore needs to be removed before rotating the wind vector. Our modified version of (4.4) becomes:

$$\mathbf{u} = \mathbf{SR} \left(\mathbf{A}'(\alpha)^{-1}(\mathbf{u}_{\text{me}} + \mathbf{v}'_{\text{ship}}) + \langle \mathbf{v}_{\text{ship}} \rangle \right) \quad (4.15)$$

where the ship motion is separated into the mean horizontal velocity $\langle \mathbf{v}_{\text{ship}} \rangle$ and the fluctuating part $\mathbf{v}'_{\text{ship}}$ (pitch, roll, yaw and heave) with $\langle \mathbf{v}'_{\text{ship}} \rangle = 0$.

The transformation \mathbf{A}' denotes a modification to (4.5): the relative wind vector is not divided by $a(\alpha)$, but $[(1 - a(\alpha)^{-1}) \cdot \langle \mathbf{u}_{\text{me}} \rangle]$ is subtracted. Thus (4.5) becomes

$$\mathbf{A}'^{-1}\mathbf{x} \equiv \Psi^{-1}\Theta^{-1}\Phi^{-1}\mathbf{x} - \langle \Psi^{-1}\Theta^{-1}\Phi^{-1}\mathbf{x}(1 - a^{-1}) \rangle \quad (4.16)$$

Note that if transformation \mathbf{A} were used in (4.15), the covariance moment $\langle uw \rangle$ would be scaled with the correction for the mean wind speed acceleration $(a^{-2})^\dagger$. There is, however, no evidence in literature nor in our results that the acceleration of the mean wind speed reflects equally on the turbulent quantities. Also note that after the motion and tilt correction in (4.15), only a single rotation over the z-axis is applied to the true wind vector in order to align it with the local stream line (thereby forcing $\langle v \rangle = 0$).

[†]This follows from the distributivity of the multiplication with a scalar over the addition
 $a \cdot (x + y) = a \cdot x + a \cdot y$

If the flow distortion correction \mathbf{A}'^{-1} is not available, e.g., if there is not enough data from one wind direction sector to perform a planar fit, the wind speed measurements should be corrected in the following way:

$$\mathbf{u} = \mathbf{SR} \left(\mathbf{SR}^{-1} \mathbf{DR} (\mathbf{u}_{\text{me}} + \mathbf{v}'_{\text{ship}}) + \langle \mathbf{v}_{\text{ship}} \rangle \right) \quad (4.17)$$

Equation (4.15) describes: (i) rotation of the measured wind speeds into earth frame and correction for $\mathbf{v}'_{\text{ship}}$; (ii) double rotation to achieve first $\langle v \rangle = 0$ and then $\langle w \rangle = 0$; (iii) reversal of the rotation around the z-axis, indicated by \mathbf{SR}^{-1} ; (iv) correction for $\langle \mathbf{v}_{\text{ship}} \rangle$; (v) a final rotation around the z-axis to achieve $\langle v \rangle = 0$.

For on-station measurements, equation (4.17) is equivalent to (4.4), but avoids the over-estimation of the wind vector tilt if the mean platform velocity is > 0 . Unlike (4.15), equation (4.17) cannot account for potential roll or yaw of the relative wind vector and can therefore lead to biased flux estimates. The flow distortion-induced yaw of the wind vector becomes relevant only when the platform is moving and the vector addition of \mathbf{v}_{ship} and \mathbf{u}_{me} leads to an incorrect estimate of the true wind direction. This bias in α_{true} has no effect on the scalar fluxes or u_* (if defined as in (4.2)). It does however lead to incorrect estimates of the wind stress angle

$$\alpha_\tau = \text{atan} \left(\frac{\langle vw \rangle}{\langle uw \rangle} \right). \quad (4.18)$$

The roll and pitch of the wind vector are relevant for all fluxes. Further, the planar fit reduces the effect of calibration errors and the under-sampling of large eddies, as discussed by *Wilczak et al.* (2001). Therefore, (4.15) is superior to (4.17), even if mean acceleration a and yaw bias ψ are unknown, and should be applied when possible.

4.3 Methods

The measurements presented here were taken on-board the R/V *Saramiento de Gamboa* during the SPURS-MIDAS cruise (Las Palmas de Gran Canaria 16th March – Ponta Delgada, Azores 17th April, 2013). Relative wind speed and direction were measured on the bow mast of the ship at two different heights $z_1 = 10$ masl and $z_2 = 15$ masl with a *R3A* 3D sonic anemometer (Gill) and a 2D vane anemometer *Wind Monitor-MA* (Young), respectively. Fig. 4.1 shows a photograph of the bow of the ship, on which the positions of the two anemometers are indicated. Note that the 3D sonic was located approximately 1.5 m in front of a large tower with a cross section of 0.75 m. An inertial motion unit *NAV440* (Moog-Xbow) recorded 3D acceleration and angular rates. The unit was installed 1.16 m behind and 0.82 m below the *R3A*. This position vector was accounted for in the motion correction following *Edson et al.* (1998). A differential GPS system *VS-100* (Hemisphere GPS) recorded the ship’s heading and course and provided a universal time stamp. Mean meteorological data (downwelling long- and shortwave, air temperature, relative humidity, atmospheric pressure and the relative wind speed at z_2) were recorded at 0.1 Hz and averaged to 12min. The wind speed (u_m, v_m, w_m), speed of sound temperature (T_{sonic}), and ship motion were recorded at a frequency of 20 Hz. They were used to calculate true wind speed and the covariance moments. The details of the motion correction procedures are described in section (4.3.4). The direct comparison of the ship’s heading and the heading recorded by the *VS-100* revealed a yaw of 5° in the orientation of the flux mast in respect to the center-line of the ship. All measurements were corrected for this tilt offset prior to further analysis.

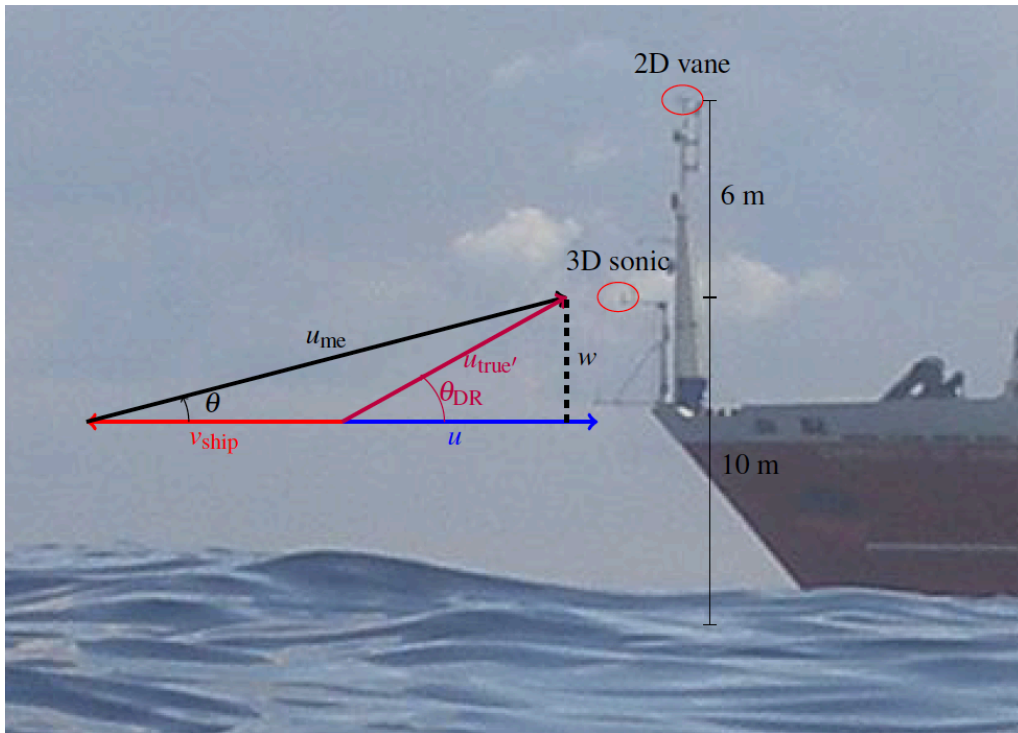


Figure 4.1: Photograph of the bow of the R/V *Saramiento de Gamboa* with indications of the positions of the 3D sonic and the 2D vane anemometers. Also shown is an illustration of the over-estimation of the pitch of the relative wind vector by the classic motion-tilt correction (4.4). The relative wind vector $\mathbf{u} - \mathbf{v}_{ship}$ is tilted by the angle θ due to the presence of the ship and measured as \mathbf{u}_{me} with vertical component w . Applying the double rotation after the correction for \mathbf{v}_{ship} gives θ_{DR} which overestimates the tilt.

A buoy, the WHOI station 41061 [‡], was moored in September 2012 at the measurement site (24.5811°N, 38°W) and provided mean meteorological measurements with 1 minute resolution. EC flux measurements were also performed on the buoy, but the data is not available at the current time. The wind speed and direction measurement from the buoy are used as a free stream reference to estimate the effects of mean air-flow distortion in the ship borne measurements. Figure 4.2 shows a time series of wind speed, direction, and friction velocity measured on-board the ship and by the buoy

[‡]More information about the mooring on station 41061 can be found under http://www.ndbc.noaa.gov/station_page.php?station=41061

(the buoy u_* is computed with the COARE 3.0 bulk flux algorithm). Also shown are the ships speed, the distance to the buoy, and the significant wave height measured on the buoy.

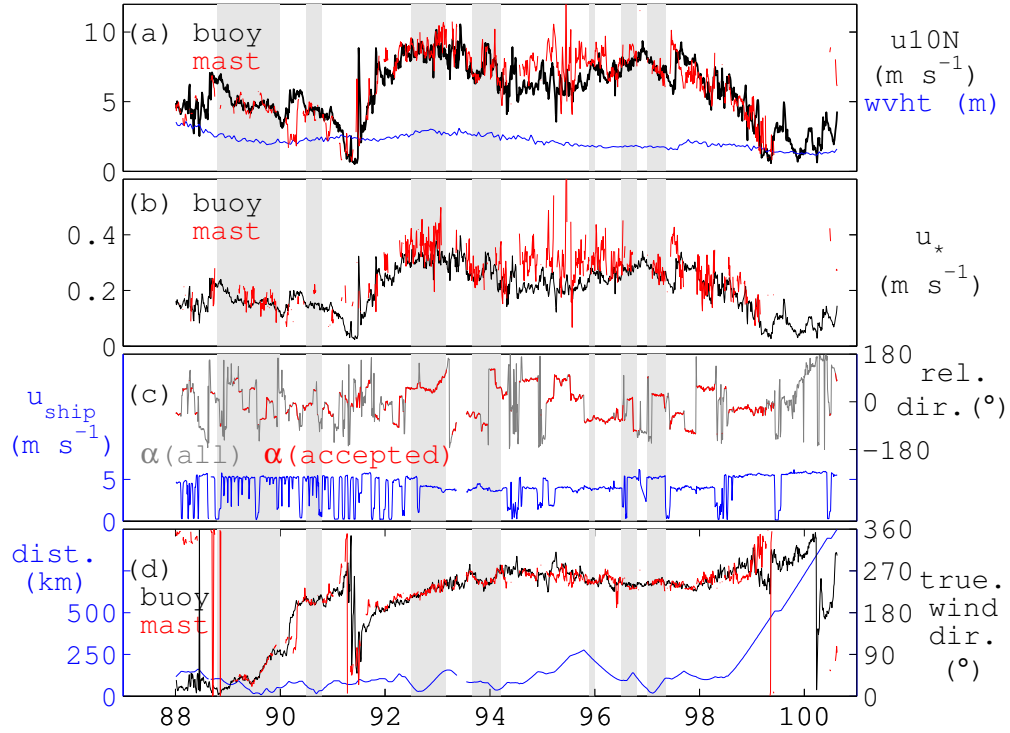


Figure 4.2: Time series of (a) normalized wind speed and significant wave height; (b) friction velocity; (c) measured relative wind direction and ship speed; (d) true wind direction and distance between ship and buoy position. The buoy values are COARE 3.0 bulk flux results calculated from 1 minute measurements on the mooring, which were averaged to 12 minutes and interpolated on the bow mast time series using the GPS time stamps. Bow mast u_{10N} , true wind direction and u_* are calculated using (4.14) and (4.15), respectively. The shaded areas mark periods that were selected for the estimation of the yaw and acceleration bias in the measured relative wind direction and speed on the bow mast. These periods are also used for the comparison of the direct measurements of u_* on the bow mast with the COARE 3.0 estimates from the buoy.

4.3.1 Quality Control

The 12 minute time series of \mathbf{u} was used to calculate average values and the direct fluxes $\langle wu \rangle$, $\langle wv \rangle$ and $\langle wT_{\text{sonic}} \rangle$; the same was done for 4 minute averaging periods.

For mean variables like u_{10N} and $\langle \mathbf{u}_{\text{me}} \rangle$, intervals were rejected when one of the following empirical criteria was fulfilled:

- Measured relative wind direction:

$$|\langle \alpha \rangle_{12min}| \geq 150^\circ.$$

- Variation of the three sub interval wind directions:

$$|\langle \alpha \rangle_{4min,i} - \langle \alpha \rangle_{4min,j}| \geq 20^\circ, \text{ (with } i, j = [1, 2, 3]).$$

- Variation of the ship velocity:

$$\sqrt{\sigma(v_{ship,x})^2 + \sigma(v_{ship,y})^2 + \sigma(v_{ship,z})^2} \geq 1 \text{ m s}^{-1},$$

where $\sigma(v_{ship,x}) = \langle v_{ship,x}(i+1) - v_{ship,x}(i) \rangle$ is the average difference between two consecutive measurements.

- The vector average of the instantaneous course/heading vector was smaller than 0.95 (1 indicates a perfectly stable course).
- Measured average relative wind speed to low:

$$\langle u_{\text{me}} \rangle \leq 2.5 \text{ m s}^{-1}$$

In order to reduce the loss of sample intervals due to maneuvering of the ship, the 12 minute intervals were defined every 4 minutes, thus three intervals were overlapping. If more than one of three contiguous (overlapping) intervals passed the quality control, only the first interval was accepted. Of 1515 independent 12 minute intervals, 964 passed the first quality control.

For the direct fluxes, the following additional rejection criteria were applied:

- Measured relative wind direction:

$$|\langle \alpha \rangle_{12min}| \geq 90^\circ.$$

- Variation of the three sub interval wind directions:

$$|\langle \alpha \rangle_{4min,i} - \langle \alpha \rangle_{4min,j}| \geq 15^\circ.$$

- The cross-correlation $\langle w_{me}(t)v_{ship,z}(t + \Delta t) \rangle$ suggested a shift of $\Delta t > 1$ sample of the time series.

612 intervals passed these additional criteria.

Periods with relatively constant conditions and short distances between the buoy and the ship ($\leq 100\text{km}$) were used for the estimation of the wind speed acceleration and yaw bias, as well as for the comparison of the direct flux measurements with the bulk flux estimates from the buoy. These periods are marked as shaded areas in Fig. 4.2. For these tasks, intervals were additionally rejected when criteria for the ship's mean variables were fulfilled (see above) or on of the following:

- Ship speed minimum: $v_{ship} \leq 3 \text{ m s}^{-1}$.
- Difference between ship's course and heading: $|\text{COG} - \text{HDG}| \geq 10^\circ$.
- Stability (at buoy and ship): $L_* \geq -30 \text{ m}$.

The first two criteria were implemented to reduce the uncertainty in the wind direction measurement. The third criterion accounts for the uncertainty arising from large wind profile corrections for $L_* \approx z$. These controls were passed by a total of 560 12-minute intervals, of which 185 passed the criteria for direct fluxes (see above). Note that for these intervals, the significant wave height was always below 3.1 m and thus below the height of the wind speed is measured at the buoy (3.3 masl).

4.3.2 Estimation of the wind vector pitch and roll

The pitch and roll of the wind vector were estimated from the 3D relative wind speed measurement at the bow mast using a method similar to the anemometer tilt correction algorithm, planar fit (PF), presented by *Wilczak et al.* (2001). The underlying hypothesis is that, over the ocean, the time average of the vertical wind speed component is close to zero. An observed non-zero vertical wind speed can be caused by (a) a tilt of the anemometer (i.e., the platform), (b) a tilt of the wind vector due to flow distortion, or (c) measurement errors.

In this experiment, the anemometer was mounted collinearly with the motion sensor. However, even after accounting for the platform tilt by using the apparent wind speed measurements \mathbf{u}_{me} , the mean vertical wind speed was non-zero and increased with growing relative wind speed. Therefore, it is assumed that the observed non-zero vertical component of the average apparent wind speed is caused by flow distortion.

The method presented here is an adaptation of the PF for the situation where the structure of the wind field cannot be described with a single set of tilt angles. In the case of ship borne measurements the flow distortion pattern will likely vary with the relative wind direction. To account for this, the PF method is applied on wind direction sectors. A sector planar fit was also used by *Yuan et al.* (2010) to account for air flow patterns over forestry. In *Yuan et al.* (2010) the roll and pitch angles are defined in a fixed coordinate frame. Here the pitch and roll angles are defined relative to the average relative wind direction. This has the advantage that (i) a direct comparison with the pitch estimate from the DR method is possible and that (ii) the effect on the EC fluxes can be estimated using small angle

approximations (see *Wilczak et al.*, 2001).

To determine the tilt angles $\phi(\alpha)$ and $\theta(\alpha)$, the apparent wind speed measurements \mathbf{u}_{me} were averaged over 12 minute intervals and sorted into bins based on the average relative wind direction $\tan^{-1}(\langle v_{me} \rangle / \langle u_{me} \rangle)$. From the members of each bin a mean relative wind direction was computed and each individual averaged wind vector was rotated into this ensemble mean flow.

$$\langle \mathbf{u}_{mr} \rangle = \mathbf{R} \langle \mathbf{u}_{me} \rangle \quad (4.19)$$

The wind vector pitch and roll in the stream line coordinate system was then derived from a linear regression to the measured vertical wind speed with the horizontal wind speed components:

$$\langle w_{me} \rangle = c_3 + b_1 \cdot \langle u_{mr} \rangle + b_2 \cdot \langle v_{mr} \rangle \quad (4.20)$$

The mean pitch θ and roll ϕ of the relative wind vector for each sector are given by:

$$\theta = \tan^{-1}(b_1) \quad (4.21)$$

$$\phi = \tan^{-1}(-b_2) \quad (4.22)$$

The result of the regression and the residual c_3 are shown in Fig. 4.3. An asymmetry between port and starboard winds can be seen. This could be caused by a slight misalignment of the bow mast to the ship, which was estimated to 5° . I acknowledge that the definition of a roll angle in a radial coordinate system is questionable, as $\langle v_{mr} \rangle$ will vanish for sufficiently small wind direction bins. However, I found that including ϕ in the analysis

did significantly improve the results when compared to using $\langle w_{me} \rangle = c_3 + b_1 \cdot (\langle u_{me} \rangle^2 + \langle v_{me} \rangle^2)^{0.5}$. In order to distinguish the above described variation of the PF method from others, it will be dubbed radial planer fit method (rPF) henceforth.

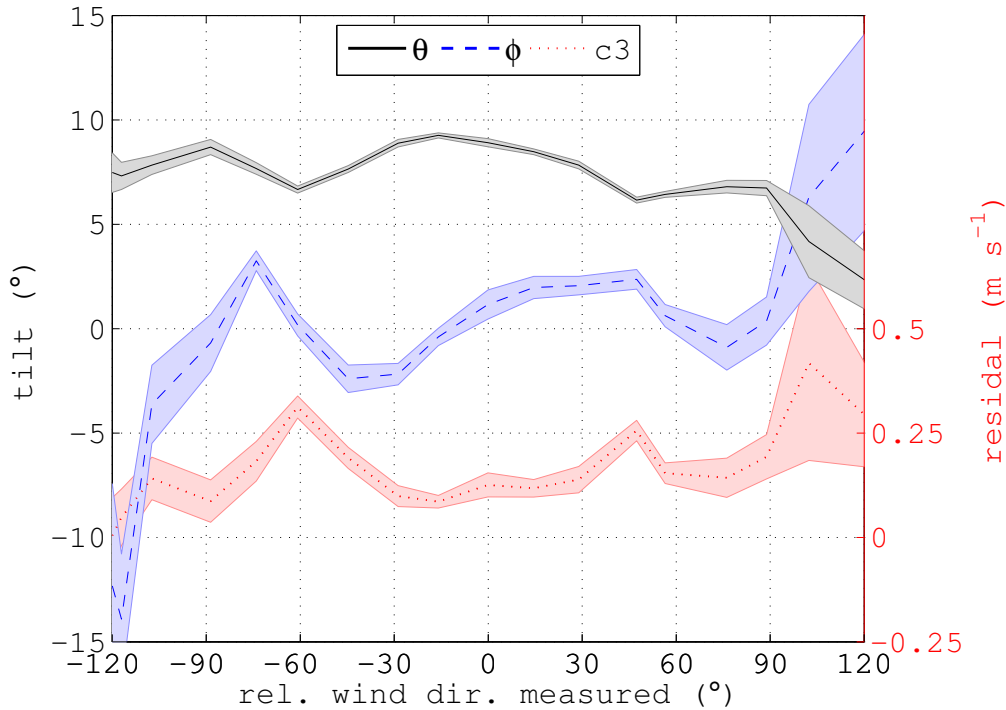


Figure 4.3: Pitch and roll angles (θ and ϕ respectively) and the vertical wind speed residual c_3 , determined by the linear regression (4.20) over 15° wind direction bins, are plotted as functions of the measured relative wind direction. The shading shows the 95% confidence intervals of the regression.

In Fig. 4.4 the pitch angles estimated using (4.4) (θ_{DR}) and (4.17) (θ_{DRx}) are plotted as a functions of the relative wind direction. Also shown are the results from the rPF method (θ_{rPF}), respectively. The pitch estimates from the classical DR method show a strong dependence on the relative wind direction and on the ratio $v_{ship}u_{me}^{-1}$. Highest values of θ_{DR} are reached when the ship steams into the wind. The estimates from the DRx method show much less variability and agree well with the estimates from the rPF

method, however, predicting on average slightly higher pitch values than the rPF method especially at low wind speeds. This is because the DRx method does not account for c_3 .

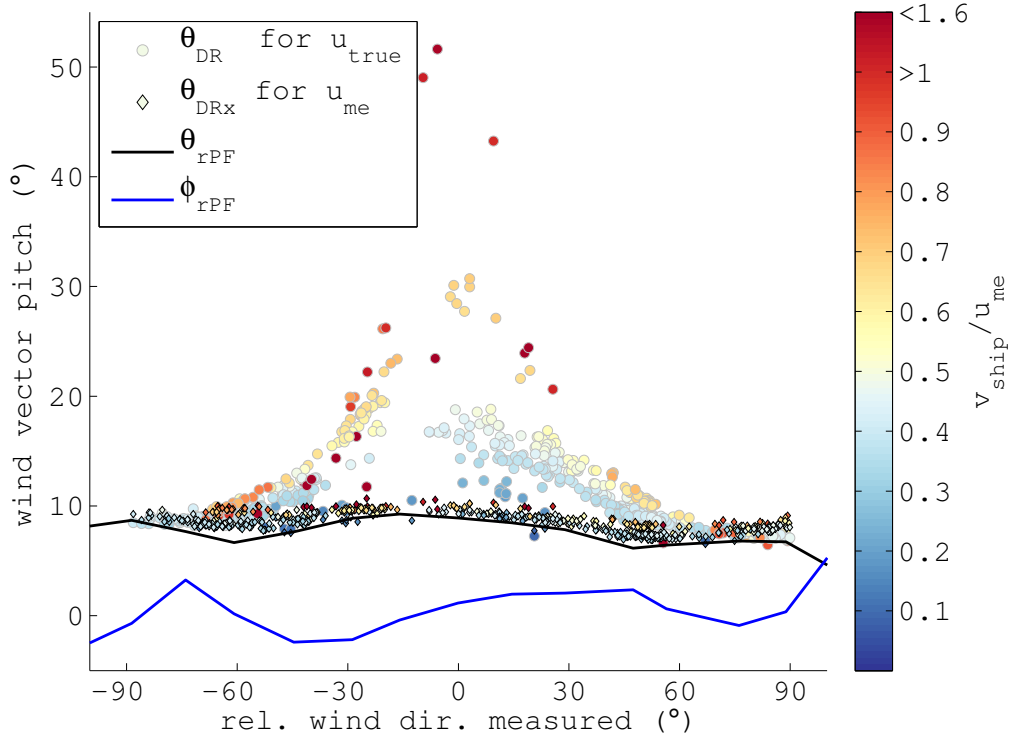


Figure 4.4: Wind vector pitch at the 3D sonic calculated using the classic DR (\circ) and using the alternative method DRx (\diamond) as function of the measured relative wind direction and the ratio of ship velocity and measured wind speed. The results for pitch and roll from the rPF method (see Fig. 4.3) are shown for comparison (black and blue lines).

The apparent over-estimation of the wind vector tilt by the DR correction method is illustrated in Fig. 4.1 for the example of the ship steaming into the wind ($\alpha = 0$). The relative wind speed is pitched upwards by the angle θ , which leads to a measured average vertical velocity $\langle w \rangle > 0$. Deriving the pitch angle from $\langle w \rangle > 0$ and the corrected horizontal wind speed $\langle u_{true} \rangle$ as done in (4.4) gives $\theta_{DR} > \theta$.

4.3.3 Estimation of Yaw Bias and Acceleration

While pitch and roll angle can be estimated directly from the 3D wind speed measurement on-board the ship, the estimation of the yaw angle ψ and the acceleration of the mean wind speed a requires a free stream reference. Here the wind speed and surface current measurements from the moored buoy were utilized.

The wind speed measurements on the mooring were made at a height of 3.3 masl and corrected to a standard height and neutral stability using the bulk flux parameterisation COARE3.0 (Fairall *et al.*, 2003). The u_{10N} values were converted to $u(z)_{\text{freestream}}$ using the local stability at the location of the R/V *Saramiento de Gamboa*, derived from the direct flux measurements and the measurement height of the bow mast sonic $z = 10$ masl. In order to calculate the length scale L_* , use was made of the approximation

$$\langle wT \rangle + 0.61T \langle wq \rangle \approx \langle wT_{\text{sonic}} \rangle = \langle wT \rangle + 0.51T \langle wq \rangle.$$

The free stream wind vector relative to earth at the location of the ship was calculated, assuming the same surface currents as measured by the buoy. The expected relative wind vector was calculated as

$$\langle \mathbf{u}_{\text{exp}} \rangle = (\langle \mathbf{u}(z)_{\text{freestream}} - \mathbf{v}_{\text{ship}} \rangle) \quad (4.23)$$

and used to estimate the acceleration of the relative wind speed and the yaw bias as functions of the measured relative wind direction. Note that the speed of the surface current measured at the buoy location was on average 0.2 m s^{-1} with a maximum value of 0.4 m s^{-1} .

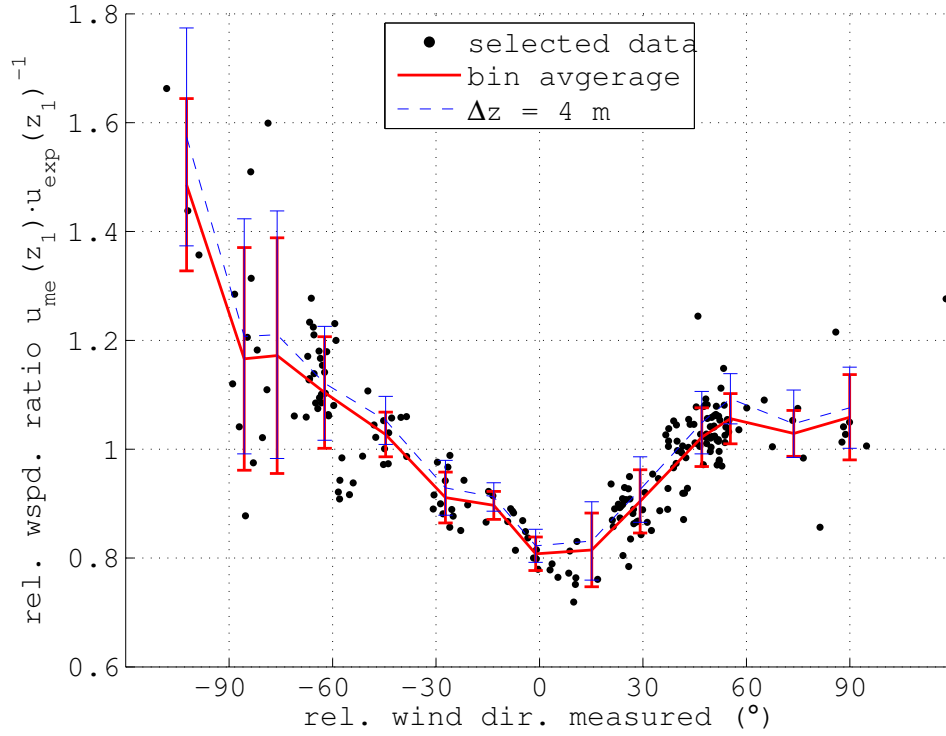


Figure 4.5: Ratio of the measured relative wind speed and the expected relative wind speed, calculated from the buoy wind speed and the ship velocity using (4.23) as function of the measured relative wind direction. The uplift was assumed to be zero ($\Delta z = 0$). Individual measurements and averages that were taken over 15° relative wind direction bins are shown as black dots and red line, respectively. The blue dashed line shows the bin average values for an assumed uplift $\Delta z = 4$ m. The error bars show the standard deviation of the mean.

Figure 4.5 shows the ratio u_m/u_{exp} of the relative wind speed measured at the bow mast and the expected relative wind speed calculated from the buoy. The ratio is given by the acceleration/deceleration a_1 of the wind speed when the streamlines circumvent the ship superstructure and by a potential uplift of the streamlines by the height difference Δz . For this study it was assumed $\tilde{z}_1 = z_1$ i.e. $\Delta z_1 = 0$ and thus $a_1 = u_m(z_1)/u_{\text{exp}}(z_1)$. For $\Delta z_1 > 0$ this could cause an underestimation of a_1 that will increase with the relative wind direction. To estimate the uncertainty in a_1 caused by the unknown height displacement (4.9) was used to calculate \tilde{a}_1 for a constant

$\Delta z_1(\alpha) = 4 \text{ m}$ (dashed blue line in Fig. 4.5). Even for the relatively large $\Delta z = 4 \text{ m}$, the average difference of +3% acceleration is small compared to the large uncertainty in a_1 due to the variability in the wind field.

The relative wind direction measurements and expected values are compared in Fig. 4.6. Positive relative wind directions are overestimated and negative relative wind directions are underestimated, i.e., the magnitude of the measured relative wind direction is always higher than expected. This means that the approaching air is deflected away from the ships structure. The magnitude of the bias increases with increasing relative wind direction but starts to decrease beyond $\pm 90^\circ$; these data exhibit an asymmetric behavior similar to θ and ϕ (see Fig. 4.3).

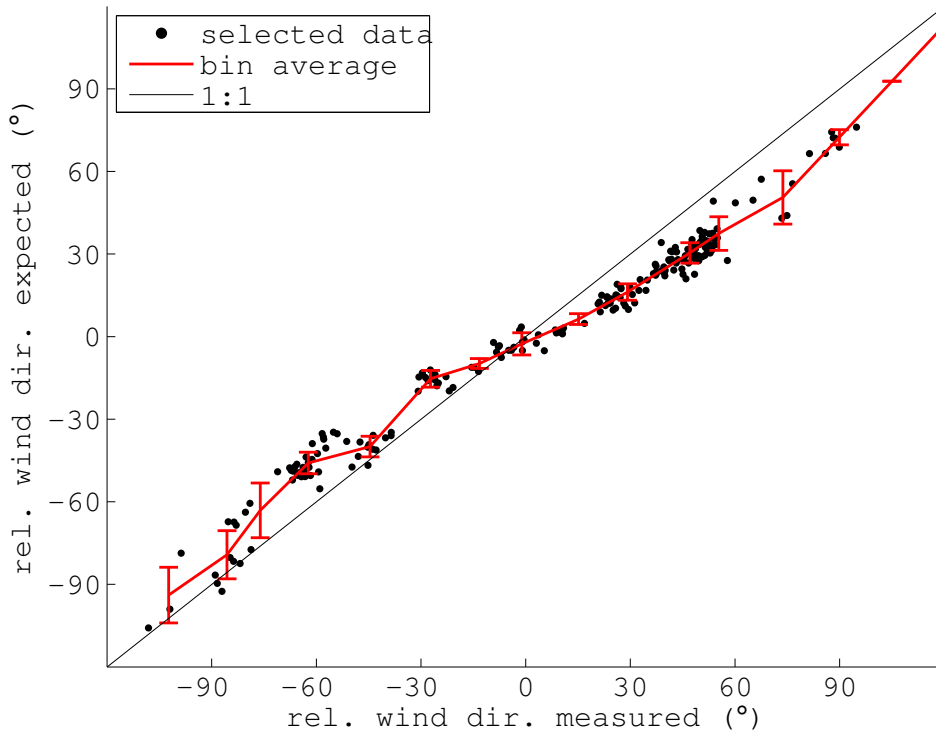


Figure 4.6: Expected relative wind direction calculated from the buoy wind speed and the ship velocity using (4.23) as function of the measured relative wind direction. Individual measurements and averages that were taken over 15° relative wind direction bins are shown as black dots and red line, respectively. The error bars show the standard deviation of the mean.

4.3.4 Correction for Platform Motion and Air Flow

Distortion

The ship motion, platform tilt T_{ep} , and the velocity bias \mathbf{v}_{ship} were calculated for sub-intervals of 12 minutes using the motion correction script from *Miller et al.* (2008). The code was modified to allow for differences in the ship's heading and the actual course. The velocity bias was separated in a mean and fluctuating part as outlined in section 4.2.

The average relative wind direction was calculated from the apparent wind vector. The tilt angles ϕ , θ , ψ , and the acceleration a_1 were derived by linearly interpolating the results from the two nearest wind direction bins. Time series of true wind speed in the local stream line coordinate system were computed (i) using (4.4), (ii) using (4.15) and (iii) using (4.17). The covariances calculated with (4.4), (4.15) and (4.17) will be labelled standard Double Rotation method (DR), radial planar fit method (rPF) and alternative Double Rotation method (DRx), respectively.

4.4 Discussion of Results

4.4.1 Intercomparison of the Bow Mast Wind Speed

Measurements

Figure 4.7 shows the observed ratio of the wind speeds recorded by the 3D sonic anemometer at height z_1 and the 2D vane anemometer at z_2 , which was expected to experience less air-flow distortion due the more exposed

measurement location. The observed ratio does not only depend on the mean relative wind direction, but also on the true wind speed, the platform velocity and the local stability, which are combined in the factor x_a (see (4.13)). Note that the approximation is only valid for $|\alpha_{\text{true}}| \leq 90^\circ$ and near-neutral or unstable conditions. The color scale in Fig. 4.7 indicates the magnitude of the correction factor x_a assuming $\tilde{z}_1 = z_1$ and $\tilde{z}_2 = z_2$. Also shown are bin averages of $a_1 a_2^{-1}$ calculated with (4.13) by (i) ignoring x_a , (ii) assuming $\Delta z = 0$ m, and (iii) assuming $\Delta z = 4$ m. Note the similar shape of $a_1(\alpha) a_2(\alpha)^{-1}$ and $a_1(\alpha)$ in Fig. 4.5.

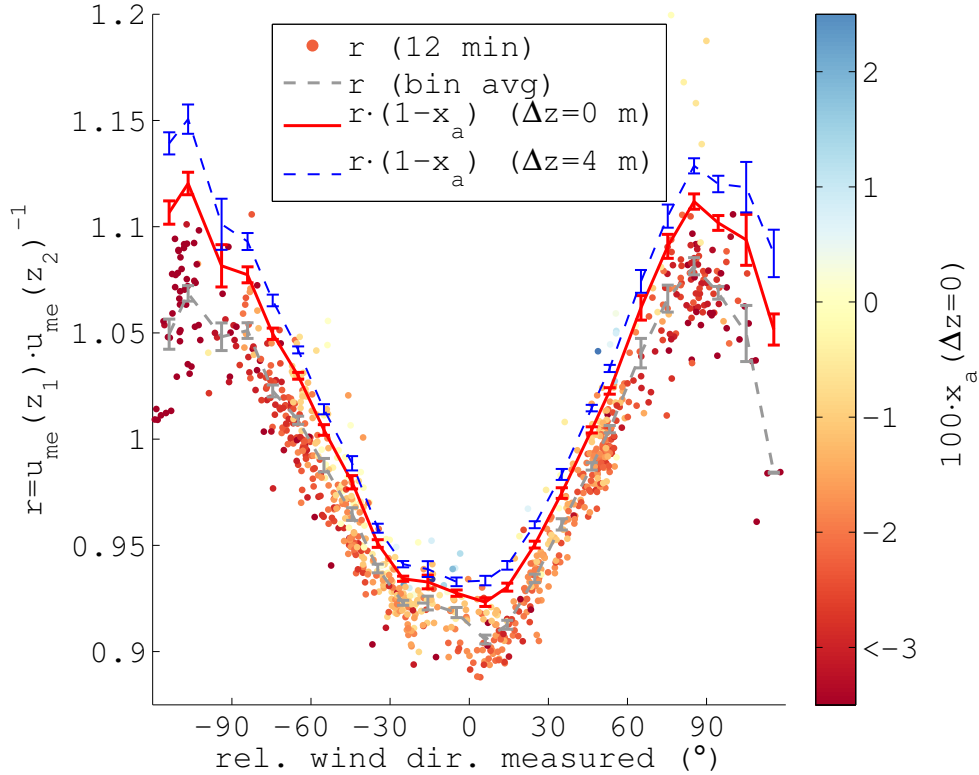


Figure 4.7: Observed ratio (r) of the wind speed measured by the 3D sonic (10 masl) and the 2D vane anemometer (16 masl), as function of the measured relative wind direction. Also shown are the bin averages of r and the ratio of the accelerations $r \cdot (1 - x_a) \approx a_1 a_2^{-1}$, calculated with (4.13), for $\Delta z_1 = \Delta z_2 = 0$ and $\Delta z_1 = \Delta z_2 = 4$ m.

4.4.2 Intercomparison of the Bow Mast Fluxes to the Buoy

In Fig. 4.8 the ratio of u_* measured on the ship and the bulk estimates from the buoy using COARE 3.0 is plotted as function of the relative wind direction. Ratios are shown for EC fluxes calculated with DR, DRx and the rPF tilt correction. The direct u_* , calculated with DR, overestimates the bulk flux estimates from the mooring by 46%; this ratio varies with the relative wind direction, with the largest values occurring at the wind sectors $\pm(20^\circ - 60^\circ)$. The values calculated using DRx are on average 20% higher than the estimates from the buoy and 5% for rPF respectively. From the three ratios the one with rPF shows the least variation with the relative wind direction. Note that at $u_{10N} = 5 \text{ m s}^{-1}$ the u_* values computed with COARE 3.0 are 10% higher than for newest version COARE 3.5 and for $u_{10N} = 10 \text{ m s}^{-1}$ the difference is 2.5%. For this comparison, the data were restricted to the selected time periods marked in Fig. 4.2.

4.4.3 Drag Coefficient and Stress Angle

To demonstrate the effect of the choice of the motion-tilt correction on the measurement of the momentum flux from moving platforms scatter plots of u_* and the square roots of the cross-wind component of the momentum flux calculated with (4.4) and (4.15) and u_{10N} are shown in Fig. 4.9 and Fig. 4.10.

The direct measurements of u_* calculated with (4.4) show a strong dependence on the relative wind direction and a weak correlation with u_{10N} (see Fig. 4.9a). When compared to the COARE 3.5 bulk flux formulation (*Edson*

et al., 2013) the EC u_* values appear largely overestimated. The magnitude of this effect increases with decreasing wind speed as the ratio of u_{me} and u_{true} , and thus the tilt bias, increases (see Fig. 4.4). In contrast the use of (4.15) leads to a significantly better correlation between u_* and u_{10N} (see Fig. 4.9b). The u_* values are mostly higher than the COARE 3.5 results.

The results for the square root of the cross-wind stress of the momentum flux are shown in Fig. 4.10. Over land, the cross-wind stress is expected to be zero. Wind-wave interactions have been proposed as explanation for observed

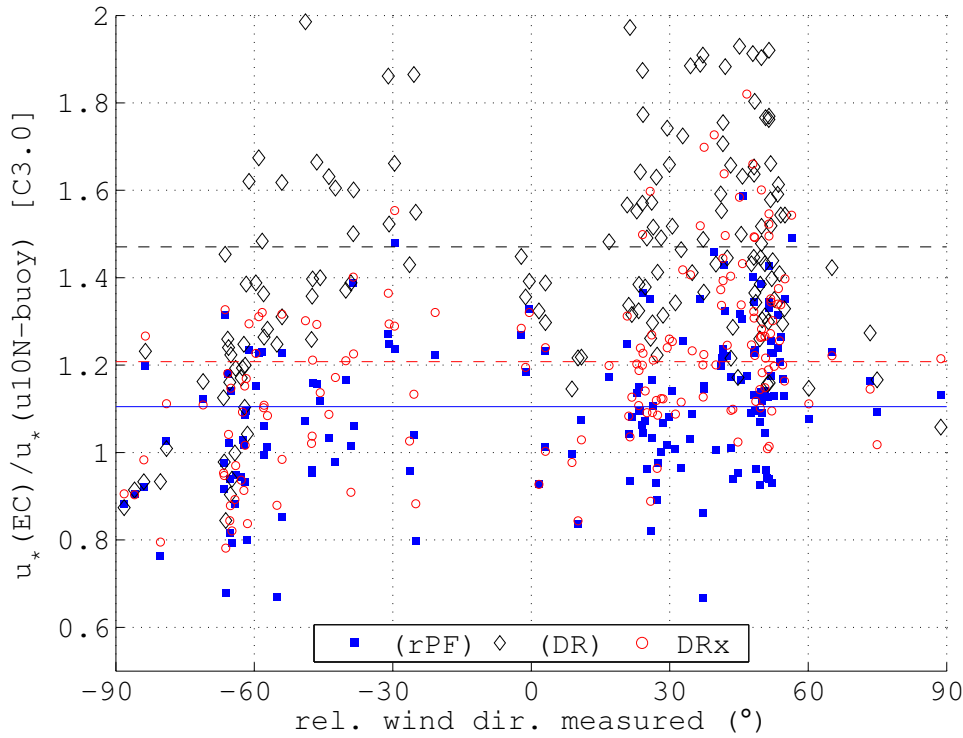


Figure 4.8: Ratio of the EC measurements of u_* on-board the R/V *Saramiento de Gamboa* and the COARE 3.0 bulk flux estimates from the mooring as a function of the measured relative wind direction measured on the ship. Individual 12 min measurements are shown as scatter and average values as lines. Results from the rPF method (4.15) are shown as (blue ■ and —) and results using (DR) as (black ◇ and —), and (DRx) as (red ○ and —), respectively. For this comparison, the data were restricted to the selected time periods marked in Fig. 4.2.

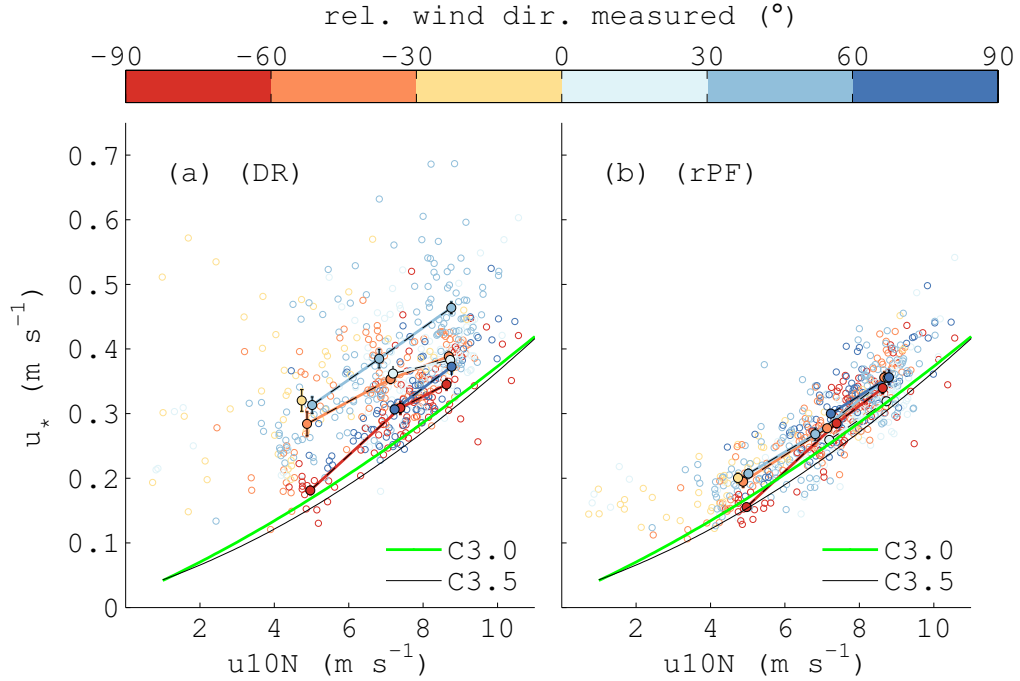


Figure 4.9: Direct measurements of u_* as a function of u_{10N} and the measured relative wind direction: panel (a) shows results obtained using the standard motion correction and rotation into the stream (4.4), and panel (b) shows the results using the rPF method (4.15). Individual measurements (12 min) are shown as (\circ) and bin averages over 30° wind direction and 2 m s^{-1} wind speed bins are shown as thick lines and big \bullet (error bars show the standard deviation). The COARE3.0 and COARE3.5 bulk flux predictions calculated from u_{10N} are shown as green and black line, respectively.

non-zero stress angle (e.g. *Rieder et al.*, 1994). Tilt- and motion-corrected open ocean cross-wind stress measurements on R/P-*FLIP* presented by *Miller et al.* (2008) are on average close to zero and show no correlation with the along-wind stress. *Edson et al.* (1998) and *Pedreros et al.* (2003) presented evidence that ship-borne direct measurements overestimate the cross-wind stress when compared to small platforms (a catamaran and an ASIS buoy), which they attributed to air-flow distortion. The results using (4.4) in Fig. 4.10a show a strong dependence of the average cross-wind stress on the relative wind direction, with the highest magnitudes at wind direction

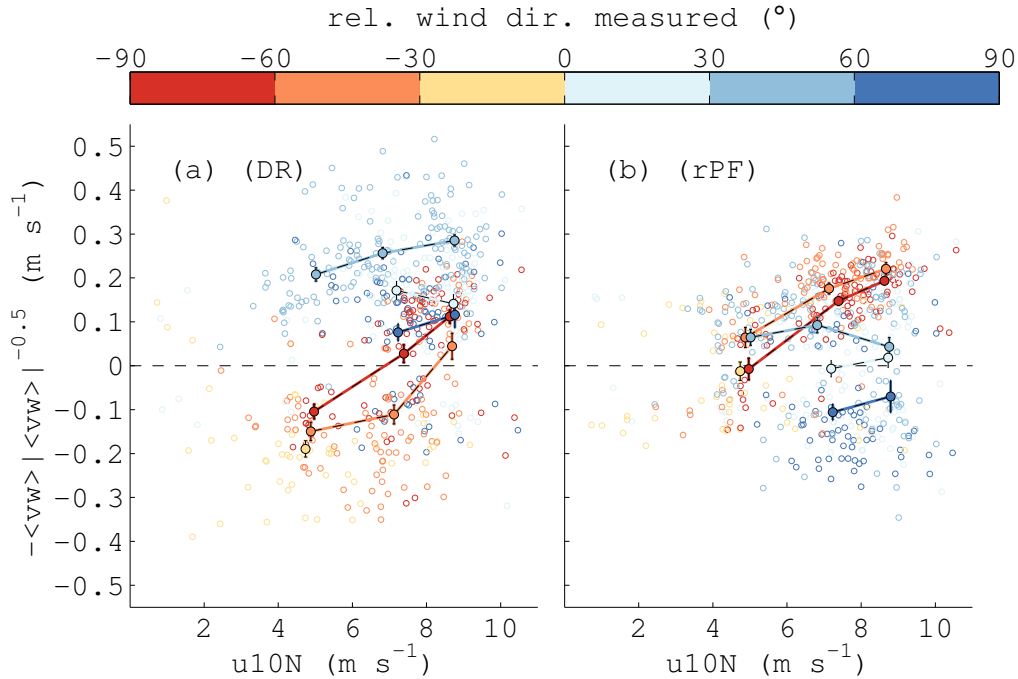


Figure 4.10: Same as fig. (4.9) but for the sign-preserving square root of the cross-wind stress component $-\langle vw \rangle \langle vw \rangle^{-0.5}$. Note positive values indicate downward cross-wind momentum flux.

from $\pm(30$ to $60^\circ)$. The application of (4.15) results in much smaller average cross-wind stress estimates (Fig. 4.10b). The observed strong correlation of the cross-wind stress with wind speed for -90° to -30° appears mostly unchanged by the choice of the tilt correction, but the absolute values of $\langle vw \rangle$ are changed. Note that the positive sign in Fig. 4.10 denotes a downward momentum flux. The wind stress angle for the rPF results was calculated with (4.18) and is plotted in Fig 4.11 as a function of the relative wind direction and u_{10N} . Large stress angles up to $\pm 90^\circ$ are found for low wind speeds. This might be caused by wind-wave interaction, or simply by the fact that the wind direction estimate is not very accurate for low wind speeds. For $u_{10N} > 6 \text{ m s}^{-1}$ a bin average was calculated for 15° wind direction sectors.

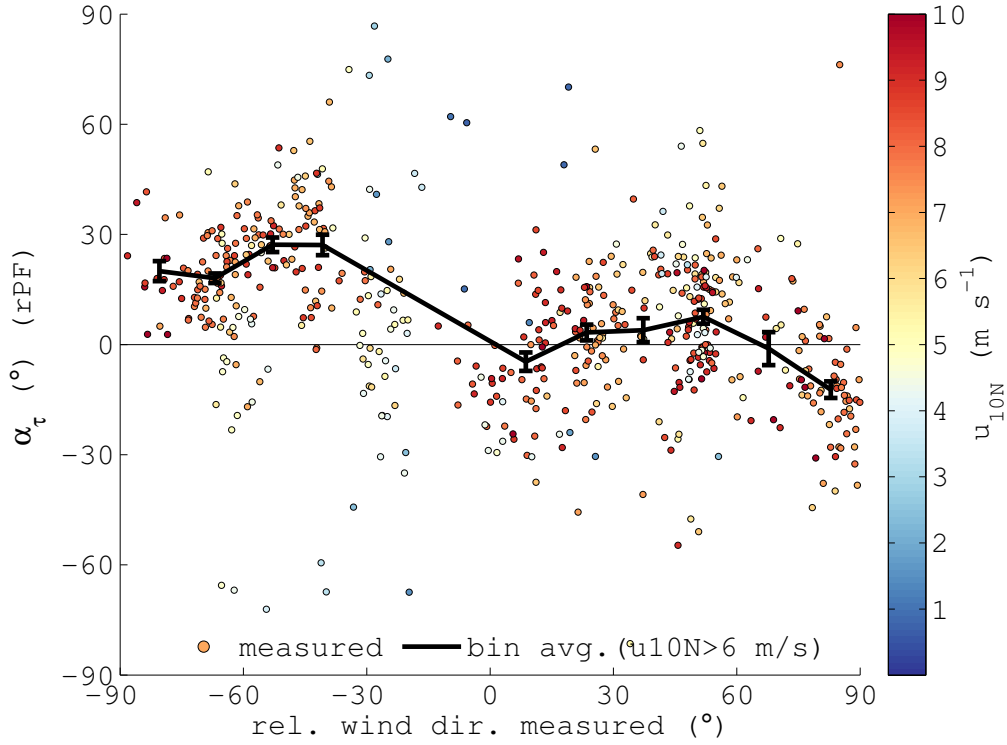


Figure 4.11: Measured stress angle α_τ (using rPF results) as a function of the measured relative wind direction and u_{10N} . The bin averages (shown as black line) are taken for $u_{10N} \geq 6 \text{ m s}^{-1}$ over 15° wind direction bins. Error bars indicated standard deviation from the mean.

I could not identify a physical reason for the high cross-wind stress values at -90° to -30° relative wind direction. Inaccuracies in the estimated wind direction (see Fig. 4.6), which would great interference between along-wind and cross-wind stress, or flow distortion could be possible explanations.

In order to compare the performance of the different corrections for different relative wind directions, the wind speed dependence of u_* is removed (on average) by calculating the ratio of the measured EC u_* and the COARE 3.5 bulk flux prediction for u_* using the flow distortion-corrected wind speed $u_*(u_{10N})[C3.5]$. These ratios are plotted in Fig. 4.12 as a function of the relative wind direction and the wind speed. Also shown are the bin averages of the ratios over the wind speed range $(6 - 10) \text{ m s}^{-1}$.

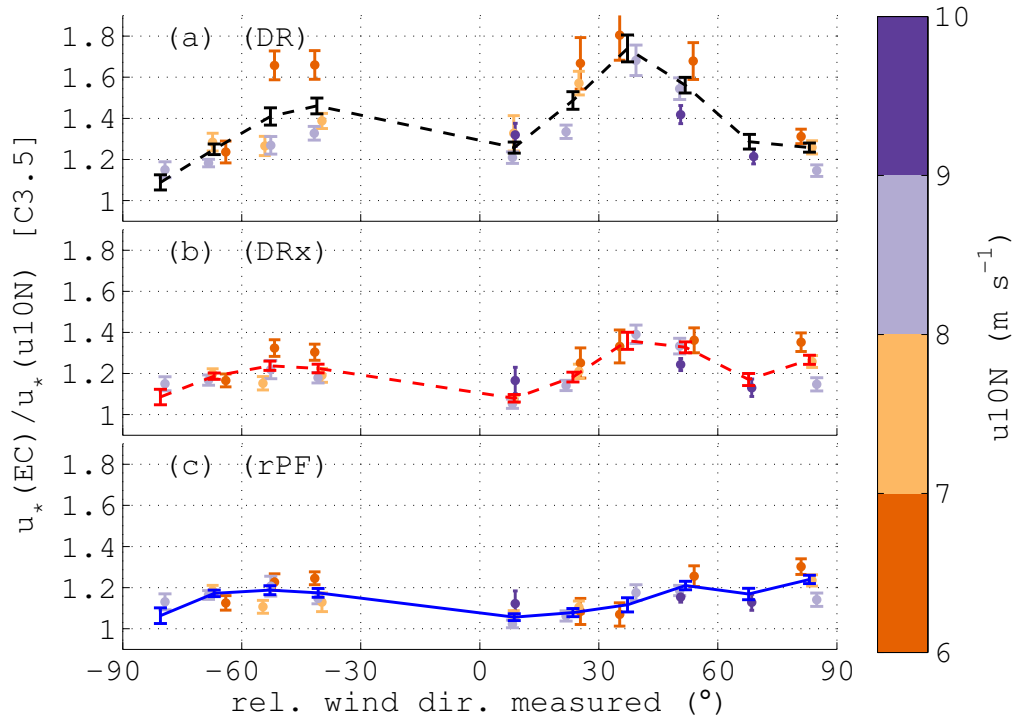


Figure 4.12: Ratio of the u_* measured with EC and the COARE 3.5 bulk flux prediction using u_{10N} as a function of the relative wind direction and the wind speed. The ratios are presented as bin-averaged values over 15° wind direction and 1 m s^{-1} wind speed bins (minimum 6 measurements per bin). Also shown are 15° wind direction bins for $6 \text{ m s}^{-1} \leq u_{10N} \leq 10 \text{ m s}^{-1}$ (minimum 12 measurements per bin). The errorbars indicate the standard deviation. Panel (a),(b), and (c) show the results using DR, DRx, and rPF respectively.

These are replotted in Fig. 4.13 together with the result for using the rPF method but ignoring the roll angle (rPF $\phi=0$). The ratios obtained from the DR method show large variations with the relative wind direction and also with the wind speed, note that the ship was under way with $v_{\text{ship}} \approx 5 \text{ m s}^{-1}$ for most of the measurements. Highest values are reached at $\pm(20 \text{ to } 60^\circ)$, but even for bow on wind direction u_* is overestimated by $\sim 25\%$ when compared to the COARE 3.5 bulk flux prediction. The results from the DRx method show no clear dependence on the wind speed but qualitatively the same dependence on the relative wind direction as the DR results. For

rPF the variation of the ratio with the wind direction is further reduced. But elevated values for $|\alpha| \geq 30^\circ$ indicated that rPF does not completely eliminate the effects of air-flow distortion on the EC flux estimates. However a significant improvement is obvious when compared to DR and DRx. Also shown in Fig. 4.13 is the effect of ignoring the roll offset (ϕ) in the rPF correction. The u_* values for rPF($\phi = 0$) are very similar to the DRx results. In fact the difference between the rPF($\phi = 0$) and DRx results arises from the differences in θ_{DRx} and θ_{rPF} (see Fig. 4.4). The rPF method accounts for the residual vertical wind speed measured by the 3D sonic anemometer (see Fig. 4.3) while DRx does not, which leads to higher estimates for θ .

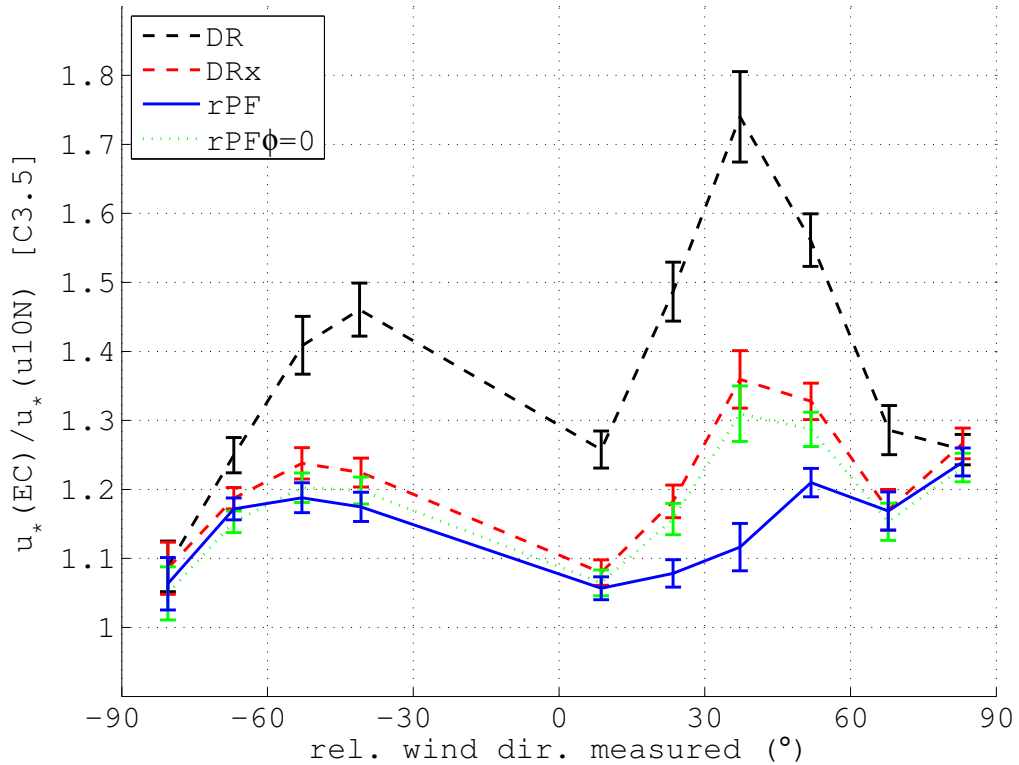


Figure 4.13: The bin average ratios from Fig. 4.12 for DR, DRx, and rPF, for the wind speed range $6 \text{ m s}^{-1} \leq u_{10\text{N}} \leq 10 \text{ m s}^{-1}$. Also shown are the results for setting the roll angle to zero in the rPF correction method (rPF $\phi=0$). Each bin average is based on a minimum of 12 individual measurements.

Note that a ratio of 1 in Figures 4.8, 4.12 and 4.13 does not necessarily imply that the flux measurements are free from air-flow distortion. The variation of $u_*(\text{rPF})$ with the relative wind direction implies, however, that the presented EC flux measurements are significantly biased by air-flow distortion, which cannot be fully accounted for by the tilt correction. It is likely that obstruction of the air flow by the tower on the bow of the *R/V-Saramiento de Gamboa* did contribute substantially to the observed flow distortion bias in the EC flux measurements.

4.4.4 Errors in the Direct Fluxes due to the Standard Motion Correction

In this section the results for u_* , and $\langle wT_{\text{sonic}} \rangle$, obtained using DR and DRx are directly compared with the results obtained by using the rPF method. This is put in context with previous reports about direct comparisons of EC fluxes from ships and buoys.

In Fig. 4.14 the ratios of the u_* values computed with DR, DRx, and $\text{rPF}\phi=0$ and the values computed with rPF are plotted as function of the relative wind direction. The ratios are presented as bin averages over the same 15° wind direction bins as used in Fig. 4.3. This allows to study the part of the flow distortion bias in u_* that is caused by the biased estimation of the wind vector tilts if the DR or DRx methods are used. Note that DR and DRx give identical results for station measurements. Figure 4.15 shows the ratios obtained for the scalar flux $\langle wT_{\text{sonic}} \rangle$.

The bias in u_* is caused by a combination of the pitch and roll offset. This can be seen by comparing the ratio $u_*(\text{DRx})/u_*(\text{rPF})$ with the ratio $u_*(\text{rPF}\phi=0)/u_*(\text{rPF})$ that depends only on the roll offset. This shows that

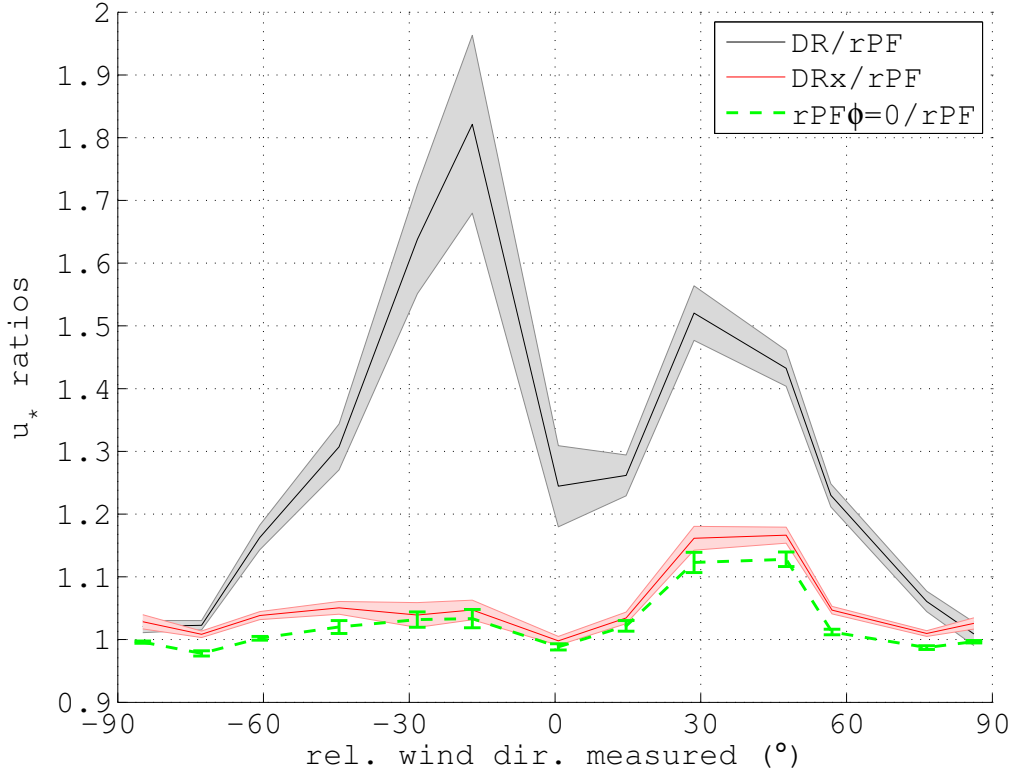


Figure 4.14: Ratios of u_* computed with DR, DRx, and $rPF\phi=0$ and u_* computed with rPF as function of the relative wind direction. The data is presented as bin averages with the standard deviation indicated as shaded area or error bars. Used are the same 15° wind direction bins as in Fig. 4.3.

for the DRx results the bias caused by ignoring the roll is comparable to the bias caused by the slightly overestimated pitch (see Fig. 4.4). The large overestimation of the pitch for the under way measurements in the DR method (see Fig. 4.4) leads to much higher values for the ratio $u_*(DR)/u_*(rPF)$ when compared to $u_*(DRx)/u_*(rPF)$. Due to the contribution of the roll, the ratio $u_*(DR)/u_*(rPF)$ reaches a maximum of 2 for negative and 1.5 for positive relative wind directions.

For the scalar example $\langle wT_{\text{sonic}} \rangle$ the roll offset has almost no effect ($\langle wT_{\text{sonic}} \rangle(rPF\phi=0)/\langle wT_{\text{sonic}} \rangle(rPF) \approx 1$) and the ratio $\langle wT_{\text{sonic}} \rangle(DR)/\langle wT_{\text{sonic}} \rangle(rPF)$ has one distinct maximum for the bow on wind direction. The DRx method

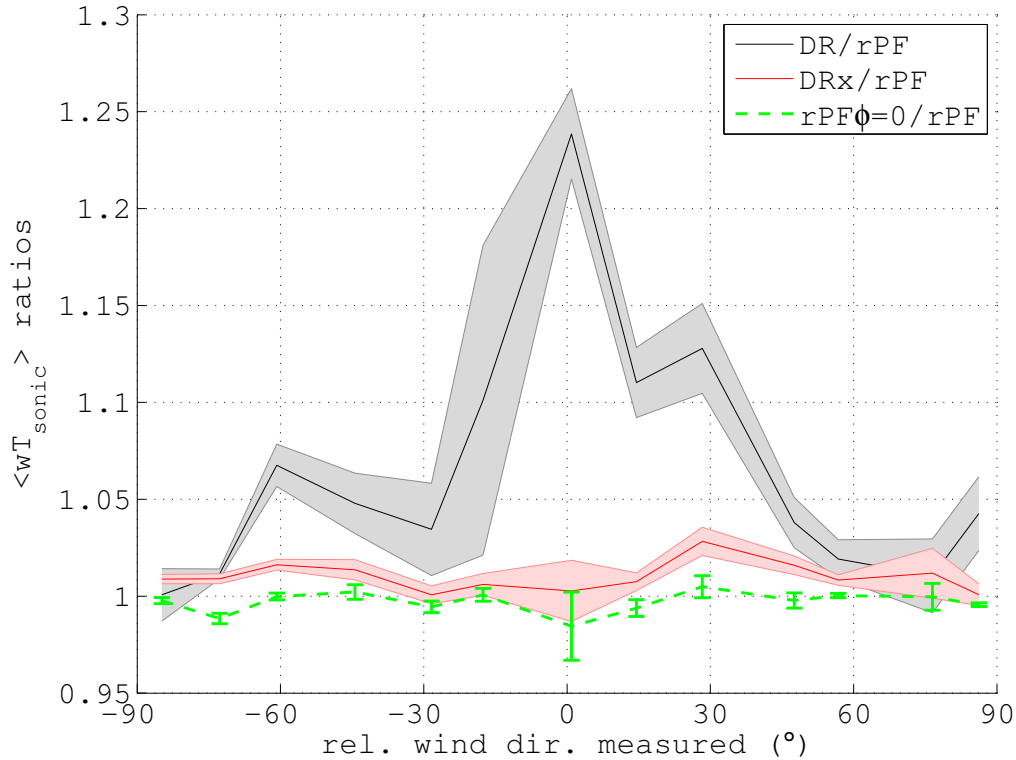


Figure 4.15: Same as Fig. 4.14 but for the ratios of the sonic sensible heat flux $\langle wT_{\text{sonic}} \rangle$.

leads to flux values that are 1 – 3% higher than the results obtained with the rPF method.

Edson et al. (1998) observed an over-estimation of u_* by 8% for $\alpha \leq 120^\circ$ and also reported a wind vector tilt angle of ($3^\circ - 5^\circ$). The tilt angles observed in this study ranged from 6° to 9° , a simple scaling of *Edson et al.* (1998) results would thus lead to 16% over-estimation in u_* . This falls somewhere between our observations for the DR and the DRx method. Unfortunately *Edson et al.* (1998) provide no details about the ratio of wind speed and ship velocity during there experiments. *Pedrerros et al.* (2003) observed a 30% over-estimation in $\langle wu \rangle$ (which equates to 14% for u_*) and 9%; in $\langle wT_{\text{sonic}} \rangle$, for a relative wind direction range restricted to $\alpha \leq 30^\circ$

and with the restriction $\langle u_{me} \rangle \langle v_{ship} \rangle^{-1} \geq 2$. The tilt angle in this study was 7° (Dupuis *et al.*, 2003). Restricting the data set in the same way, average differences between rPF and DR of 26% for u_* and $\sim 14\%$ for $\langle wT_{sonic} \rangle$ were obtain. Note that the narrow restriction of the relative wind direction in (Pedreros *et al.*, 2003) increased the ratio of the average over-estimation of the scalar flux $\langle wT_{sonic} \rangle$ and u_* . This simple comparison shows that the flow distortion effects in direct fluxes, which were reported by Edson *et al.* (1998) and Pedreros *et al.* (2003), are likely explained by the over-estimation of the pitch angle and the neglecting of the roll and yaw of the relative wind vector.

4.4.5 Effect of the Tilt on the Covariance Spectra

The effect of the overestimated wind vector pitch on the measurement of turbulent fluxes was studied using the covariance spectra. Figures 4.16 and 4.17 show the average covariance spectra C_{wu} , C_{wv} and $C_{wT_{sonic}}$ for a 4 hours and 48 minute time period from April 7th 2013 (02:24 to 07:12 UTC) with a steady wind speed ($u_{10N} = 7.1 \pm 0.4 \text{ m s}^{-1}$) and near neutral atmospheric conditions ($z/L \approx -0.15$). The ship was travelling with a constant velocity of ($v_{ship} = 5.1 \pm 0.1 \text{ m s}^{-1}$) and a constant relative direction to the wind field ($\alpha = 25.6 \pm 3^\circ$). The Euler angles tilts due to flow distortion were estimated to ($\phi = 2^\circ$), ($\theta = 8^\circ$) and ($\psi = -12^\circ$). The DR of u_{true} resulted in a pitch estimate $\theta_{DR} = 15^\circ$, almost twice the value estimated by the rPF method and in a true wind direction bias $\Delta\psi = -25^\circ$.

The covariance spectra computed from $(u, v, w,)$ estimated using (4.15) have similar shape as expected (Kaimal *et al.*, 1972). The spectra computed using (4.4), however, exhibit increased energy levels at low frequencies. For

frequencies above 1 Hz, $nC_{wT_{\text{sonic}}}$ remains unchanged, while nC_{wu} is reduced and nC_{wv} increased slightly in magnitude.

Similar to the calculations by *Wilczak et al.* (2001), Kaimal model spectra for the tilted coordinate system ($\Delta\phi = \phi$, $\Delta\theta = \theta_{\text{DR}} - \theta$, and $\Delta\psi = \alpha_{\text{true,DR}} - \alpha_{\text{true,rPF}}$) were calculated using small angle approximation and assuming $C_{wv} = C_{uv} = C_{vT_{\text{sonic}}} = 0$ and $\cos(\Delta\phi) = 1$:

$$(C_{wu})_{\text{tilt}} \approx C_{wu} \cos(\Delta\theta) \cos(\Delta\psi) + 0.5(S_w - S_u) \sin(2\Delta\theta) \quad (4.24)$$

$$(C_{wv})_{\text{tilt}} \approx -C_{wu} \sin(\Delta\psi) + 0.5(S_w - S_v) \sin(2\Delta\phi) \quad (4.25)$$

$$(C_{wT_{\text{sonic}}})_{\text{tilt}} \approx C_{wT_{\text{sonic}}} \cos(\Delta\theta) - C_{uT_{\text{sonic}}} \sin(\Delta\theta) \quad (4.26)$$

The results are shown as grey lines in Figs. 4.16 and 4.17. Using the Kaimal spectra ignores the high energy levels, which were found in S_u, S_v at low frequencies (see Fig. 3.6), and can therefore explain only a part of the changes in co-spectral energy at this range.

Based on (4.24) and (4.25) the behaviour of $(C_{wu})_{\text{tilt}}$ and $(C_{wv})_{\text{tilt}}$ above 1 Hz can be explained with the isotropy $S_u \approx S_v \approx S_w$. In this frequency range θ becomes irrelevant and error is solely given by the yaw bias, leading to parts of C_{wu} being misinterpreted as C_{wv} .

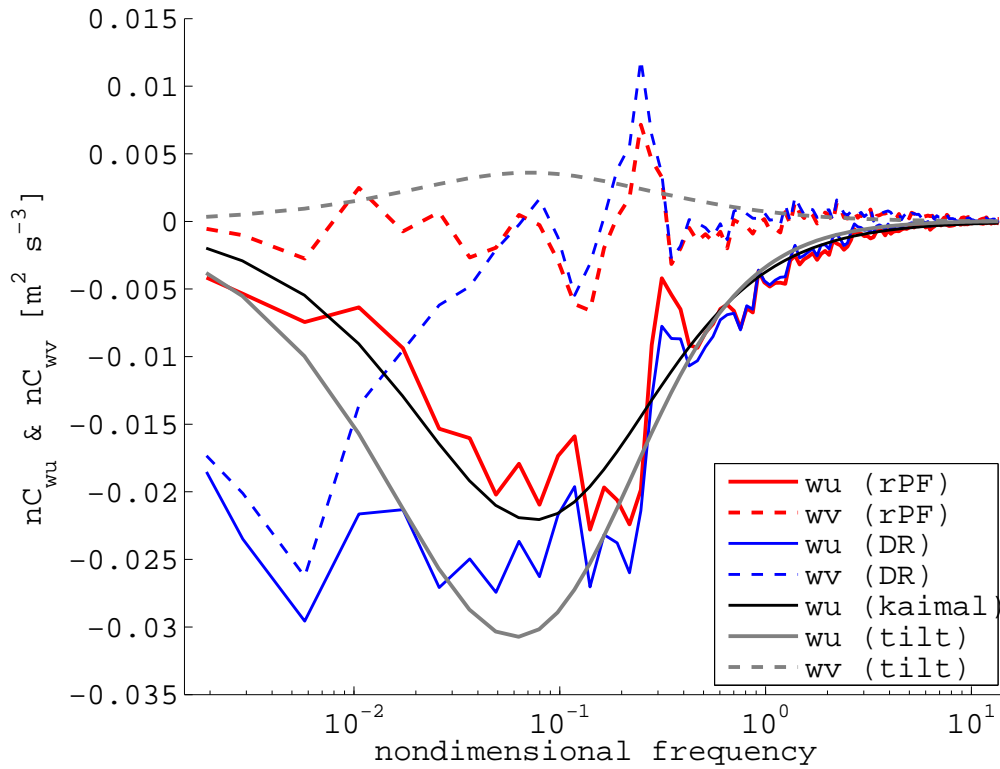


Figure 4.16: Average of 24 12 minute frequency weighted co-spectra from April 7th, 2013 (02:24 - 07:12), a period of constant wind speed ($u_{10N} = 7.1 \pm 0.4 \text{ m s}^{-1}$) and ship velocity ($v_{\text{ship}} = 5.1 \pm 0.1 \text{ m s}^{-1}$). The relative wind direction was ($\alpha = 25.6 \pm 3^\circ$). Shown are nC_{wu} and nC_{wv} , calculated using (4.15) with flow distortion Euler angles ($\phi = 2^\circ$), ($\theta = 8^\circ$) and ($\psi = -12^\circ$). Co-spectra calculated using (4.4), with estimated pitch ($\theta_{\text{DR}} = 15^\circ$), are shown in blue. The black line shows the Kaimal spectrum and the grey lines show the expected Kaimal spectra for the tilted (DR) coordinate system estimated using (4.24) and (4.25).

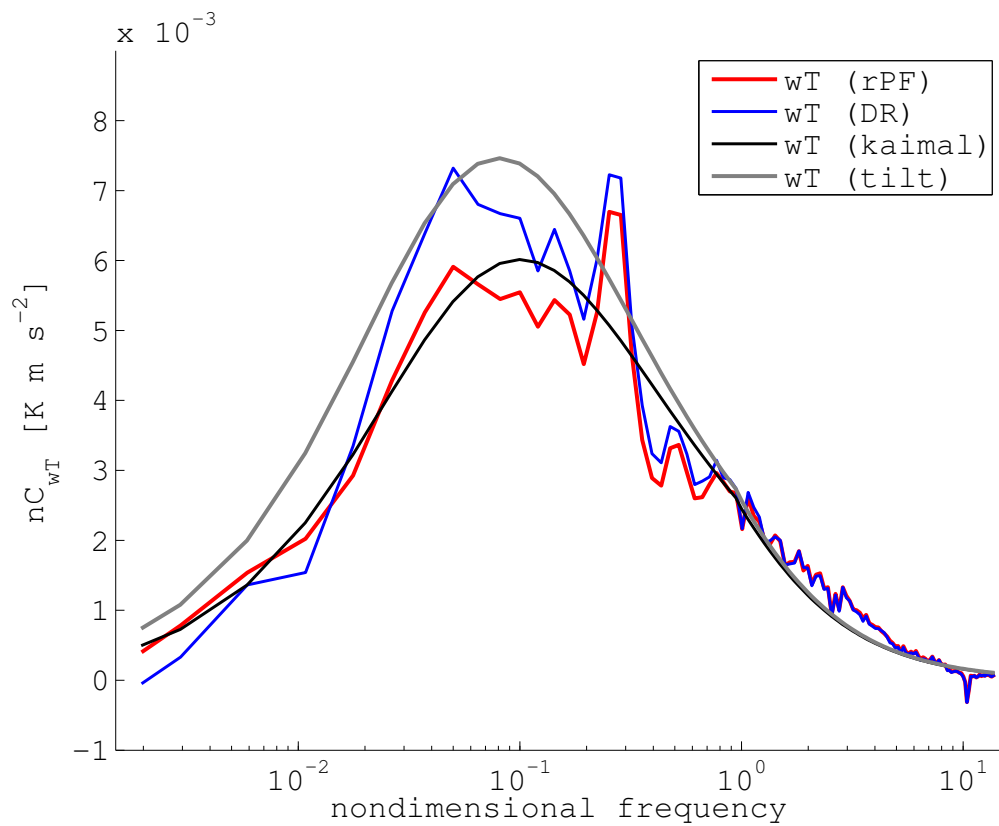


Figure 4.17: Same as Fig. 4.16 but for the covariance of the vertical wind speed and the speed of sound temperature fluctuations.

4.5 Conclusions for the Motion-Tilt Correction

I showed that the commonly used motion correction procedure (4.4) leads to an incorrect estimation of the wind vector tilt, which is reflected in an over-estimation of the direct fluxes. This bias is caused mainly by errors in the pitch of the wind vector, when (4.4) is applied to measurements from a ship under way. This is because $\langle w \rangle$ scales with the relative wind speed u_{me} and not with u_{true} . Additionally, (4.4) does not account for a roll of the wind vector. This is relevant for both under way and station measurements. Air-flow distortion can also lead to a biased measurement of the wind direction. Typically the magnitude of the measured relative wind direction is higher than the true relative wind direction. This can lead to errors in the stress angle, however the yaw of the wind vector has no effect on scalar fluxes and on the estimation of u_* with (4.2). For the typical measurement situation of a research vessel heading into the wind, covariance moments calculated with (4.4) will overestimate the vertical flux; the sign of the cross-wind stress bias does, however, depend on the relative wind direction. I could also show that predominantly the low frequency part of the covariance spectra is affected by the tilt of the coordinated system.

In this study, the bias caused by the motion correction procedure (4.4) was in the range of 0 – 50% for u_* and 0 – 25% for $\langle wT_{sonic} \rangle$ for a wind direction range of $\pm 90^\circ$. The effect for other air-sea gas exchange studies will depend on the magnitude of the wind vector tilt, the ratio of true and relative wind speed, and, to some extent, on the atmospheric stability and the height of the boundary layer (*Wilczak et al.*, 2001). I suggest that this is the main cause for the observed over-estimation of air-sea fluxes, when

measured on research vessels (e.g. *Edson et al.*, 1998; *Pedrerros et al.*, 2003).

I presented a different approach to correct for ship motion and wind vector tilt (4.15), and have shown that it can successfully reduce air-flow distortion bias in the direct flux measurements. The required pitch and roll of the relative wind vector can be derived from the measured wind speeds using the rPF method (4.20) based on wind direction sectors. The estimation of yaw bias and acceleration of the mean wind speed does, however, require an independent free stream measurement or alternatively the use of computational fluid dynamics models (*O'Sullivan et al.*, 2014).

With (4.17) I also presented an alternative to (4.4) which avoids the large over-estimation of the wind vector pitch for under way measurements. It does not account for a potential roll or yaw of the wind vector due to air-flow distortion and is subject to random measurement errors caused by relatively short averaging periods and statistical errors due to imperfections in the anemometer calibration. I suggest the rPF method to be used instead of the DR and DRx approach.

The technique presented here could be used to extend the number of high quality flux measurements available for air-sea interaction studies. For example, *Fairall et al.* (1996a) restricted covariance data not only by relative wind direction within 30° of the bow, but also by the pitch of the wind vector (estimated from the DR method) less than 10° . This essentially removes under way measurements at relative low wind speeds. A reanalysis of previous EC datasets could be a straightforward solution to provide more data to improve the COARE algorithm.

These findings are most relevant for ship-borne direct flux measurements and derived bulk parameterizations of air-sea exchange processes, but also apply, to a lesser extent, to stationary flux measurements when air-flow

distortion cannot be avoided.

Two MATLAB scripts that derive the pitch and roll angle via the rPF method and to apply it to the wind speed measurements, are made available at <http://airsea.nuigalway.ie/scripts>.

5 Analysis of the PKT correction for direct CO₂ fluxes

Preface

This chapter is an adapted version of the article:

Landwehr, S., S. D. Miller, M. J. Smith, E. S. Saltzman, and B. Ward, (2014). Analysis of the PKT correction for direct CO₂ flux measurements over the ocean. *Atmos. Chem. Phys.*, **14**, 3361 - 3372.

The primary goals of *Landwehr et al.* (2014) were (i) to demonstrate the non-validity of PKT correction as presented by *Prytherch et al.* (2010a), and (ii) to show that the (*Miller et al.*, 2010)-method of measuring CO₂ at dry air can be used to obtain high quality direct CO₂ flux measurement. We were motivated to publish these results in order to highlight the issues associated with open-path measurements.

The right to share and adapt this work is freely available under the Creative Commons Attribution 3.0 License. The data analysis, the interpretation and synthesis of results, the production of figures and the writing were done exclusively by the author of this thesis. Dr. Ward contributed by supervising, assisting and reviewing the work and by providing the in-

frastructure (computer time, travel costs, additional instrumentation, etc.) required to carry out this research project. Dr. Miller provided the Eddy Covariance Flux setup and supported the data-analysis. Data collection was done by the author. Dr. Smith contributed measurements of mean meteorological parameters and the calculation of bulk fluxes. Dr. Saltzman provided assisting and reviewing of the publication.

5.1 Introduction

Direct measurements of air–sea CO₂ flux contribute to the understanding of the Earth climate system and can be used to study the fundamental physics of air–sea gas exchange. When direct flux measurements are combined with the measurement of the partial pressure gradient of CO₂ across the air–water interface, $\Delta p\text{CO}_2$, the gas transfer velocity k can be derived as follows (e.g. *Wanninkhof, 1992*):

$$k = \frac{F_c}{K_{0\text{CO}_2}\Delta p\text{CO}_2} \quad (5.1)$$

where $K_{0\text{CO}_2}$ is the solubility of CO₂ in sea water and F_c is the vertical CO₂ flux. The ability to parameterise k is essential for modelling global air–sea CO₂ fluxes based on $\Delta p\text{CO}_2$ climatologies (*Takahashi et al., 2002*), and for increasing our understanding of the global oceanic uptake of CO₂ (*Ward et al., 2004*).

In the eddy covariance (EC) method, the turbulent flux is directly calculated from the covariance of the fluctuations in the vertical wind speed (w')

and fluctuations in the CO₂ mixing ratio in dry air (x'_c):

$$F_c = \langle n_d \rangle \langle w' x'_c \rangle \quad (5.2)$$

where n_d is the dry air density (here $\langle \rangle$ indicates a time average over a time interval t_I and the primes denote deviations from the mean). The w' and x'_c parameters need to be sampled fast enough to resolve the smallest flux-carrying eddies (typically 10 Hz), and the averaging interval needs to be long enough to include large scale motions that contribute to the vertical flux, but short enough to ensure stationarity of the relevant parameters during the interval (typically t_I are between 15–60 min) (*Kaimal et al.*, 1972). The EC method thus allows the study of gas transfer with much higher time resolution than both dual tracer experiments (e.g. *Nightingale et al.*, 2000; *Ho et al.*, 2006) and measurements of the ¹⁴C concentration in sea water (e.g. *Wanninkhof*, 1992; *Sweeney et al.*, 2007).

Commonly-used broadband infrared gas analysers (IRGA), such as LICOR LI7500 and LI7200, measure the CO₂ concentration n_c (number of molecules per volume), from which the mixing ratio needs to be calculated. Therefore, simultaneous measurements of temperature T , pressure P , and water vapour concentration n_v are necessary to calculate the dry air density $n_d = (P/RT - n_v)$ and the CO₂ mixing ratio $x_c = n_c n_d^{-1}$ (*Webb et al.*, 1980). Equation (5.2) can be written as the sum of the flux measured by the IRGA and a bias flux, caused by the fluctuations of the dry air density, i.e.:

$$F_c = \underbrace{\langle n'_c w' \rangle}_{F_{\text{IRGA}}} + \underbrace{\langle x_c \rangle \cdot \left[\langle n'_v w' \rangle + \frac{\langle n_d + n_v \rangle}{\langle n_d \rangle} \cdot \left(\frac{\langle T' w' \rangle}{\langle T \rangle} - \frac{\langle P' w' \rangle}{\langle P \rangle} \right) \right]}_{F_q + F_T + F_P} \quad (5.3)$$

For CO₂, the bias terms due to the water vapour, temperature and pressure fluctuations in the sample volume (F_q , F_T and F_P , respectively) can easily exceed the vertical flux by an order of magnitude because the fluctuations x'_c are small compared to the background $\langle x_c \rangle$ (*Webb et al.*, 1980). Equations (5.3) and (5.2) are fully equivalent.

EC is considered a standard method over land, but the application over the open ocean has proved to be more challenging. In the case of ship-based studies, the wind speed measurement needs to be carefully corrected for platform motion (e.g. *Edson et al.*, 1998; *Miller et al.*, 2008). Over land, the pressure term in Eq. (5.3) can be ignored, but at sea the platform motion-induced pressure fluctuations can introduce a further bias flux as they may correlate with residuals of ship motion signal in the motion-corrected wind speed (*Miller et al.*, 2010). CO₂ fluxes over the ocean are typically much smaller than over land, and with currently available sensor technology (e.g. Licor 7500/7200 have a resolution of 0.11 ppm at 10 Hz sample rate), a relatively high air–sea gradients $\Delta p\text{CO}_2 \geq 40 \text{ } \mu\text{atm}$ is required to keep the uncertainty in the flux signal due to sensor resolution below 10% (*Rowe et al.*, 2011).

For EC, the trace gas measurement has to be carried out on the same air sample as the wind speed measurement. This can be done directly using an open-path (OP) IRGA, which is located close to the sonic anemometer (*Kondo and Osamu*, 2007; *Yelland et al.*, 2009; *Prytherch et al.*, 2010b). Alternatively, air can be pumped to a distant closed-path (CP) IRGA, at a sufficiently high flow rate (e.g. *McGillis et al.*, 2001a). This allows deliberate pre-conditioning of the air sample, such as removal of the temperature and water vapour fluctuations and the application of in-line particle filters to avoid the deposition of salt or dust particles on the sensor lenses. *McGillis*

et al. (2001a) were the first to carry out EC measurements of the air–sea CO₂ flux, which were in general agreement with common bulk flux formulae. *Miller et al.* (2010) developed a CP system where 97% of the water vapour flux signal is removed by passing the air flow through a membrane dryer. This significantly lowered the magnitude of the air density correction term in Eq. (5.3).

Attenuation of the fluctuations within the sample tube of CP systems can lead to an underestimation of the turbulent transport carried by the small high frequency eddies (*Leuning and King, 1992*). To minimise this effect the flow must be kept fully turbulent (with a Reynolds number $Re \gtrsim 2100$). This requires flow rates of about 100 slpm. Therefore, CP systems have higher power and maintenance requirements than OP systems.

In the oceanic environment, the lenses of OP IRGAs are prone to the build-up of salt particles, and flushing with fresh water is necessary to avoid degradation of the signal. The LI7500 has also been deployed with a shroud and a very high airflow (570 slpm) (*Edson et al., 2011*). This deployment mode is a hybrid of the OP and CP mode as the contamination with sea spray is reduced with minimal loss of high frequency fluctuations. Even when the air density correction Eq. (5.3) has been applied carefully, reported CO₂ flux values based on OP and shrouded OP EC systems over the open ocean are typically an order of magnitude higher than expected based on generally accepted bulk flux parameterisations (*Kondo and Osamu, 2007; Prytherch et al., 2010a; Lauvset et al., 2011; Edson et al., 2011*).

The exact reason for the additional bias is still unclear. *Kohsiek* (2000) suggested that the build-up of water films on the sensor lenses could lead to a biased CO₂ measurement x_{cm} with dependency on the relative humidity (RH). This will cause a bias in the CO₂ flux measurement F_{cm} , which

scales with the latent heat flux because the fluctuations of the water vapour concentration in the sample volume will lead to artificial fluctuations in x_{cm} . Removing this artificial cross-correlation is difficult because there is a natural correlation between the fluctuations of the two scalars x_c and x_v , which are both transported by the same turbulent eddies. Attempting to remove the artificial dependency $x_{cm}(\text{RH})$ with regressions or polynomial fits can thus lead also to the removal of the turbulence-driven variations of x_c and, therefore, of the CO₂ flux signal itself. *Prytherch et al.* (2010a) suggested that the accumulation of salt particles on the lens of the LI7500 OP IRGA could modulate the magnitude of the bias. *Edson et al.* (2011) reported that the accumulation of salt particles on their shrouded and regularly cleaned IRGAs was unlikely and suggested that a more suitable explanation was provided by the contamination of the optics with small particles from the ship's engines combined with organic deposits from sea spray. *Prytherch et al.* (2010a) went further and presented a correction method (called the Peter K. Taylor – PKT – method), which has since been used in several publications to correct OP CO₂ fluxes (e.g. *McVeigh*, 2009; *Prytherch et al.*, 2010b; *Lauvset et al.*, 2011; *Edson et al.*, 2011; *Huang et al.*, 2012; *Ikawa et al.*, 2013). The PKT correction assumes that the true fluctuations of the CO₂ mixing ratio (x'_c) can be calculated from the measured fluctuations (x'_{cm}) by subtracting a bias term that is proportional to the fluctuations of the H₂O mixing ratio (x'_v):

$$x_c = x_{cm} - \mu x_v \tag{5.4}$$

here the cross talk coefficient (μ) is a variable factor that is determined iteratively. *Edson et al.* (2011) advanced this method by allowing μ to

depend on the frequency ω of the fluctuations:

$$C_{wx_c}(\omega) = C_{wx_{cm}}(\omega) - \mu(\omega)C_{wx_v}(\omega) \quad (5.5)$$

Here $C_{xy}(\omega)$ stands for the co-spectrum of two quantities x and y . The spectral crosstalk coefficient is given by:

$$\mu(\omega) = \frac{C_{x_vx_{cm}}(\omega)}{S_{x_vx_v}(\omega)} - \frac{C_{x_vx_c}(\omega)}{S_{x_vx_v}(\omega)} \quad (5.6)$$

where $S_{xx}(\omega)$ stands for the variance spectrum of x . *Edson et al.* (2011) determine the crosstalk coefficient μ by assuming that the ratio of the true and measured covariance of the CO₂ and H₂O mixing ratios can be approximated by a constant value (Γ):

$$\mu(\omega) = \left(1 - \frac{C_{x_vx_c}(\omega)}{C_{x_vx_{cm}}(\omega)}\right) \frac{C_{x_vx_{cm}}(\omega)}{S_{x_vx_v}(\omega)} \approx \Gamma \frac{C_{x_vx_{cm}}(\omega)}{S_{x_vx_v}(\omega)} \quad (5.7)$$

Edson et al. (2011) estimated $\Gamma \approx 0.88$ by tuning their results to fit the PKT correction on average and used (5.5) to correct direct flux measurements from the Southern Ocean Gas Exchange Experiment. The derived gas transfer velocities support a cubic relationship of k_{660} with u_{10N} .

Huang et al. (2012) reported that the PKT correction did bring some of their CO₂ flux measurements closer to the bulk flux estimate, but found that for small water vapour fluxes the PKT method overcorrected the CO₂ flux and, in some cases, even resulted in a reversal of the flux direction. *Ikawa et al.* (2013) reported that the PKT correction resulted in increased scatter when applied to coastal tower-based CO₂ flux measurements, and decided not to apply the correction. *Blomquist et al.* (2014) applied the spectral correction (5.5). Using CO₂ fluxes, measured with an LI-7200 at dry air

as reference, they found two different Γ values for two different open-path gas analysers ($\Gamma = 0.93$ and $\Gamma = 1.1$)*. *Blomquist et al.* (2014) suggest, that CO₂ fluxes measured at dry air have superior quality over open-path measurements, but might not be suitable for autonomous deployments, e.g. on buoys. A selection of the publications mentioned above are also listed in Table 5.1 together with a brief description of the deployed IRGAs and findings relevant to this contribution.

Here direct CO₂ flux measurements performed during the Surface Ocean Aerosol Production (SOAP) experiment in the Southern Ocean are presented, where the SUNY Albany Air/Sea Flux system (*Miller et al.*, 2010), consisting of dried and un-dried CP IRGAs was deployed. In order to rule out that the failure of an individual IRGA would suggest differences between the dried and un-dried deployment, the number of IRGAs was doubled using sensors from NUIG.

We show that even EC measurements using CP IRGAs can be affected by a large humidity bias when the sampled air is neither dried nor filtered. We applied the PKT method (which does not include any OP-specific assumptions) to the un-dried CP data as a test of its ability to remove the observed humidity flux-related bias in broadband non-dispersive infrared (NDIR) sensors.

We further analyse and discuss four particular issues regarding the presented flux measurements: (i) the PKT correction method (*Prytherch et al.*, 2010a), (ii) the effect of air-flow distortion to the direct fluxes, (iii) potential bias in the *dry* CO₂ fluxes due to residual water vapour fluctuations down stream of the diffusion dryer, and (iv) the potential underestimation of the fluxes due the attenuation of high frequency fluctuations in the tubing.

*It should be noted that a 10% error in a correction factor, which can easily be 10 times larger than the signal, still leads to a 100% error in the corrected value.

Table 5.1: Publications addressing the bias in NDIR CO₂ measurements that is related to relative humidity.

Publication	Configuration	Notes
<i>Kohsiek (2000)</i>	two custom-made NDIR sensors	Laboratory tests show dependency of the CO ₂ signal on RH for RH \geq 50%. Author suggests water-films on the sensor optics as cause
<i>McGillis et al. (2001a)</i>	LI-6262 closed-path with in-line particle filter	first air-sea EC CO ₂ fluxes consistent with bulk formula
<i>Kondo and Osamu (2007)</i>	LI-7500 open-path	measured CO ₂ fluxes order of magnitude higher than bulk formula
<i>Miller et al. (2010)</i>	LI-7500 converted to closed-path, dried air-stream	reduced Webb correction CO ₂ fluxes consistent with bulk formula
<i>Prytherch et al. (2010a)</i>	LI-7500 open-path + PKT	suggest water films caused by salt particles as cause; apply an order of magnitude correction
<i>Prytherch et al. (2010b)</i>	LI-7500 open-path + PKT	transfer velocity measurements at high wind speeds; apply order of magnitude correction
<i>Lausset et al. (2011)</i>	LI-7500 open-path + PKT	order of magnitude correction
<i>Edson et al. (2011)</i>	LI-7500 shrouded + PKT and spectral method	suggest small particles on sensor lenses as cause; order of magnitude correction
<i>Kondo and Tsukamoto (2012)</i>	LI-7500 open-path and LI-7000 closed path	measured CO ₂ fluxes from both sensors are an order of magnitude higher than bulk formula
<i>Huang et al. (2012)</i>	LI-7500 open-path on buoy	find PKT results not plausible
<i>Ikawa et al. (2013)</i>	LI-7500 open-path on coastal tower	find PKT results not plausible
<i>Blomquist et al. (2014)</i>	LI-7500 open-path, LI-7200 and PICARRO closed-path	PKT, spectral method and dry fluxes suggest drying is better than correcting
This study	LI-7500 <i>Miller et al. (2010)</i> compared to LI-7200 closed path + PKT	dry CO ₂ fluxes consistent with bulk formula; un-dried CO ₂ fluxes biased low; disproves PKT correction

5.2 Experiment and methods

The SOAP field campaign was conducted from February to March 2012 on the R/V *Tangaroa*. The EC system described here consisted of two Csat3 sonic anemometers attached to the bow mast (12.6 m a.s.l.), which provide high frequency measurements of the three components of the wind vector (u , v and w) and the speed of sound temperature (T_{sonic}), as well as four IRGAs of the type LI7200 ($\times 2$) and LI7500 ($\times 2$), which were located inside the container laboratory on the bow deck and connected to the sample volume on the mast with a stainless steel tube (ID = 1 cm; $L = 20$ m). The inlet tube was heated to avoid condensation on the walls, which would lead to an underestimation of the EC latent heat flux. Although the tubing had an inbuilt self-regulated heating resistor (Parker SL-522-B0849A), the temperature in the tubing was not measured continuously. However the LICOR temperature sensors recorded temperatures ranging from 23°C to 36°C at an outside air temperature ranging from 8°C to 16°C. A pump (Gast model 1423) delivered a continuous air stream from the mast at 100 slpm ($Re \approx 7500$), where Re is computed as $Re = \frac{Q \cdot 2R}{\nu \cdot \pi R^2}$, using a flow rate Q [ms^{-1}], the inner radius of the tubing R [m] and the kinematic viscosity of air $\nu \approx 7.1 \cdot 10^{-6} \text{m}^2 \text{s}^{-1}$. Figure 5.1 shows a schematic of the flux system.

A part of the main flow (17 slpm; ID = 6 mm; $L = 2$ m; $Re \approx 2100$) was directed to the two LI7200s CP IRGAs (*wetA*, *wetB*) connected in sequence. Up to this point the air was not filtered. The air stream was subsequently divided and passed to two LI7500s, which were connected in parallel. The 7500 OP units were converted to CP and each one was

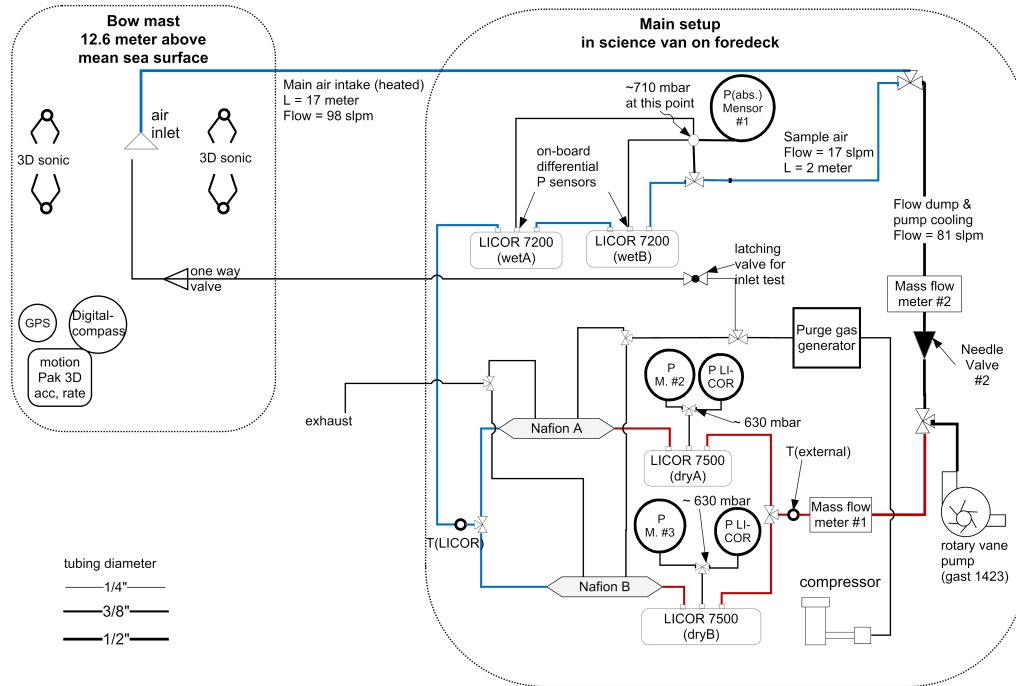


Figure 5.1: Schematic of the Eddy Covariance setup for the SOAP experiment on the R/V *Tangorua*. The sample air line is colour-coded in blue and the colour is changed to red downstream of the membrane dryers to indicate that the air is dried at this point.

positioned downstream of a Nafion membrane dryer (PD-200T) to remove fast water vapour fluctuations as shown by *Miller et al.* (2010). They are described as (*dryA* and *dryB*) in the following text.

Zero air was injected periodically (every 6 h) into the sample inlet to measure the delay of the signal in the IRGAs. Pressure and temperature in each IRGA sample volume were also measured with external sensors (Mensor CPT6100 and a thermocouple, respectively). An inertial motion unit (IMU – Systron Donner MotionPak II) provided high frequency acceleration and rate data, and a GPS compass and the ship’s gyrocompass were used to completely describe the ship’s motion. These data allowed the wind speed measurements from the Cs3 to be corrected for platform motion following *Miller et al.* (2008). All measurements were performed at 10 Hz.

5.2.1 Data analysis and flux calculations

The fluxes of momentum u_* and the sonic sensible heat H_{sonic} were calculated from the Csat3 data after motion correction (*Miller et al.*, 2008) and rotation of the wind vector into the mean flow (*McMillen*, 1988). The latent heat flux Q_{lat} was calculated from the covariance of the vertical wind speed w with the water vapour mixing ratio x_v from *wetA* and *wetB* after correction for the time delay. H_{sonic} was corrected with the latent heat flux to derive the sensible heat flux H_s , following (*Burns et al.*, 2012). The measured CO₂ density was converted to a mixing ratio (as described in Sect. 5.1) and ship motion contaminations of the signal due to flexing of the sensor or inertial forces on the filter wheel were removed using a linear regression with the acceleration and rate signal (as in *Miller et al.*, 2010).

All flux calculations were performed over 25 min intervals. These intervals were divided into five 5 min sub-intervals and were excluded if any of the mean wind direction within the sub-intervals exceeded $\pm 100^\circ$ to the bow to minimise flow distortion effects. Flux intervals were also excluded when spikes were present in the wind speed or IRGA measurements. The remaining intervals were checked for signs of non-stationarity in the CO₂ co-spectra of the *dryA* and *dryB*, and the same criteria as in *Bell et al.* (2013) were applied. It has to be noted here, that the co-spectra of CO₂ and H₂O are similar. Therefore a cross-contamination of the CO₂ signal with H₂O cannot be clearly identified by spectral analysis. A total of 327 from the 1039 available intervals passed the quality control for *dryA* as well as for *dryB* and were used for the analysis presented here. For *wetA* and *wetB*, only 273 and 269 intervals, respectively, passed because these analysers had been removed from the setup for about one day. Flux measurements from *wetA*

and *wetB* passed both for 267 intervals, because spikes had compromised the data from the two sensors during different intervals.

The PKT correction, as presented by *Prytherch et al.* (2010a), was applied to the mixing ratios measured by the two analysers *wetA* and *wetB*. This method includes an iteration in which the correct flux value is approximated. The termination criteria for the iteration was chosen according to *Prytherch et al.* (2010a), to be $|F_c^{(j)} - F_c^{(j-1)}| \leq 0.04 \text{ mol m}^{-2} \text{ yr}^{-1}$. *Prytherch et al.* (2010a) also suggested a rejection of the PKT results if the iteration did not converge within 10 steps or if $F_c^{(j)}$ exceeded $\pm 400 \text{ mol m}^{-2} \text{ yr}^{-1}$ (which was considered unrealistically high). Thus the application of the PKT correction to the measurements from the un-dried IRGA lead to a further reduction of the data set. For *wetA*, the PKT correction rejected 102 of the 273 intervals and for *wetB* 89 of 269, respectively. Flux measurements and PKT results passed for both sensors for 161 of the intervals. The fluxes calculated from measured x_{cm} and the PKT-corrected x_{PKT} were evaluated against the unbiased measurements of the dried IRGAs.

5.3 Results

Figure 5.2 shows an overview of the conditions encountered during the SOAP experiment from 16 February to 5 March 2012 (doy 47–65). The wind speed range was between 0–15 m s^{-1} (25 min average) and peaked at 20 m s^{-1} on doy 61. Unfortunately, the uninterruptible power supply of the EC system was flooded during this storm event, leading to a 12 h gap in the record. The ship was steered into the wind as much as possible, except during survey

periods or deployments of instruments.

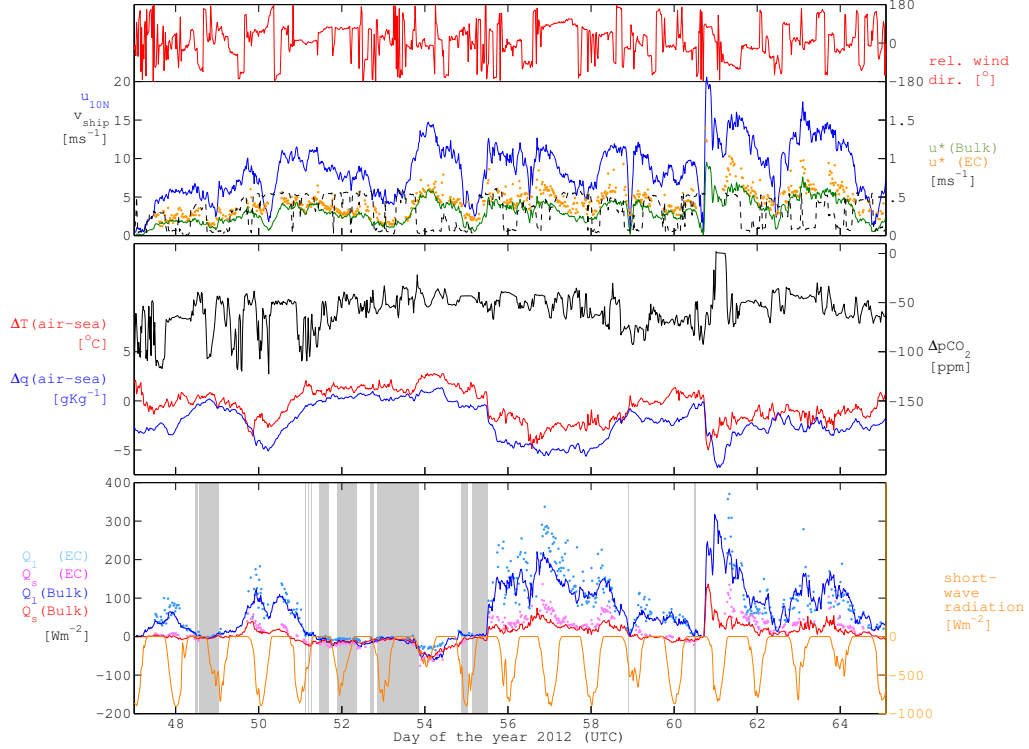


Figure 5.2: Overview of conditions encountered during the SOAP experiment. Shaded areas mark low latent heat fluxes ($Q_{\text{lat}} \leq 7 \text{ W m}^{-2}$). The wind speed measurement was taken on the ship’s main deck and is corrected for air-flow-distortion (Popinet *et al.*, 2004) and normalised to standard conditions (10 m height and neutral stability). This wind speed was used to calculate the bulk fluxes with the TOGA COARE 3.0 algorithm. All direct EC fluxes are measured at the bow mast using the Csat3 sonic anemometer and the IRGA in the science container on the fore-deck.

The air temperature was mostly colder than the water temperature (measured by the ship’s thermosalinograph) except for a period between day 51 and 55, when a warm air mass led to negative turbulent heat fluxes. The air-water $p\text{CO}_2$ difference ranged between $-40 \mu\text{atm}$ and $-120 \mu\text{atm}$. These large $\Delta p\text{CO}_2$ values were easily within the $40 \mu\text{atm}$ criterion for EC flux measurements with the LICOR IRGAs (Rowe *et al.*, 2011).

5.3.1 Primary CO₂ flux results

The CO₂ flux measurements from the four CP IRGAs (without PKT correction) are plotted in Fig. 5.3 (top and middle). The CO₂ flux estimates from the dry gas analysers were in general agreement with each other and *Sweeney et al.* (2007), which is an updated version of the widely-used parameterisation from *Wanninkhof* (1992), while the flux measurements from the un-dried gas analysers exhibited large scatter.

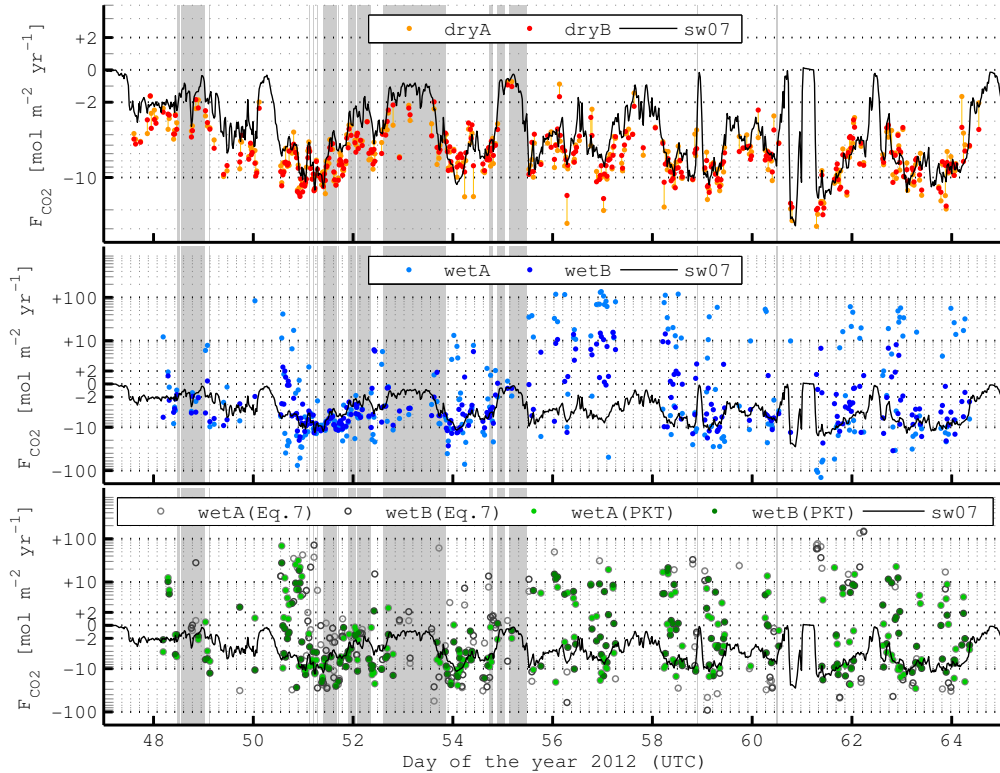


Figure 5.3: Time series of the direct CO₂ fluxes and the flux calculated with the parameterisation of *Sweeney et al.* (2007), plotted on logarithmic scale with sign. Values between $\pm 2 \text{ mol m}^{-2} \text{ yr}^{-1}$ are plotted on linear scale. Shaded areas mark low latent heat fluxes ($Q_{\text{lat}} \leq 7 \text{ W m}^{-2}$). Top: fluxes from *dryA* and *dryB* parallel measurements are linked with vertical lines; middle: fluxes from *wetA* and *wetB*; bottom: fluxes from *wetA* and *wetB* after the PKT correction has been applied to the CO₂ measurements and the results from Eq. (5.11), which are overlaid with the PKT results.

The LICOR IRGAs measure CO₂ density and the measured flux signal F_{IRGA} must be corrected for the air-density flux bias terms (F_q , F_T , and F_P) to obtain the correct CO₂ flux signal F_c . The flux bias terms at different measurement positions are shown in Fig. 5.4. For the un-dried IRGA F_q

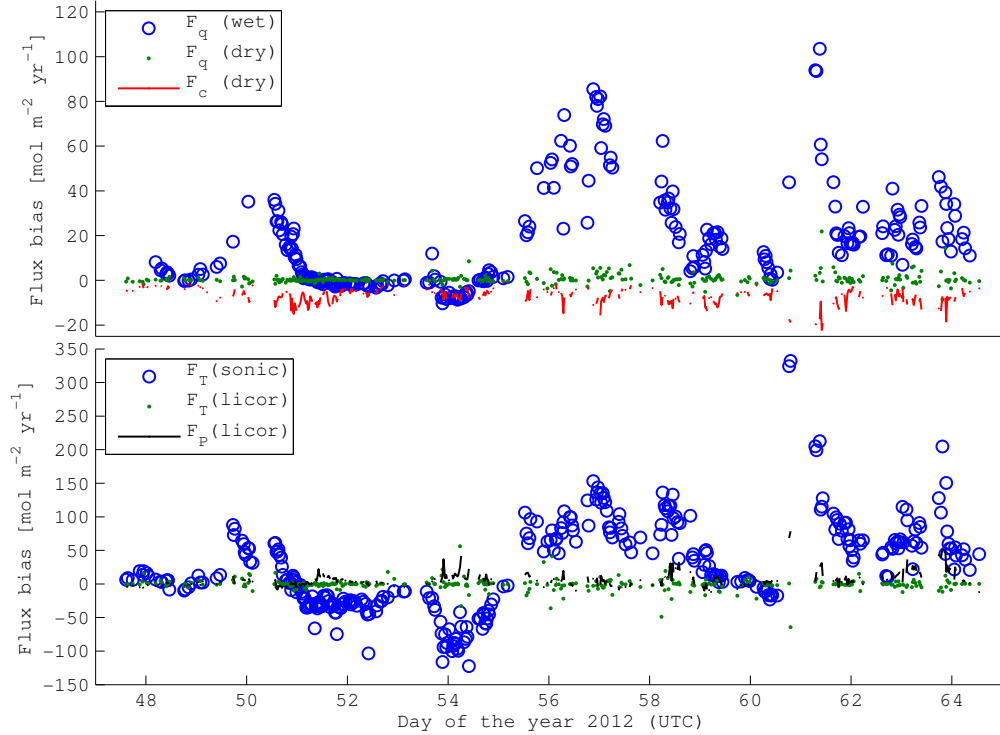


Figure 5.4: Time series of the bias fluxes in Eq. 5.3, caused by air density fluctuations (*Webb et al.*, 1980). Top: Bias flux caused by humidity fluctuations F_q upstream of the dryer *wet* and downstream *dry* and the CO₂ flux F_c as measured by the IRGA *dry* (there are only small differences between *A* and *B*). Bottom: Bias flux caused by temperature fluctuations F_T as measured by the bow mast sonic and as measured by the CP-IRGAs, and the bias flux caused by pressure fluctuations F_P .

exceeded F_c by an order of magnitude (Fig. 5.4 top). For the whole data set, the average magnitude of the latent heat flux from the un-dried IRGAs was 36 W m^{-2} , in contrast the average magnitude of the latent heat flux downstream of the dryer was 2.4 W m^{-2} . The application of the diffusion dryer therefore reduced F_q in average by 93%. This is comparable to (*Miller*

et al., 2010), who found a reduction by 97%. A similar effective reduction was found for F_T (Fig. 5.4 bottom), when compared with the open-path measurement by the sonic anemometer. The reduction of F_T is due to heat exchange of the sample air with the 20 m long inlet tubing and does not depend upon the drying. F_P (Fig. 5.4 bottom) is much smaller than F_q and F_T , but of the same magnitude as F_c . F_P cannot be reduced physically and needs to be measured accurately (*Miller et al.*, 2010).

The flux measurement of all four CP-IRGAs, as presented in Fig. 5.3, have been corrected for the air-density bias fluxes by calculating the CO₂ mixing ratio. However, even after this correction was applied, the un-dried IRGA CO₂ fluxes showed erratic behaviour. The difference in the CO₂ flux measurements from the un-dried and dried IRGAs is plotted in Fig. 5.5. The variance of the flux data from *wetA* and *wetB* increased proportionally with the latent heat flux and became an order of magnitude larger than that from *dryA* or *dryB*. There was no apparent correlation between the differences in the CO₂ fluxes ΔF and the bias fluxes caused by the pressure and temperature fluctuations (F_T , and F_P).

It has to be pointed out that the primary flux measurements from the two un-dried sensors agreed with the measurements from the dried IRGAs during periods with very low latent heat flux ($Q_{\text{lat}} \leq 7 \text{ W m}^{-2}$). These periods are marked as shaded areas in Figs. 5.2 and 5.3. The limit of 7 W m^{-2} was chosen so that the envelope of the bias was approximately two times the scatter observed at $Q_{\text{lat}} \approx 0 \text{ W m}^{-2}$. Figure 5.6 shows scatter plots of the flux measurements from *wetA* and *wetB* against those from *dryB* for ($Q_{\text{lat}} \leq 7 \text{ W m}^{-2}$) and of *dryA* against *dryB* for the whole data set. A linear regression of the *dryA* vs. *dryB* for the full dataset gave a slope of (1.09 ± 0.01) with a $R^2 = 0.96$. For *wetA* and *wetB* regression was performed

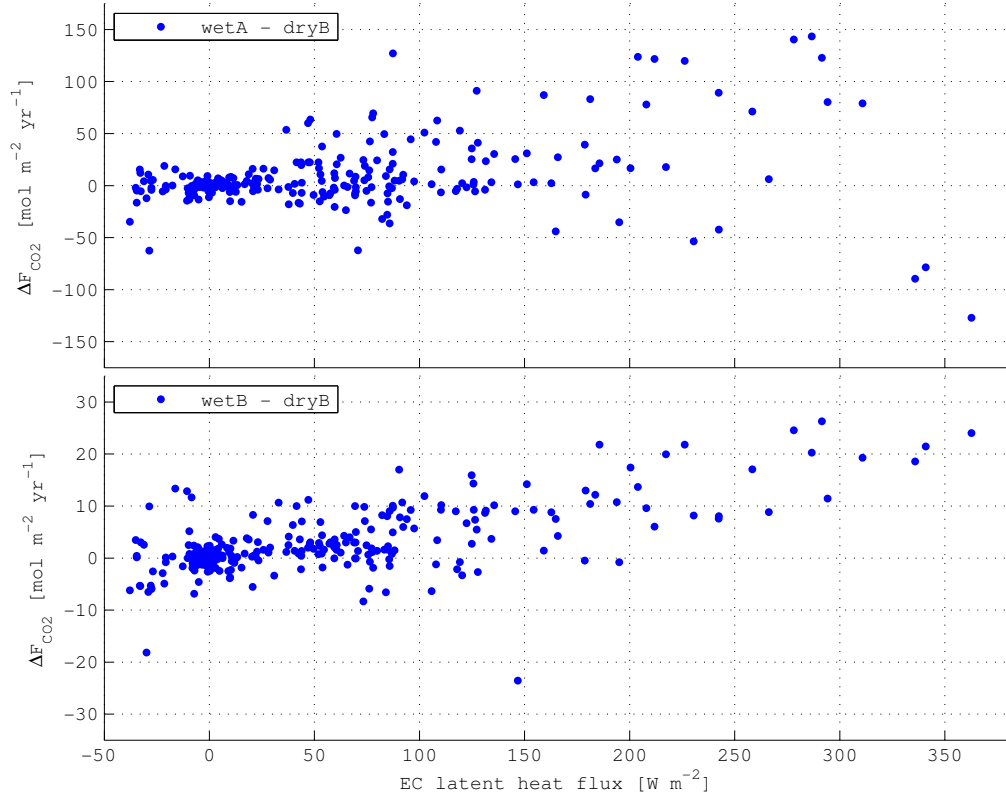


Figure 5.5: Difference between the CO₂ flux calculated from the measured signals x_{cm} from the un-dried gas analysers to the flux from *dryB* as a function of the EC latent heat flux measurement from the un-dried gas analysers. Different scales are used for the two sub-plots.

over the restricted data set ($Q_{\text{lat}} \leq 7 \text{ W m}^{-2}$) and gave slopes of (0.88 ± 0.15) with $R^2 = 0.36$ and (0.93 ± 0.06) with $R^2 = 0.78$, respectively.

Figures 5.7 and 5.8 (left side) show scatter plots of the primary flux measurements of *wetA* and *wetB* against *dryB* for the full data set. The magnitude of the latent heat flux is used as colour code. Linear regression gave a slope of (-0.17 ± 0.8) for *wetA* vs. *dryB* and $(+0.7 \pm 0.2)$ for *wetB* vs. *dryB*, respectively, both with very low R^2 values. On average, the effect of the bias was to reduce the CO₂ flux, even changing the sign.

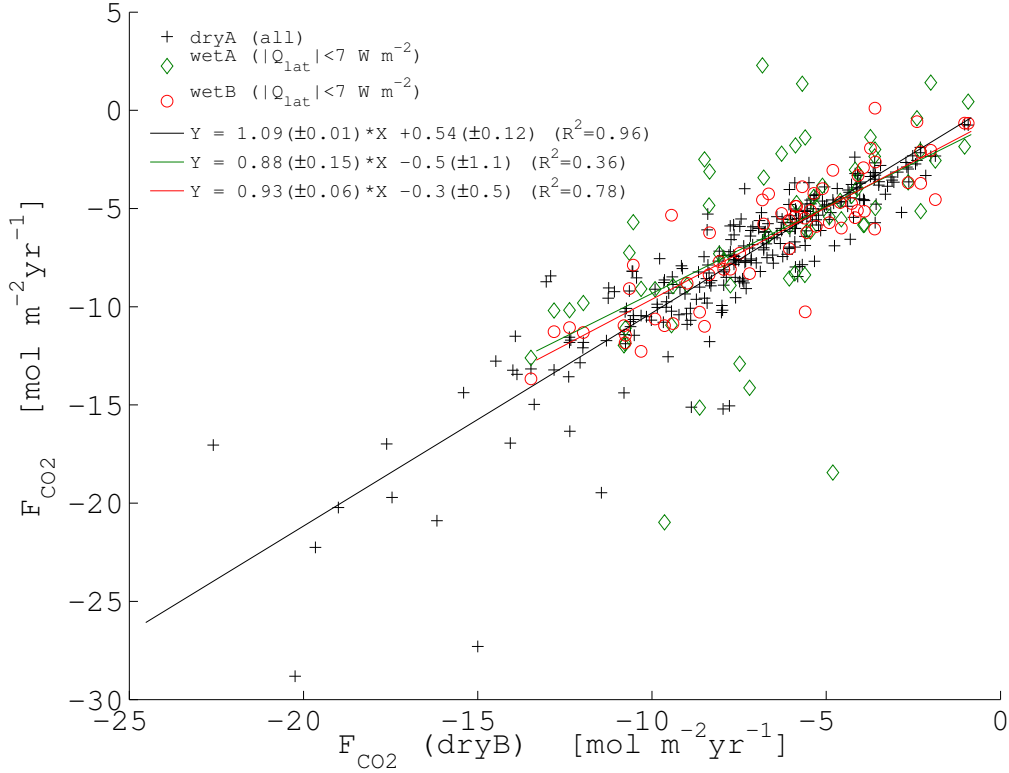


Figure 5.6: Scatter plot of the CO₂ flux measurements (without PKT correction) from *wetA*, *wetB* and *dryA* against those from *dryB*. For *wetA* and *wetB*, only measurements with $Q_{\text{lat}} \leq 7 \text{ W m}^{-2}$ are used. Linear fit coefficients with standard deviation and the R^2 value are shown in the legend.

5.3.2 Application of the PKT Correction

The PKT correction, as presented by (Prytherch *et al.*, 2010a), was applied to the x_{cm} measured by the two un-dried analysers and the results were evaluated against the unbiased measurements of the dried IRGAs. Figure 5.3 (bottom) shows the PKT-corrected fluxes (F_c^{PKT}) as well as the results from Eq. (5.11), which is derived in Sect. 5.4 and presents a simplified version of the PKT correction that also provides an output when the PKT correction does not converge. The results of Eq. (5.11) are not used in the evaluation of the PKT correction results, i.e. intervals that were rejected by the PKT correction are excluded from the analysis.

Scatter plots in Figs. 5.7 and 5.8 show the correlation between the flux measurements from the un-dried IRGAs and the fluxes from *dryB* before (left) and after the application of the PKT correction to the un-dried measurements (right). For low latent heat flux, the PKT correction increases the scatter of

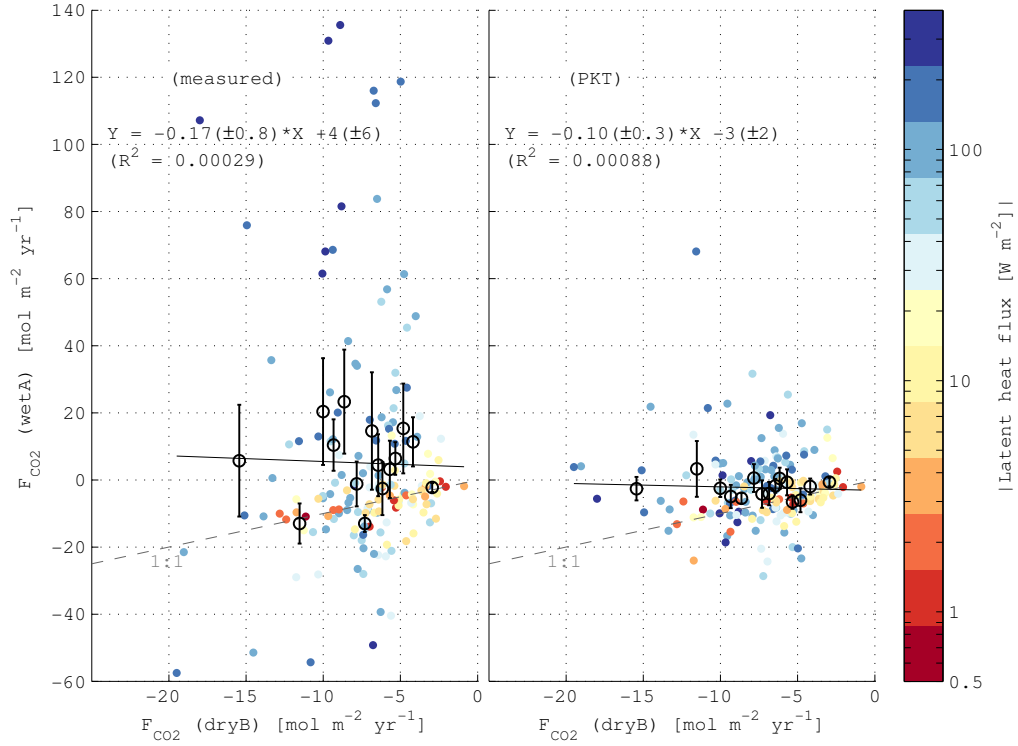


Figure 5.7: Scatter plot of the CO₂ flux measurements from *wetA* against those from *dryB* before (left) and after the PKT correction was applied to the *wetA* measurements (right). Bin averages of 15 bins with an equal number of data points are shown as black circles, with error bars indicating the standard deviation from the bin average. A linear regression to the data is shown as a solid black line and the 1 : 1 agreement is indicated with a grey dashed line. Only intervals for which the PKT correction provided a result for both, *wetA* and *wetB*, were used for this plot.

the initially well-correlated measurements and also rejects a large part of the results. For *wetA*, the PKT correction reduces the large range of scatter, but does not improve the correlation with the *dryB* fluxes. For *wetB*, which shows a weaker bias, the PKT correction even reduces the correlation with the *dryB* flux estimates from (0.7 ± 0.2) to (0.4 ± 0.2) .

The average raw flux estimates from the four CP IRGAs and with PKT correction for the two un-dried IRGAs are shown in Table 5.2.

Table 5.2: Average CO₂ fluxes in [mol m⁻² yr⁻¹] for the complete experiment, and for subsets (Subset 1 [$-7 \text{ W m}^{-2} \leq Q_{\text{lat}} \leq +7 \text{ W m}^{-2}$]; Subset 2 [$-35 \text{ W m}^{-2} \leq Q_{\text{lat}} \leq -7 \text{ W m}^{-2}$]; Subset 3 [$+7 \text{ W m}^{-2} \leq Q_{\text{lat}} \leq 340 \text{ W m}^{-2}$]) based on the EC latent heat flux measured by the un-dried gas analysers. To make the values comparable, only intervals with results from the PKT loop are used for the calculating the mean flux values.

Interval	all	Subset 1	Subset 2	Subset 3
# intervals	161	28	24	109
$F_{\text{cm}} \text{ dry}A$	-7.21	-6.59	-5.80	-7.69
$F_{\text{cm}} \text{ dry}B$	-7.16	-6.51	-5.63	-7.66
$F_{\text{cm}} \text{ wet}A$	+5.01	-6.50	-7.67	+10.76
$F_{\text{cm}} \text{ wet}B$	-3.29	-5.96	-6.62	-1.87
$F_{\text{PKT}} \text{ wet}A$	-2.34	-5.89	-8.97	+0.03
$F_{\text{PKT}} \text{ wet}B$	-3.09	-6.67	-7.94	-1.10

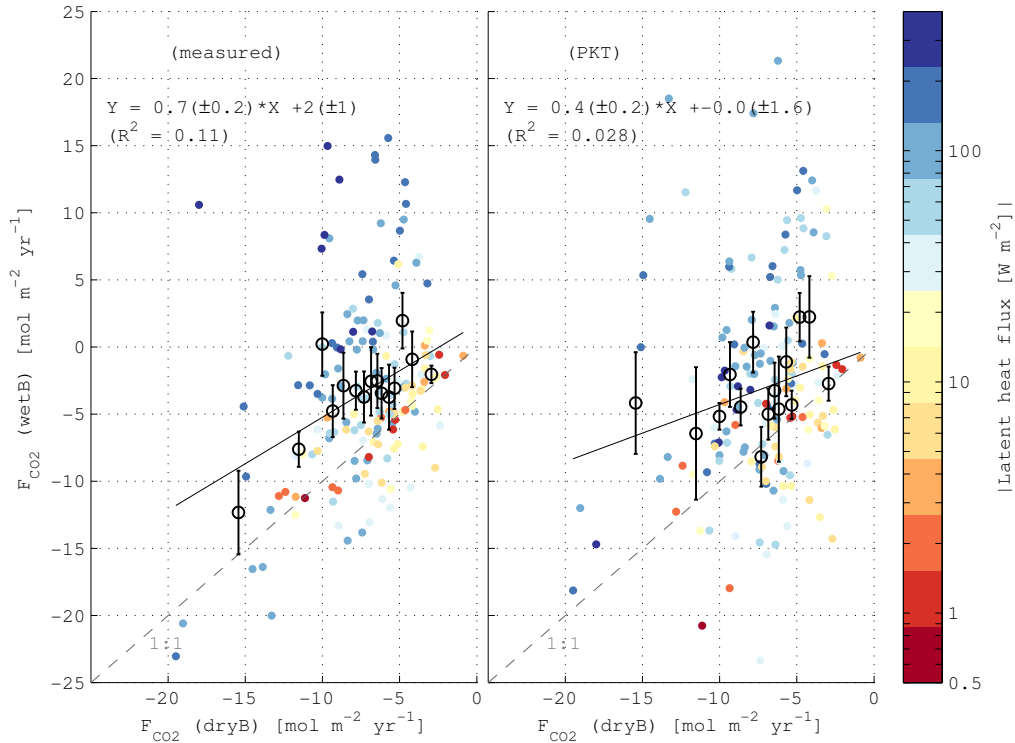


Figure 5.8: Same as Fig. 5.7, but for *wetB*.

The average was taken over the 161 intervals, where PKT results were available for both un-dried gas analyser, and over three subsets, which were based on the magnitude and sign of the latent heat flux measured by the un-dried IRGAs. For the whole cruise, the PKT correction brought the flux measurements from *wetA* and *wetB* into closer agreement. The mean estimate of *wetA* and *wetB* after PKT did, however, underestimate the flux ($\overline{F_c} = -7.19 \text{ mol m}^{-2} \text{ yr}^{-1}$) by 62%. For Subset 1, ($[-7 \text{ W m}^{-2} \leq Q_{\text{lat}} \leq +7 \text{ W m}^{-2}]$) the bias in the un-dried IRGA was negligible and the flux estimates of all four sensors agreed within 10%. Here PKT correction changed the results by less than 12%. For Subset 2 with moderately negative latent heat fluxes ($[-35 \text{ W m}^{-2} \leq Q_{\text{lat}} \leq -7 \text{ W m}^{-2}]$), the PKT correction increased the bias in the flux measurements from 25% to 48%. Subset 3 included the largest latent heat fluxes ($[+7 \text{ W m}^{-2} \leq Q_{\text{lat}} \leq 340 \text{ W m}^{-2}]$); here, the PKT-corrected fluxes are only small fractions of the dried fluxes i.e. $\leq 1\%$ and 14% for *wetA* and *wetB*, respectively. The average flux estimates of the two dried IRGAs agreed within 1% for the whole cruise and for each of the subsets 1 and 3. For subset 2 the agreement was within 3%.

5.3.3 Application of the Spectral Correction

Here we test the spectral cross-sensitivity correction (*Edson et al.*, 2011) on its ability to estimate the humidity flux bias in the *wet* CO₂ flux measurements. Figures 5.9 and 5.10 show scatter plots of the correction factor $\mu(\Gamma = 1)\langle x_v w \rangle$ assuming $\Gamma = 1$ over (i) the CO₂ flux bias that was estimated by the PKT correction (panel a), and (ii) the bias with respect to the *dry* flux measurements (panel b). The measurements are scaled with the average CO₂ flux of $|\langle x_c w \rangle| = -7 \text{ mol m}^{-2} \text{ yr}^{-1}$. This emphasises that the

observed flux biases are in the order of 1000%.

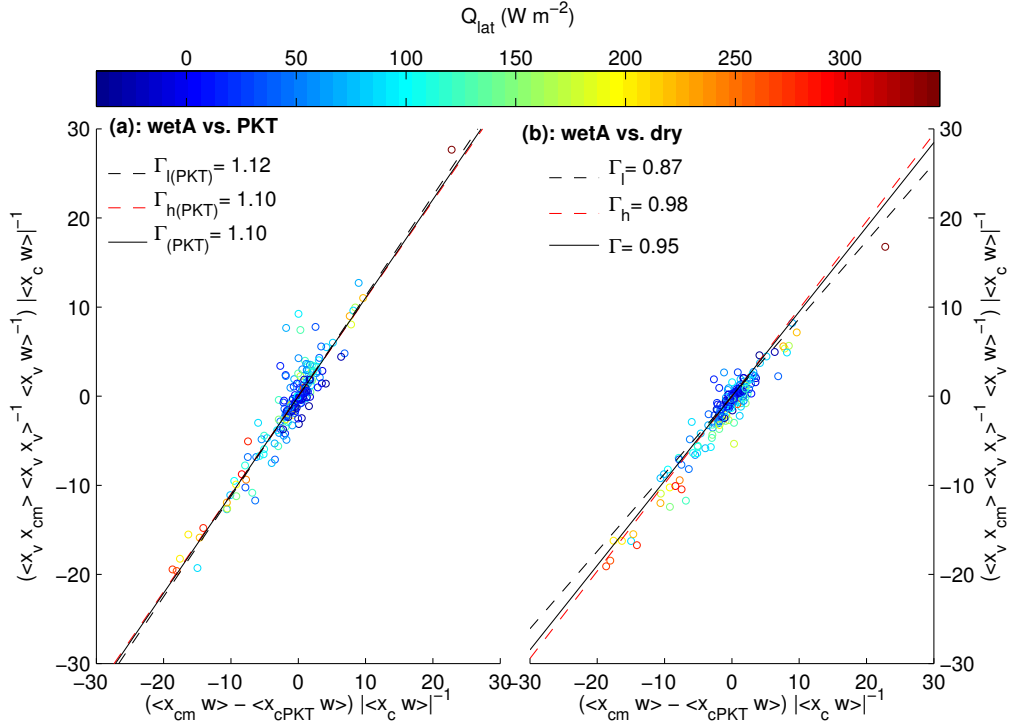
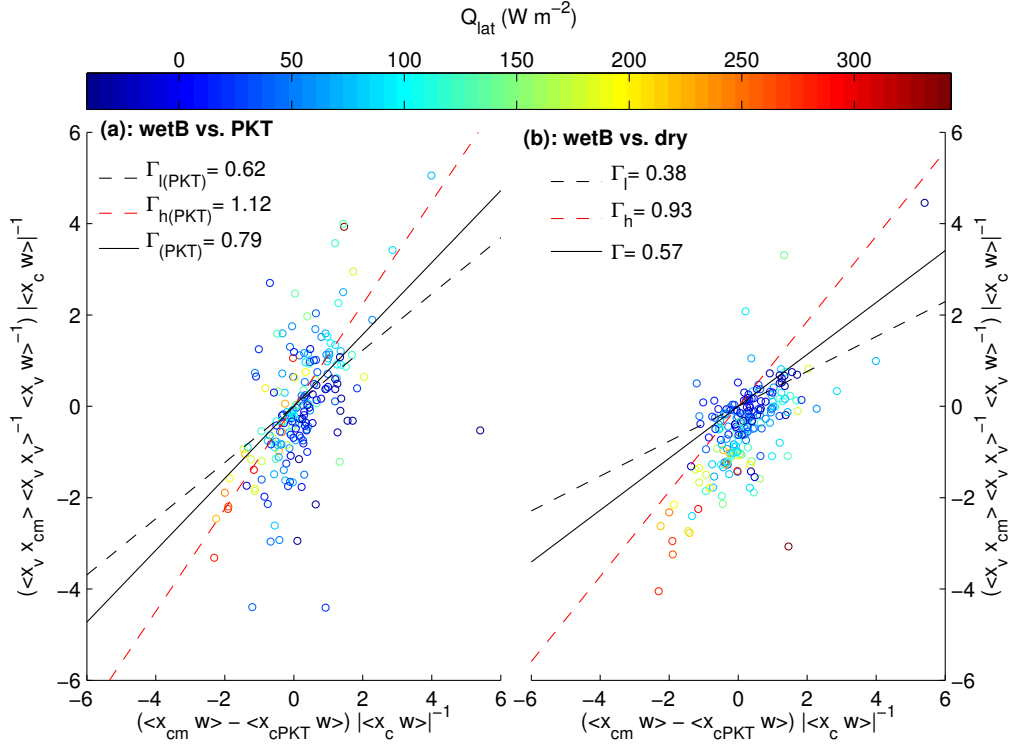


Figure 5.9: Panel a: Correction factor, $\mu\langle x_v w \rangle$ for $\Gamma = 1$, for IRGA *wetA* plotted as function of the bias estimated by the PKT correction. Both axes are weighted with the cruise average CO₂ flux ($-7.2 \text{ mol m}^{-2} \text{ yr}^{-1}$), which was measured by the IRGA *dry*. The correction factor Γ is estimated as linear fit with the y-intercept forced to zero, for latent heat fluxes below, and above 100 W m^{-2} , and for the whole data set Γ_{l} , Γ_{h} , and Γ respectively. Panel b: same, but the bias to the CO₂ fluxes measured on dry air is used as x-axis. The latent heat flux measured by the IRGA *wet* is used as color code for both panels.

From these plots, the factor Γ can be estimated by a linear fit (when the intercept is forced to zero). Γ values are given for the whole data set, and for two subsets with $7 \text{ Wm}^{-2} < |Q_{\text{lat}}| < 100 \text{ Wm}^{-2}$ and $|Q_{\text{lat}}| > 100 \text{ Wm}^{-2}$. A correlation between the correction term $\mu(\Gamma = \text{const})\langle x_v w \rangle$ is given for both gas analysers. However the residuals of the linear fits to the measurements are all of the order of $|\langle x_c w \rangle|$, and the estimates of Γ depend on the selected subset of data.


 Figure 5.10: Same as Fig. 5.9 but for the IRGA *wetB*.

5.3.4 Humidity Bias and Transfer Velocities

The main purpose of the direct CO₂ flux measurements is the determination of the gas transfer velocity and its dependency on environmental parameters such as wind speed. Here we study the effect of the usage of the PKT correction on the transfer velocity estimates. Figure 5.11 shows scatter plots of k_{660} measured with the *wet* and *dry* IRGA and after PKT-correcting the *wet* flux measurements. The k_{660} from the *dry* measurements are higher than (Sweeney *et al.*, 2007) and show a rather linear increase with u_{10N} , i.e., they remain clearly below the relation $k_{660}(u_{10N})$, which is given by the cubic parametrisation from (Wanninkhof and McGillis, 1999). For the *wet* measurements, the magnitude of k_{660} increases much faster with increasing wind speed, but the large fraction of (*un-physical*) negative transfer velocities

leads to an on average low transfer velocity that weakly correlates with wind speed. The scatter is one order of magnitude larger than for the *dry* k_{660} . In this study the PKT correction reduces the scatter significantly, but leads to biased low transfer velocities when compared to the *dry* k_{660} . If the largest negative values were removed from the data set, both measured *wet* and PKT-corrected k_{660} would support cubic or higher relationships with wind speed.

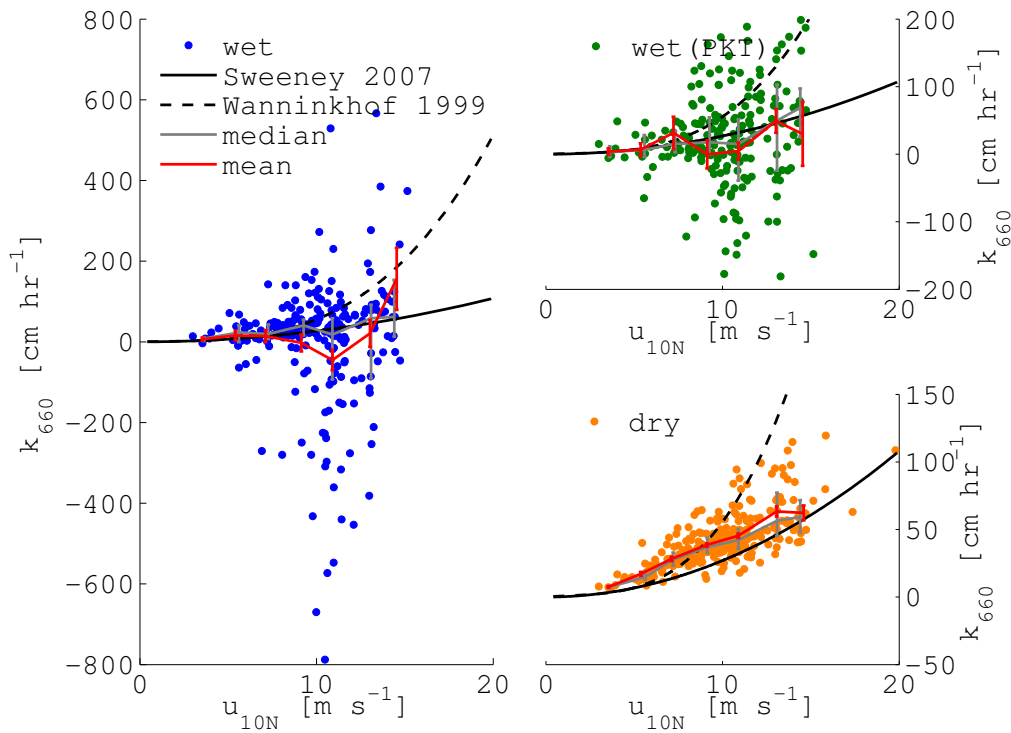


Figure 5.11: Normalised transfer velocities calculated using the preliminary flux results from the *wet* and *dry* IRGA (left and bottom right, respectively) and after application of the PKT correction (top right) plotted as functions of the normalised wind speed u_{10N} . Shown are individual 25 min measurements and wind speed-bin averages (mean in red) and (median in grey). The quadratic and cubic parametrisations from *Sweeney et al.* (2007) and *Wanninkhof and McGillis* (1999), respectively are shown as black lines.

5.4 Analysis of the PKT correction

To investigate the unsatisfactory results of the PKT correction (cp. Sect. 5.3.2), we will now analyse the correction algorithm in detail.

The PKT method *Prytherch et al.* (2010a) is based on the assumption that the ratio of the variations of two quantities, e.g., CO₂ and relative humidity, is equal to the ratio of their vertical fluxes:

$$\frac{\partial \langle x_c \rangle}{\partial \langle \text{RH} \rangle} = \frac{\langle x'_c w' \rangle}{\langle \text{RH}' w' \rangle} \quad (5.8)$$

Prytherch et al. (2010a) derived Eq. (5.8) from the Monin–Obhukov similarity theory, assuming that the scalar profiles of the two non-dimensionalised quantities are equal.

The correction algorithm can be summarised as follows: first, the variations of x_c that are dependent on RH are removed from the measured signal x_{cm} with a 3rd order polynomial fit to the x_{cm} and RH time series:

$$x_c^{(0)} = x_{\text{cm}} - \sum_{n=1:3} a_n (\text{RH})^n \quad (5.9)$$

where a_n are the polynomial coefficients determined by the fit. A first-step CO₂ flux $F_c^{(0)}$ is calculated from the detrended signal $x_c^{(0)}$, and then used with Eq. (5.8) to get a first approximation of $\frac{\partial \langle x_c \rangle}{\partial \langle \text{RH} \rangle}$. The CO₂ mixing ratio is then adjusted using this quantity:

$$x_c^{(\text{new})} = x_c^{(0)} + 0.5 \cdot (\text{RH}') \cdot \frac{F_c^{(0)}}{\langle x'_v w' \rangle} \frac{\partial \langle x_v \rangle}{\partial \langle \text{RH} \rangle} \quad (5.10)$$

Here, the relative humidity flux $\langle \text{RH}' w' \rangle$ was substituted with $\langle x'_v w' \rangle \left(\frac{\partial \langle x_v \rangle}{\partial \langle \text{RH} \rangle} \right)^{-1}$,

similar to Eq. (5.8). The adjusted time series $x_c^{(\text{new})}$ is now used to calculate an approximation of the CO₂ flux, and produce a new correction term via Eq. (5.8) to be used in Eq. (5.10). Equations (5.8) and (5.10) are then looped until the CO₂ flux estimate converges to a flux value F_c^{PKT} (this loop typically converges within less than 10 steps). Equations (5.8–5.10) are taken from the Matlab code in the supplementary material of *Prytherch et al.* (2010a).

We found that the loop can be replaced by one simple equation:

$$F_c^{\text{PKT}} = F_c^{(0)} \cdot \beta \quad (5.11)$$

where $\beta = \left(1 - 0.5 \frac{\langle \text{RH}' w' \rangle}{\langle x_v' w' \rangle} \frac{\partial \langle x_v \rangle}{\partial \langle \text{RH} \rangle}\right)^{-1}$. From Eq. (5.8) it follows that $\beta \approx 2$.

In order to show this, we re-write Eq. (5.10) by replacing the adjusted mixing ratio $x_c^{(\text{new})}$ with $x_c^{(j)}$ and $F_c^{(0)}$ with the flux from the previous iteration step $F_c^{(j-1)}$:

$$x_c^{(j)} = x_c^{(0)} + 0.5 \cdot (\text{RH}') \cdot \frac{F_c^{(j-1)}}{\langle x_v' w' \rangle} \frac{\partial \langle x_v \rangle}{\partial \langle \text{RH} \rangle} \quad (5.12)$$

Equation (5.12) is iterated within the PKT loop. The new flux estimate of iteration j (i.e. $F_c^{(j)}$) is computed from $x_c^{(j)}$ as follows:

$$F_c^{(j)} = F_c^{(0)} + 0.5 \cdot \langle \text{RH}' w' \rangle \cdot \frac{F_c^{(j-1)}}{\langle x_v' w' \rangle} \frac{\partial \langle x_v \rangle}{\partial \langle \text{RH} \rangle} \quad (5.13)$$

and is used to compute $x_c^{(j+1)}$ via Eq. (5.12). However, if Eq. (5.13) is inserted into the convergence criterion ($F_c^{(j)} - F_c^{(j-1)} \rightarrow 0$) and solved for $F_c^{(j-1)}$, we find that the loop will terminate at F_c^{PKT} given by Eq. (5.11). The results of the loop agree with Eq. (5.11) within the tolerance $|F_c^{(j)} - F_c^{(j-1)}| \leq 0.04 \text{ mol m}^{-2} \text{ yr}^{-1}$, which is used by *Prytherch et al.* (2010a) to determine

that the loop has converged. In Fig. 5.12 the results from Eq. (5.11) and the PKT loop are plotted over the 1:1 correspondence line. A significant advantage of Eq. (5.11) is that it always provides a result whereas the PKT loop does not always converge. In Fig. 5.3 (bottom) the results of Eq. (5.11) are overlaid with F_c^{PKT} . The rejection criteria in the PKT correction algorithm lead to a reduced range of scatter in the PKT results when compared to the results of Eq. (5.11).

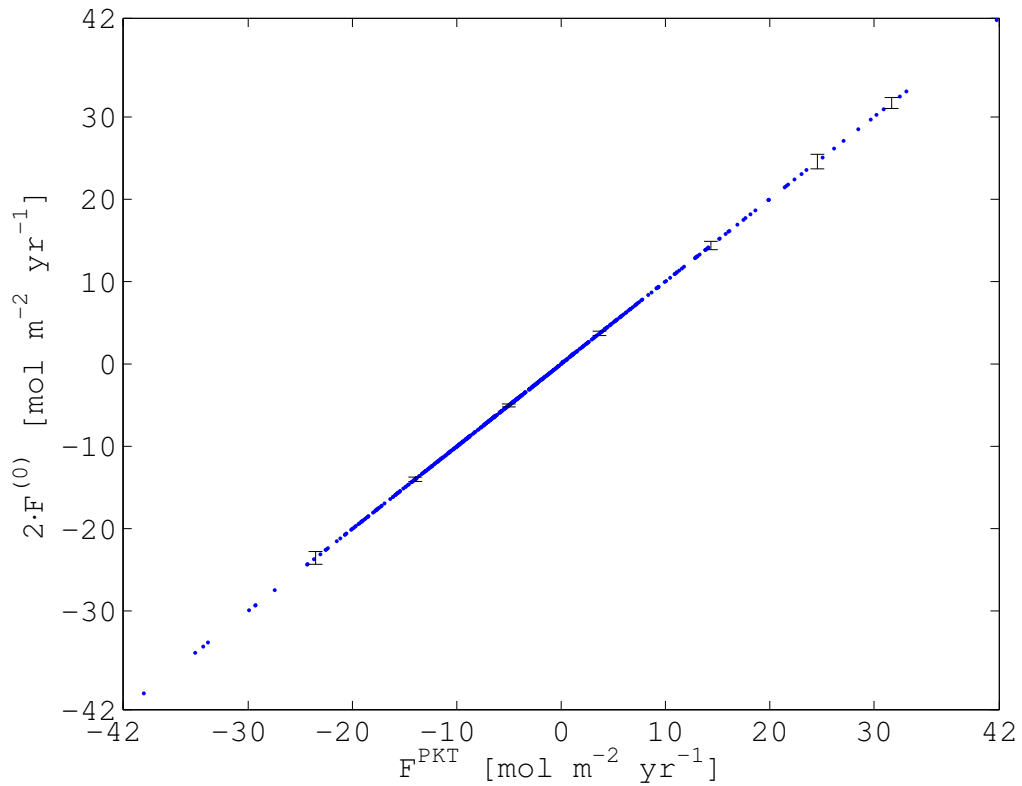


Figure 5.12: Scatter plot of the results from Eq. (5.11) against the results of the PKT correction for IRGA wetB, individual (blue) and binned (black).

Prytherch et al. (2010a) validated the PKT method by applying it to the sensible heat flux (F_{T_s}) as calculated from the measured speed of sound temperature (T_{sonic}). We followed this analysis and show our results in Fig. 5.13, which can be directly compared to Fig. 2 in (*Prytherch et al.*, 2010a). The average of the flux, calculated from the detrended sonic temperature

$(F_{T_s}^{(0)})$, yields approximately one half of the flux signal. The PKT flux, which is equal to the product of the detrended flux and β , correlates with the standard EC sensible heat flux. The factor 0.5 in Eq. (5.11) comes from the same factor Eq. (5.10), which was originally inserted to reduce the step width and improve the convergence of the iteration and was not expected to change the result of the PKT correction (J. Prytherch, review comments). In order to illustrate the influence of this factor, the results of a PKT correction with a factor of 0.75 are shown in Fig. 5.13. Here $\beta \approx 4$ and the PKT results are $(\approx 4 \times F_{T_s}^{(0)})$ and $(\approx 2 \times Q_{\text{sen}})$.

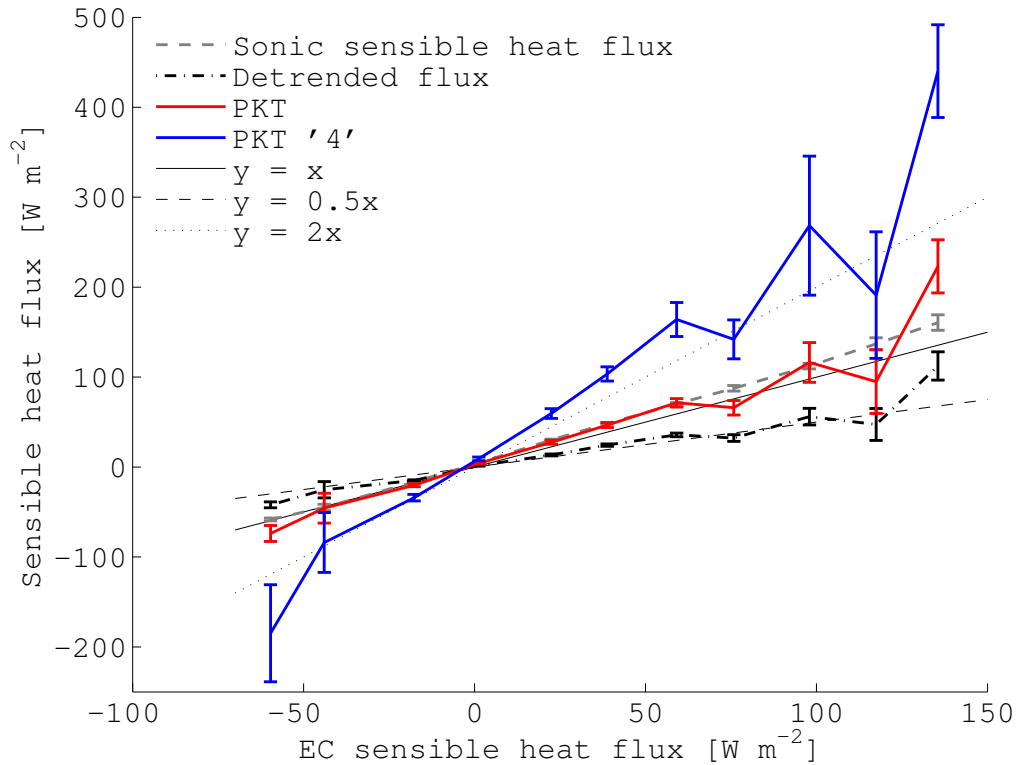


Figure 5.13: Bin-averaged heat fluxes plotted against the standard EC sensible heat flux results (to be compared with Fig. 2 in *Prytherch et al.*, 2010a): “sonic flux” calculated from T_{sonic} (light grey - -); flux after detrending against humidity (black -.); “PKT-corrected” flux (red -); results of a PKT correction with step width 0.75 and $\beta \approx 4$ (“PKT 4”) (blue -). Error bars show standard deviation from the mean. 1 : 1, 1 : 2 and 2 : 1 agreement are indicated.

5.5 Discussion

5.5.1 Humidity Bias - Correcting versus Drying

The good agreement between the dried and un-dried CP systems for low latent heat fluxes (cp. Sect. 5.3.1) supports the findings of *Miller et al.* (2010) that application of a diffusion dryer does not alter the CO₂ flux signal, but avoids contamination of the sensor optics and significantly reduces the magnitude of the necessary air density correction.

The magnitude of the scatter in the CO₂ fluxes from the un-dried CP systems increases with the latent heat flux (Fig. 5.5). These results are similar to results reported for OP IRGAs (LICOR-7500) (e.g. *Kondo and Osamu*, 2007; *Lauvset et al.*, 2011; *Prytherch et al.*, 2010b), which showed an overestimation of the CO₂ flux magnitude, when compared to common bulk formulae. In this study, on the other hand, the bias reduced the CO₂ flux on average. *Kondo and Tsukamoto* (2012) simultaneously deployed OP (LICOR-7500) and CP (LICOR-7000) sensors to measure CO₂ fluxes in conditions with low air–sea CO₂ gradient ($12 \mu\text{atm} < \Delta p\text{CO}_2 < 42 \mu\text{atm}$) and large latent heat fluxes ($70 \text{ W m}^{-2} \leq Q_{\text{lat}} \leq 140 \text{ W m}^{-2}$). The EC CO₂ flux estimates from both OP and CP IRGAs were an order of magnitude higher than expected using the *Sweeney et al.* (2007) parameterisation and diverged increasingly for higher latent heat fluxes. We therefore assume that the bias observed in the fluxes from the un-dried CP has the same origin as the biases observed in the OP measurements cited above. Our measurements also indicate that the bias can be different for each individual IRGA unit.

Equation (5.11) explains why the PKT correction produces unsatisfactory

flux results: the PKT-corrected flux is simply a product of the flux signal, which was calculated from the CO₂ mixing ratios after detrending against the relative humidity, and the term $\beta \approx 2$ that depends solely on water vapour and relative humidity fluctuations. The ratio of the detrended fluxes of the two un-dried IRGAs to the CO₂ flux measured by the *dryB* and the factor β are plotted in Fig. 5.14 as a function of the latent heat flux. The parameter β shows a large scatter for low Q_{lat} but converges to 2 for $Q_{\text{lat}} > 50 \text{ Wm}^{-2}$. The ratio of the detrended fluxes to the fluxes measured by the sensor *dryB* ($(F_c^0) \cdot (F_c)^{-1}$) is on average close to 1 when latent heat flux is small, but exhibits large scatter. For $Q_{\text{lat}} > 50 \text{ Wm}^{-2}$ the value of F_c^0 becomes much smaller than F_c ; this leads to the observed underestimation by the PKT-corrected fluxes.

The PKT correction appears to correct the latent heat flux bias in the sonic sensible heat flux, because the flux calculated from the detrended sonic temperature yields on average approximately one half of the flux signal and is then multiplied with $\beta \approx 2$. However, this does not prove that the PKT correction can successfully remove the bias in the measured CO₂ fluxes.

The spectral cross-sensitivity correction *Edson et al.* (2011) was tested on the IRGA *wet* by estimating the factor Γ in (5.7) from (i) the PKT corrected *wet* CO₂ fluxes and (ii) the fluxes from the *dry* IRGA. All gave different results, showing that $\Gamma \neq \text{const}$. In fact, assuming $\Gamma = \text{const}$ means to expect a linear relation between $C_{x_v x_c}(\omega)$ and $C_{x_v x_{cm}}(\omega)$, which in-fact should not be related. The 'true' Γ will however likely be higher for periods with large humidity fluxes and lower for periods with relative large CO₂ fluxes. Therefore, assuming a Γ constant, or even deriving it from PKT-corrected fluxes, will likely create biased wind speed dependencies of k_{660} . Functionalities of $k_{660}(u_{10N})$ that are derived with a constant Γ *Edson*

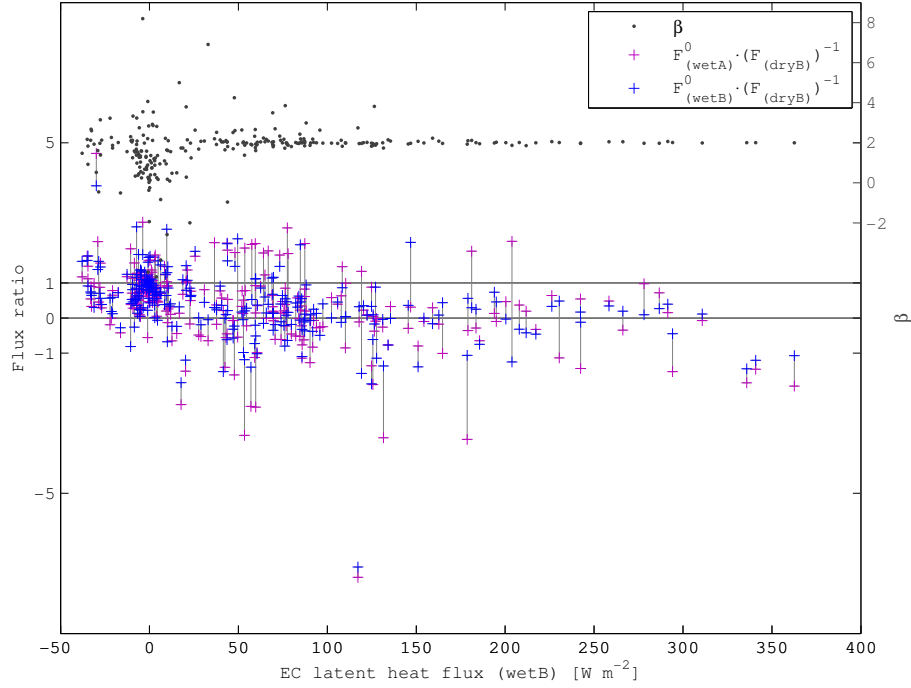


Figure 5.14: Ratio of the detrended CO₂ fluxes F_c^0 from *wetA* and *wetB* as used for the PKT correction to the CO₂ flux calculated from *dryB* (purple +, blue +). Two values of the same sample interval are connected with a grey line; the factor $\beta = \left(1 - 0.5 \frac{\langle RH'w' \rangle}{\langle x'_v w' \rangle} \frac{\partial \langle x_v \rangle}{\partial \langle RH \rangle}\right)^{-1}$ as in Eq. (5.11), calculated from the latent heat flux and relative humidity, as measured by *wetB*, (grey ●).

et al. (e.g. 2011) might therefore not reflect the true relationship.

The idea of a cross correlation coefficient as proposed by *Prytherch et al.* (2010a) and *Edson et al.* (2011) could however be used fruitfully if it can be shown that $\mu(t)$ changes smoothly in time. In this case fast open- and slow dry closed-path measurement could be combined by computing

$$x_c = \overline{x_c(dry)} + x'_{cm}(wet) - \mu_v(t)x'_v(wet) - \mu_T(t)T'(wet) \quad (5.14)$$

were the correlation-coefficients for water vapour and temperature, $\mu(t)_v$ and $\mu(t)_T$ respectively, are derived from $x_{cm}(wet)$ and $x_c(dry)$. The required flow rate for the dry close-path analyser would then depend on the maximum change rate of $\mu(t)_v$ and $\mu(t)_T$.

5.5.2 Air-Flow Distortion

The direct flux measurements in this chapter were computed with wind speeds that had been tilt corrected with the classic DR approach (*Edson et al.*, 1998). In Chapter 4 we pointed out that this can lead to an overestimation of the wind vector pitch (θ) and consequent biased flux estimates. In Fig. 5.15 the estimates of θ_{DR} are plotted as functions of the relative wind direction and colour coded with $v_{\text{ship}}u_{\text{me}}^{-1}$. This shows that θ_{DR} strongly overestimates the true wind vector pitch when the ship is under way.

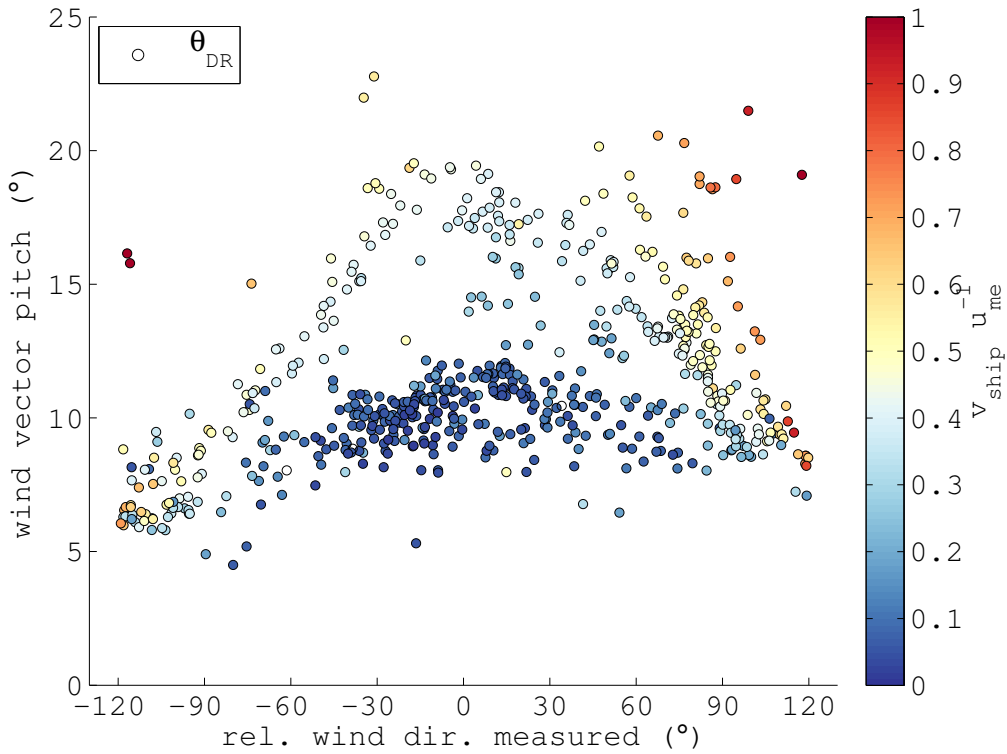


Figure 5.15: Wind vector pitch estimated from the double rotation of u_{true} (θ_{DR}) as function of the relative wind direction and of the ratio $v_{\text{ship}}u_{\text{me}}^{-1}$, which is used as colour code. This figure should be compared with Fig. 4.4.

The effect of this overestimation on k_{660} is presented in Fig. 5.16, where the *dry* transfer velocities from Fig. 5.11 (bottom right) are replotted as a function of u_{10} and the ratio $v_{\text{ship}}u_{\text{me}}^{-1}$. The measurements were separated into

two subsets $v_{\text{ship}}u_{\text{me}}^{-1} \leq 0.1$ (station, 116 measurements) and $v_{\text{ship}}u_{\text{me}}^{-1} > 0.1$ (underway, 160 measurements) and bin averaged over 2 m s⁻¹ wind speed bins. The underway measurements resulted in higher transfer velocities. This is most likely caused by the overestimation of the scalar CO₂ flux due to the overestimated θ_{DR} .

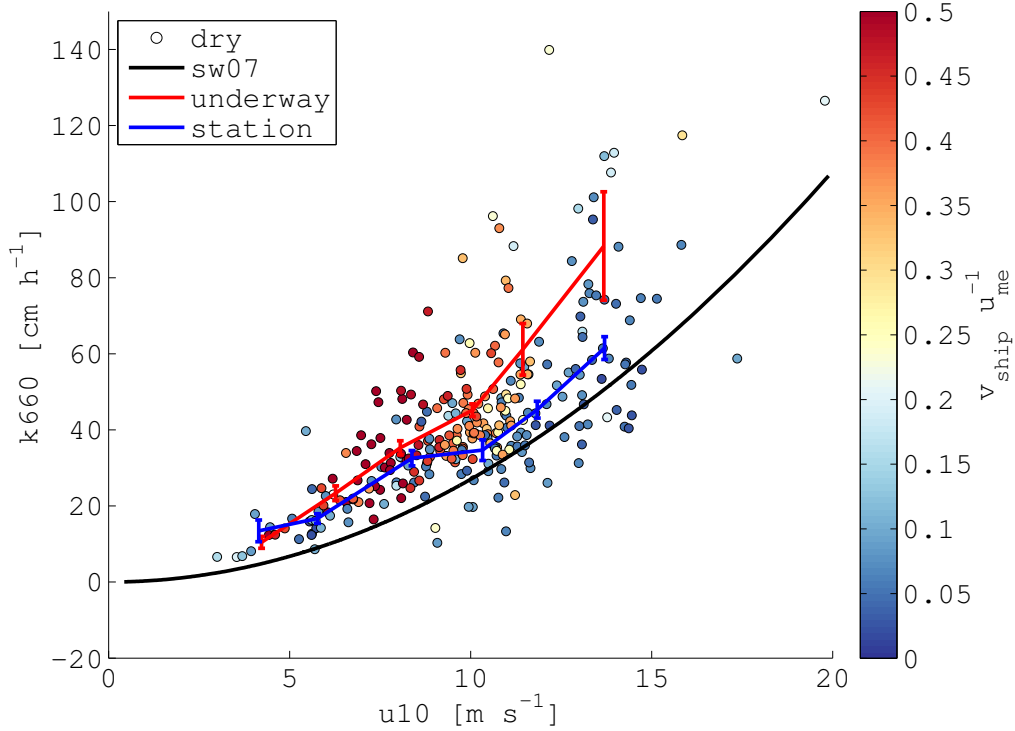


Figure 5.16: Preliminary gas transfer velocity estimates from the *dry* IRGA as a function of u_{10N} using the standard DR method. The colour code shows the ratio of ship speed and measured relative wind speed. The measurements are separated into two subsets $v_{\text{ship}}u_{\text{me}}^{-1} \leq 0.1$ (station) and $v_{\text{ship}}u_{\text{me}}^{-1} > 0.1$ (underway) and bin average over 2 m s⁻¹ wind speed bins; the error bars represent the standard deviation.

5.5.3 Residual Humidity Bias after drying

Figure 5.17 shows the scatter of F_c from *dryA* against the estimates from *dryB* like in Fig. 5.6, but using the magnitude of the residual humidity

Webb-bias flux as colour code. The humidity flux signal of *dryA* and *dryB* is clearly reduced by the diffusion dryer, but the Webb-correction term for water vapour still reaches values of 20 mol m⁻² yr⁻¹. Even though the Webb correction has been applied to both CO₂ fluxes, an obvious increase in scatter between the two flux signals can be observed when the correction term becomes larger than 1 mol m⁻² yr⁻¹.

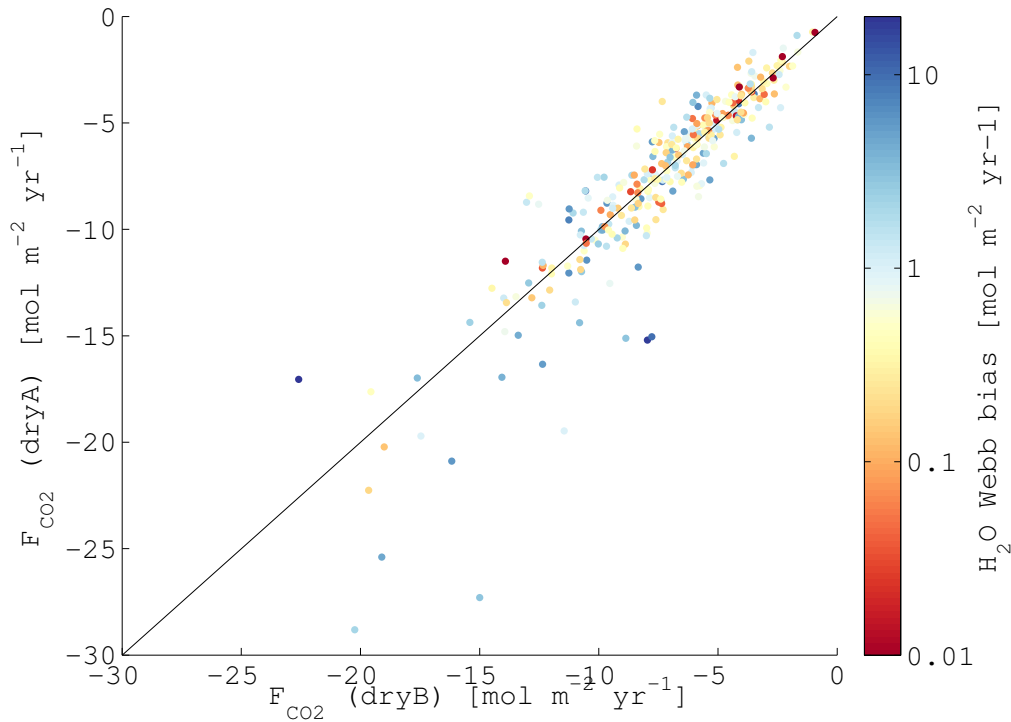


Figure 5.17: Scatter plot of the CO₂ flux measurements from *dryA* against those from *dryB*. The magnitude of the larger one of the two humidity Webb-correction terms from *dryA* and *dryB* is used as color code with logarithmic scaling.

Figure 5.18 shows averaged co-spectra of CO₂ and H₂O, C_{wc} and C_{wq} from the sensor *dryA* for two subsets: where the ratio $v_{\text{ship}}u^{-1}$ was limited to be less than 0.1 and the relative wind direction was limited to $\alpha \leq 30^\circ$, to avoid flow distortion effects. The first subset contains 41 intervals with $F_q \leq 1$ mol m⁻² yr⁻¹. The average magnitude of the latent heat flux was 60 W m⁻². The second subset contains 28 intervals with $F_q \geq 1$ mol m⁻² yr⁻¹;

here the average magnitude of the latent heat flux was 100 W m^2 . From the second subset it can be seen that downstream of the diffusion dryer, the residual humidity flux signal is restricted to low frequencies i.e. the diffusion dryer works as a strong low pass filter for H₂O. The residual humidity flux signal, however, causes a bias in the low frequency part of the CO₂ signal. This shows that the humidity flux bias can also occur downstream the dryer, albeit with a reduced intensity compared to the *un-dried* measurements. The magnitude of the residual water vapour flux recorded by the IRGA should be used as an additional quality control for the CO₂ flux measurements.

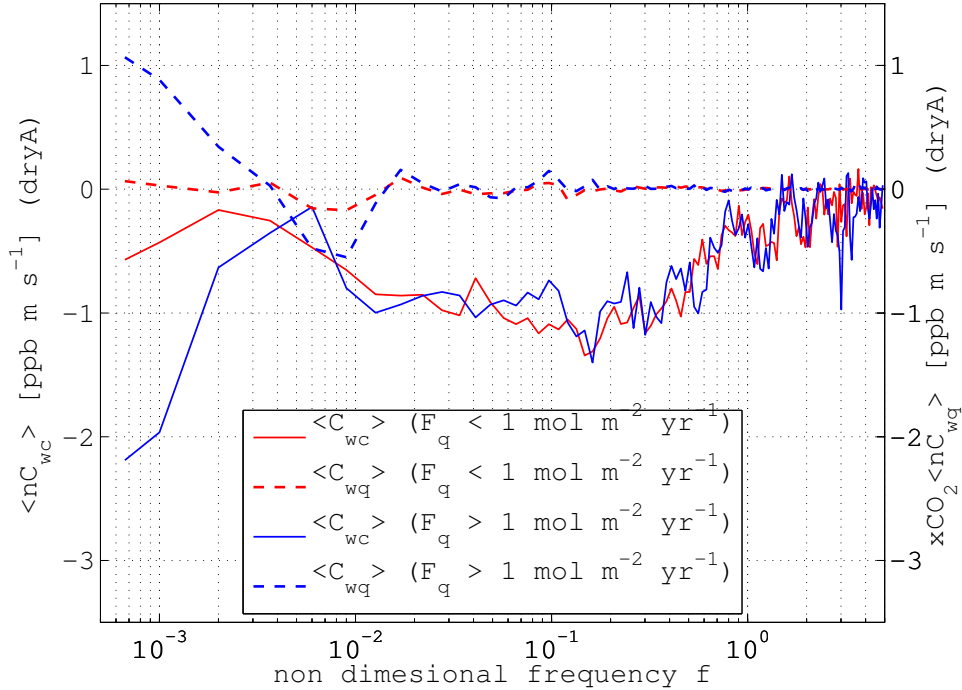


Figure 5.18: Average co-spectra of CO₂ (-) and H₂O (- -) from *dryA* as function of the non dimensional frequency. The H₂O co-spectra are weighted with the CO₂ mixing ratio to obtain the magnitude of the Webb-correction. The average co-spectra for the two subsets are shown in different colours: red showing an average from 41 intervals where $F_q \leq 1 \text{ mol m}^{-2} \text{ yr}^{-1}$; blue for 28 intervals with $F_q \geq 1 \text{ mol m}^{-2} \text{ yr}^{-1}$. To avoid flow distortion effects, the ratio $v_{\text{ship}}u^{-1}$ was limited to less than 0.1 and the relative wind direction was limited to $\alpha \leq 30^\circ$. The wind speed range was $7 - 15 \text{ m s}^{-1}$, the average 12 m s^{-1} , and the average relative wind direction $\alpha \leq 15^\circ$ for both subsets.

5.5.4 High Frequency Attenuation

The ogive method (see Sec. 3.2.7) was used to estimate the loss of high frequency fluctuations in the *dry* CO₂ and *wet* H₂O co-spectra. The data set was restricted to $|Q_{sen}| \geq 10 \text{ W m}^{-2}$, $v_{ship}u^{-1} \leq 0.1$, and $-30^\circ \leq \alpha \leq 30^\circ$. The frequency containing 50% of the sonic sensible heat flux ($n_{50\%}$) was estimated and Fig. 5.19 shows a scatter plot of $n_{50\%}$ and u_{10N} . For neutral and unstable conditions $n_{50\%}$ increases linearly with the wind speed and is independent of the stability parameter. For stable stratification ($z/L_* \geq 0$) $n_{50\%}$ also increases with z/L_* . Both observation are in agreement with *Kaimal et al. (1972)*.

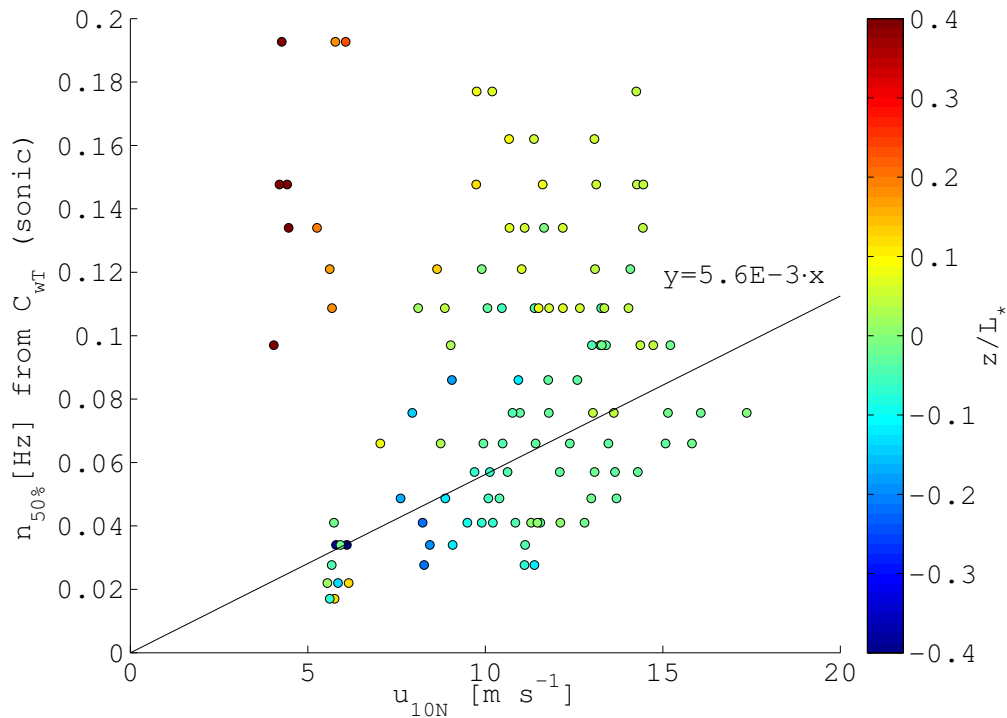


Figure 5.19: Scatter plot of the frequency containing 50% of the sonic sensible heat flux ($n_{50\%}$) and u_{10N} . The stability parameter z/L_* serves as colour code. A linear fit to the data fulfilling $z/L_* \leq 0.01$ is shown as black line.

The flux losses due to high frequency attenuation were estimated as a gain factor (g_{CO_2} and $g_{\text{H}_2\text{O}}$ for CO₂ and H₂O, respectively) using (3.17) and are plotted in Fig. 5.20 as a function of $u_{10\text{N}}$. For CO₂ the ogive of $n_{50\%}$ was used. For H₂O, where the attenuation was manifested at lower frequencies, $n_{20\%}$ was used to estimate the flux loss. The individual results exhibit large scatter, and no clear dependency of g_{CO_2} or $g_{\text{H}_2\text{O}}$ with either wind speed or stability was observed. The average gains are $g_{\text{CO}_2} = 1.06 \pm 0.20$ and $g_{\text{H}_2\text{O}} = 1.68 \pm 0.82$, and agree well with the estimates which were obtained from 6 hourly average spectra at $u_{10\text{N}} = 14 \text{ m s}^{-1}$ ($g_{\text{CO}_2} = 1.06$ and $g_{\text{H}_2\text{O}} = 1.57$; see Sec. 3.2.7).

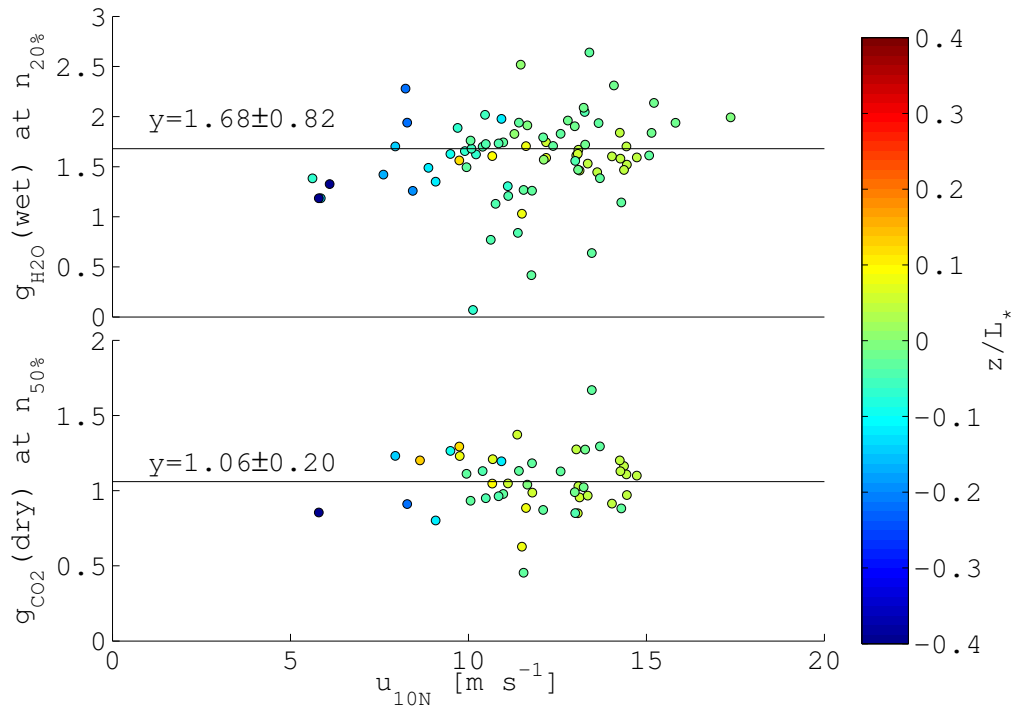


Figure 5.20: Scatter plot of the gains of H₂O (top) CO₂ (bottom) and $u_{10\text{N}}$. The stability parameter z/L_* serves as colour code. The gains were estimated with $n_{50\%}$ and $n_{20\%}$ for g_{CO_2} and $g_{\text{H}_2\text{O}}$, respectively. The average values are shown as black line and stated together with the standard deviation.

5.6 Conclusions

Measurements of the air–sea CO₂ flux over the open ocean were conducted with four IRGAs, two of which had the water vapour fluctuations removed with a membrane dryer (*Miller et al.*, 2010). The flux results from the dried and un-dried sensors agreed with each other during periods of very low latent heat flux, demonstrating that the membrane dryer does not alter the CO₂ flux signal. With increasing latent heat flux, the CO₂ flux measurements from the un-dried sensors showed large bias and scatter. This is similar to earlier studies *Kondo and Osamu* (2007); *Lauvset et al.* (2011); *Prytherch et al.* (2010a). In this study the bias flux was positive (on average) leading to a net reduction of the downward CO₂ flux.

The PKT correction reduced the scatter in the flux measurements from the un-dried gas analysers from 1000 % to 100 % of the flux signal. However, the PKT-corrected fluxes showed only a weak correlation with the flux measurements from the dried gas analysers. A detailed analysis of the PKT algorithm was performed, which revealed that the loop in the PKT correction can be replaced by a single equation. The PKT-corrected flux was shown to be a product of the de-trended CO₂ flux and a factor that depends solely on the latent heat flux and relative humidity. The PKT method cannot be used to retrieve the true CO₂ from the measured signal, since detrending to remove the bias also removes most of the CO₂ flux information. Conclusions made based on PKT-corrected CO₂ flux measurements should be treated with care. The same holds for the spectral cross correlation correction method, which was presented by (*Edson et al.*, 2011). This method assumes a constant relation between the observed cross-correlation of the measured (biased)

CO₂ and H₂O signals and the correlation between the true CO₂ signal and H₂O. This is rather unlikely.

The results support the conclusions of *Miller et al.* (2010) that the order of magnitude bias in the measured CO₂ fluxes can be removed when the sample air is dried. The authors therefore strongly recommend the use of the closed-path IRGAs with a diffusion dryer as presented by *Miller et al.* (2010) for EC flux measurements over the open ocean. The humidity bias was observed even downstream of the diffusion dryer. The magnitude of the residual water vapour flux must therefore be monitored carefully.

Further analysis is necessary, to remove or quantify the flux errors due to air-flow distortion and the attenuation of high frequency fluctuations, before SOAP (and Knorr11) data sets can be used for parameterisation of k_{660} .

6 Conclusions and Future Work

Air-sea fluxes of momentum, heat (latent and sensible), and CO₂ were measured on three shipborne experiments with the eddy covariance method. This thesis presents the analysis of the data sets obtained during these experiments. The three experiments took place in different parts of the World's oceans (North Atlantic in 2011; Southern Ocean in 2012; Subtropical North Atlantic in 2013) and involved a suite of measurements of additional environmental variables (e.g. sea state, biological activity, subsurface turbulence, and mixing layer depth) with the objective of studying the influence of these environmental parameters on the transfer coefficients of air-sea exchange. These measurements add significant value to the direct flux measurements. The focus of this work, however, was on the various corrections which need to be applied to the raw EC flux data prior to the calculation of the covariances, which provide the magnitude and direction of the air-sea fluxes.

A significant source of error in direct EC fluxes was found to be introduced by the standard procedure of estimating the wind vector pitch from the motion-corrected wind speed. The wind vector measured on large oceanographic platforms, such as ships or coastal towers, is tilted away from its original direction when the stream lines circumvent the structure (*Popinet et al.*, 2004). For measurement of fluxes with the EC method, the stream line coordinate system needs to be determined, i.e. the measured wind

vector has to be rotated to fix the long-term averages of the vertical and cross-wind component to zero (*McMillen, 1988*). At sea the stream line coordinate system is usually approximated by rotating a 10-30 minute interval of motion-corrected wind speed until the interval averages of vertical- and cross-wind components are zero (*Edson et al., 1998*). In Chapter 4 it was shown that this procedure over-estimated the wind vector tilt when the platform has non-zero average velocity. This is due to the fact that the tilt is calculated from the motion-corrected wind vector, while the flow distortion acts on the (usually larger) relative wind vector (i.e. relative to the platform). The error in wind vector pitch and yaw (relative wind direction) leads to biased direct flux estimates. The errors are largest in the stress estimates, but scalar fluxes are also affected significantly. In the presented work an alternative correction method (radial planar fit - rPF) for the wind vector distortion on moving platforms has been developed which can significantly reduce the error in direct flux measurements caused by air-flow distortion.

Direct air-sea CO₂ flux measurements in particular are affected by cross sensitivity of the CO₂ signal to ambient humidity fluctuations which lead to order-of-magnitude errors (*Prytherch et al., 2010a*). *Miller et al. (2010)* demonstrate that this error source can be reduced significantly by the deployment of membrane dryers, which remove $\sim 97\%$ of the water vapour fluctuations. This application is restricted to closed-path measurements with the drawback of high energy consumption (pump), high maintenance, and possible loss of flux information due to high frequency attenuation. However, this latter issue can be resolved by applying corrections using open-path measurements of the sensible or latent heat flux spectra. Alternatively, *Prytherch et al. (2010a)* and *Edson et al. (2011)* have proposed post-processing corrections for open-path flux measurements.

During the SOAP experiment, the two approaches were tested side by side. The results, presented in Chapter 5, show that the post-processing corrections do not recover the same CO₂ flux as measured by the *Miller et al.* (2010) method. The detailed analysis of the correction algorithm in Section 5.4 proved that the proposed correction method by *Prytherch et al.* (2010a) is not valid. Before a better understanding of the humidity-cross talk in the deployed dispersive IRGAs is achieved, air-sea CO₂ fluxes should be measured after the removal of water vapour, following *Miller et al.* (2010). It was also found that the humidity bias persists, even downstream of the diffusion dryer, when the humidity flux signal cannot be completely removed. Therefore, the magnitude of the residual humidity flux should be monitored and used to reject potentially biased CO₂ flux results.

During the Knorr11 and SOAP experiments in the North Atlantic and the South Pacific, respectively, two highly valuable direct flux datasets were obtained that allow for a better constraint of the gas transfer velocities for CO₂ and DMS in these highly productive regions. DMS transfer velocities from the Knorr11 experiment were published in *Bell et al.* (2013). In order to improve the estimates of wind stress and gas-transfer velocities, the rPF motion-tilt correction method should be used to recalculate (u', v', w') for these two experiments. A direct comparison of momentum flux measurements at different locations will provide an estimate of residual air-flow distortion errors in the direct fluxes. For the R/V-*Knorr*, detailed large eddy simulations of mean air-flow distortion have been finalised recently *personal communication, Niall O'Sullivan*. The recalculated CO₂ fluxes should be corrected for high frequency attenuation and carefully screened for bias signals arising from residual humidity fluctuations. Where measurements from multiple analysers are available, these could be combined to further

reduce measurement uncertainty.

The finding of this thesis will provide means to reprocess previous flux data sets with the new rPF method in order to remove flow distortion-induced biases and thus generate more usable data for scientific analysis. It also shows unambiguously that the only valid method for EC measurements of air-sea CO₂ fluxes is to physically remove the water vapour fluctuations, to avoid large biases that cannot be corrected during data processing.

Bibliography

- Adams, D. (1979), *The hitchhiker's guide to the galaxy*, Pan Books, United Kingdom.
- Anctil, F., M. A. Donelan, W. M. Drennan, and H. C. Graber (1993), Eddy-correlation measurements of air-sea fluxes from a discus buoy, *J. Atmos. Oceanic Technol.*, *11*, 1144–1150.
- Andreas, E. L., and G. Treviño (2000), Comments on “a physical interpretation of von kármán’s constant based on asymptotic considerations - a new value”, *Journal of Atmospheric Sciences*, *57*, 1189–1192, doi: 10.1175/1520-0469(2000)057<1189:COAPIO>2.0.CO;2.
- Anguelova, M. D., and F. Webster (2006), Whitecap coverage from satellite measurements: A first step toward modeling the variability of oceanic whitecaps, *J. Geophys. Res.*, *111*(C03017), doi:10.1029/2005JC003158.
- Bell, T. G., W. De Bruyn, S. D. Miller, B. Ward, K. Christensen, and E. S. Saltzman (2013), Air-sea dimethylsulfide (dms) gas transfer in the north atlantic: evidence for limited interfacial gas exchange at high wind speed, *Atmospheric Chemistry and Physics*, *13*, 11,073–11,087.
- Blomquist, B., B. Huebert, C. Fairall, L. Bariteau, J. Edson, J. Hare, and W. McGillis (2014), Advances in air–sea CO₂ flux measurement by

-
- eddy correlation, *Boundary-Layer Meteorology*, pp. 1–32, doi:10.1007/s10546-014-9926-2.
- Blomquist, B. W., C. W. Fairall, B. J. Huebert, D. J. Kieber, and G. R. Westby (2006), Dms sea-air transfer velocity: Direct measurements by eddy covariance and parameterization based on the noaa/coare gas transfer model, *Geophys. Res. Lett.*, *33*(7), n/a–n/a, doi:10.1029/2006GL025735.
- Blomquist, B. W., B. J. Huebert, C. W. Fairall, and I. C. Faloona (2010), Determining the sea-air flux of dimethylsulfide by eddy correlation using mass spectrometry, *Atmos. Meas. Tech.*, *3*(1), 1–20, doi:10.5194/amt-3-1-2010.
- Bock, E. J., T. Hara, N. M. Frew, and W. R. McGillis (1999), Relationship between air-sea gas transfer and short wind waves, *J. Geophys. Res.*, *104*, 25,821–25,831, doi:10.1029/1999JC900200.
- Broecker, H. C., and W. Siemens (1984), The role of bubbles for gas transfer from water to air at higher wind speeds. experiments in the wind-wave facility in hamburg, in *Gas transfer at water surfaces*, edited by W. Brutsaert and G. H. Jirka, pp. 229–236, Reidel, D.
- Broecker, W. S., J. R. Ledwell, T. Takahashi, L. M. R. Weiss, L. Memery, T.-H. Peng, B. Jähne, and K. O. Münnich (1986), Isotopic versus micrometeorologic ocean CO₂ fluxes: A serious conflict, *J. Geophys. Res.*, *91*, 10,517–10,527.
- Brunke, M. A., C. W. Fairall, X. Zeng, L. Eymard, and J. A. Curry (2003), Which bulk aerodynamic algorithms are least problematic in computing ocean surface turbulent fluxes?., *Journal of Climate*, *16*(4), 619.
- Burba, G., and D. Anderson (2010), *A Brief Practical Guide to Eddy Covariance Flux Measurements: Principles and Workflow Examples for Scientific*

and Industrial Applications, LI-COR Biosciences, Lincoln, Nebraska 68504 USA.

Burns, S. P., T. W. Horst, L. Jacobsen, P. D. Blanken, and R. K. Monson (2012), Using sonic anemometer temperature to measure sensible heat flux in strong winds, *Atmos. Meas. Tech.*, *5*, 2095–2111.

Callaghan, A. H., and M. White (2009), Automated processing of sea surface images for the determination of whitecap coverage, *J. Atmos. Oceanic Technol.*, *26*(2), 383–394, doi:10.1175/2008JTECHO634.1.

Callaghan, A. H., G. B. Deane, M. D. Stokes, and B. Ward (2012), Observed variation in the decay time of oceanic whitecap foam, *J. Geophys. Res.: Oceans*, *117*(C9), n/a–n/a, doi:10.1029/2012JC008147.

Charnock, H. (1955), Wind stress on a water surface, *Quart. J. Roy. Meteor. Soc.*, *81* (350), 639–640, doi:10.1002/qj.49708135027.

Chriss, T. M., and D. R. Caldwell (1984), Universal similarity and the thickness of the viscous sublayer at the ocean floor, *J. Geophys. Res.*, *89*(C4), 6403–6414.

Corrsin, S. (1951), On the spectrum of isotropic temperature fluctuations in an isotropic turbulence, *Journal of Applied Physics*, *22*(4), 469–473, doi:http://dx.doi.org/10.1063/1.1699986.

Csanady, G. T. (1990), The role of breaking wavelets in air-sea gas transfer, *J. Geophys. Res.: Oceans*, *95*(C1), 749–759, doi:10.1029/JC095iC01p00749.

Danckwerts, P. (1951), Significance of liquid-film coefficients in gas absorption, *Industrial Engineering Chemistry*, *43*, 1460–1467.

- Deacon, E. L. (1969), The levelling error in reynolds stress measurements, *Bull. Amer. Meteor. Soc.*, *49*, 836.
- Deacon, E. L. (1977), Gas transfer to and across an air-water interface, *Tellus*, *29*, 363–374, doi:10.1111/j.2153-3490.1977.tb00746.x.
- Dupuis, H., C. Guerin, D. Hauser, A. Weill, P. Nacass, W. M. Drennan, S. Cloché, and H. C. Graber (2003), Impact of flow distortion corrections on turbulent fluxes estimated by the inertial dissipation method during the fetch experiment on r/v l'atalante, *J. Geophys. Res.: Oceans*, *108*(C3), 8064, doi:10.1029/2001JC001075.
- Dyer, A. J. (1974), A review of flux-profile relationships, *Boundary-Layer Meteorology*, *7*, 363–372.
- Dyer, A. J., and B. B. Hicks (1970), Flux-gradient relationships in the constant flux layer, *Quart. J. Roy. Meteor. Soc.*, *96*(410), 715–721, doi:10.1002/qj.49709641012.
- Edson, J. B., C. W. Fairall, P. G. Mestayer, and S. E. Larsen (1991), A study of the inertial-dissipation method for computing air-sea fluxes, *J. Geophys. Res.*, *96*(C6), 10,689–10,711, doi:10.1029/91JC00886.
- Edson, J. B., A. A. Hinton, K. E. Prada, J. E. Hare, and C. W. Fairall (1998), Direct covariance flux estimates from mobile platforms at sea, *J. Atmos. Oceanic Technol.*, *15*, 547–562.
- Edson, J. B., C. J. Zappa, J. A. Ware, W. R. McGillis, and J. E. Hare (2004), Scalar flux profile relationships over the open ocean, *J. Geophys. Res.: Oceans*, *109*(C8), n/a–n/a, doi:10.1029/2003JC001960.

- Edson, J. B., C. W. Fairall, L. Bariteau, C. J. Zappa, A. Cifuentes-Lorenzen, W. R. McGillis, S. Pezoa, J. E. Hare, and D. Helmig (2011), Direct covariance measurement of co₂ gas transfer velocity during the 2008 southern ocean gas exchange experiment: Wind speed dependency, *J. Geophys. Res.: Oceans*, *116*(C4), C00F10, doi:10.1029/2011JC007022.
- Edson, J. B., V. Jampana, R. A. Weller, S. P. Bigorre, A. J. Plueddemann, C. W. Fairall, S. D. Miller, L. Mahrt, D. Vickers, and H. Hersbach (2013), On the exchange of momentum over the open ocean, *J. Phys. Oceanogr.*, *43*, 1589—1610, doi:10.1175/JPO-D-12-0173.1.
- Fairall, C., J. Hare, J. Edson, and W. McGillis (2000), Parameterization and micrometeorological measurement of air–sea gas transfer, *Boundary-Layer Meteorology*, *96*(1-2), 63–106, doi:10.1023/A:1002662826020.
- Fairall, C. W., E. F. Bradley, D. P. Rogers, J. B. Edson, and G. S. Young (1996a), Bulk parameterization of air-sea fluxes for tropical ocean-global atmosphere coupled-ocean atmosphere response experiment, *J. Geophys. Res.: Oceans*, *101*(C2), 3747–3764, doi:10.1029/95JC03205.
- Fairall, C. W., E. F. Bradley, J. S. Godfrey, G. A. Wick, J. B. Edson, and G. S. Young (1996b), Cool-skin and warm-layer effects on sea surface temperature, *J. Geophys. Res.: Oceans*, *101*(C1), 1295–1308, doi:10.1029/95JC03190.
- Fairall, C. W., E. F. Bradley, J. E. Hare, A. A. Grachev, and J. B. Edson (2003), Bulk parameterization of air-sea fluxes: Updates and verification for the coare algorithm, *Journal of Climate*, *16*, 571–591, doi:10.1175/1520-0442(2003)016<0571:BPOASF>2.0.CO;2.
- Fairall, C. W., M. Yang, L. Bariteau, J. B. Edson, D. Helmig, W. McGillis,

- S. Pezoa, J. E. Hare, B. Huebert, and B. Blomquist (2011), Implementation of the coupled ocean-atmosphere response experiment flux algorithm with CO_2 , dimethyl sulfide, and O_3 , *J. Geophys. Res.: Oceans*, 116(C4), n/a–n/a, doi:10.1029/2010JC006884.
- Frew, N. M., E. J. Bock, U. Schimpf, T. Hara, H. Haußecker, J. B. Edson, W. R. McGillis, R. K. Nelson, S. P. McKenna, B. M. Uz, and B. Jähne (2004), Air-sea gas transfer: Its dependence on wind stress, small-scale roughness, and surface films, *J. Geophys. Res.*, 109, C08S17.
- Goddijn-Murphy, L., D. K. Woolf, and C. A. Marandino (2012), Space-based retrievals of air-sea gas transfer velocities using altimeters; calibration for dimethyl sulfide, *J. Geophys. Res.*, doi:10.1029/2011JC007535.
- Griessbaum, F., and A. Schmidt (2009), Advanced tilt correction from flow distortion effects on turbulent CO_2 fluxes in complex environments using large eddy simulation, *Quart. J. Roy. Meteor. Soc.*, 135(643), 1603–1613, doi:10.1002/qj.472.
- Hare, J. E., C. W. Fairall, W. R. McGillis, J. B. Edson, B. Ward, and R. Wanninkhof (2004), Evaluation of the national oceanic and atmospheric administration/coupled-ocean atmospheric response experiment (noaa/coare) air-sea gas transfer parameterization using gasex data, *J. Geophys. Res.: Oceans*, 109(C8S11), n/a–n/a, doi:10.1029/2003JC001831.
- Higby, R. (1935), The rate of absorption of a pure gas into a still liquid during short periods of exposure, *Transactions of the American Institute of Chemical Engineers*, 31, 365–388.
- Hill, R. J. (1989), Structure functions and spectra of scalar quantities in the inertial–convective and viscous–convective ranges of turbulence, *J. At-*

mos. Sci., 46, 2245—2251, doi:[http://dx.doi.org/10.1175/1520-0469\(1989\)046<2245:SFASOS>2.0.CO;2](http://dx.doi.org/10.1175/1520-0469(1989)046<2245:SFASOS>2.0.CO;2).

Ho, D., C. Law, M. Smith, P. Schlosser, M. Harvey, and P. Hill (2006), Measurements of air-sea gas exchange at high wind speeds in the southern ocean: Implications for global parameterizations, *Geophys. Res. Lett.*, 33, L16,611, doi:10.1029/2006GL026817.

Ho, D. T., R. Wanninkhof, P. Schlosser, D. S. Ullman, D. Hebert, and K. F. Sullivan (2011), Toward a universal relationship between wind speed and gas exchange: Gas transfer velocities measured with $^3\text{He}/\text{SF}_6$ during the southern ocean gas exchange experiment, *J. Geophys. Res.*, 116, C00F04, doi:10.1029/2010JC006854.

Högström, U. (1996), Review of some basic characteristics of the atmospheric surface layer, *Boundary-Layer Meteorology*, 78(3-4), 215–246, doi:10.1007/BF00120937.

Huang, Y., J. Song, J. Wang, and C. Fan (2012), Air-sea carbon-dioxide flux estimated by eddy covariance method from a buoy observation, *Acta Oceanol. Sin.*, 31, 66–71, doi:10.1007/s13131-012-0253-5.

Ikawa, H., I. Faloona, J. Kochendorfer, T. Paw U, K., and C. Oechel, W. (2013), Air–sea exchange of CO_2 at a northern california coastal site along the california current upwelling system, *Biogeosciences*, 10, 4419–4432, doi:www.biogeosciences.net/10/4419/2013/.

Jähne, B., W. Huber, A. Dutzi, T. Wais, and J. Ilmberger (1984), Wind/wave-tunnel experiment on the schmidt number—and wave field dependence of air/water gas exchange, in *Gas transfer at water surfaces*, edited by W. Brutsaert and G. H. Jirka, pp. 303–309, D. Reidel.

- Jähne, B., K. O. Münnich, R. Börsinger, A. Dutzi, W. Huber, and P. Libner (1987), On the parameters influencing air-water gas exchange, *J. Geophys. Res.: Oceans*, *92*(C2), 1937–1949, doi:10.1029/JC092iC02p01937.
- Jeffery, C., D. Woolf, I. Robinson, and C. Donlon (2007), One-dimensional modelling of convective CO₂ exchange in the tropical atlantic, *Ocean Modelling*, *19*(3-4), 161–182, doi:http://dx.doi.org/10.1016/j.ocemod.2007.07.003.
- Kaimal, J. C., J. C. Wyngaard, Y. Izumi, and O. R. Coté (1972), Spectral characteristics of surface-layer turbulence, *Quart. J. Roy. Meteor. Soc.*, *98*, 563–589.
- Keeling, R. F. (1993), On the role of large bubbles in air-sea gas exchange and supersaturation in the ocean, *Journal of marine research*, *51*(2), 237–271.
- Kohsiek, W. (2000), Water vapor cross-sensitivity of open path H₂O/CO₂ sensors, *J. Atmos. Oceanic Technol.*, *17*, 299–311.
- Kondo, F., and T. Osamu (2007), Air-sea CO₂ flux by eddy covariance technique in the equatorial indian ocean, *J. Oceanogr.*, *63*, 449–456.
- Kondo, F., and O. Tsukamoto (2012), Comparative CO₂ flux measurements by eddy covariance technique using open- and closed-path gas analysers over the equatorial pacific ocean, *Tellus*, *64B*(17511), doi:10.3402/tellusb.v64i0.17511.
- Lamont, J. C., and D. S. Scott (1970), An eddy cell model of mass transfer into the surface of a turbulent liquid, *AIChE J.*, *16*(4), 513–519, doi:10.1002/aic.690160403.

- Landwehr, S., S. D. Miller, M. J. Smith, E. S. Saltzman, and B. Ward (2014), Analysis of the pkt correction for direct CO₂ flux measurements over the ocean, *Atmospheric Chemistry and Physics*, *14*(7), 3361–3372, doi:10.5194/acp-14-3361-2014.
- Lauvset, S. K., W. R. McGillis, L. Bariteau, C. W. Fairall, T. Johannessen, A. Olsen, and C. J. Zappa (2011), Direct measurements of CO₂ flux in the greenland sea, *Geophys. Res. Lett.*, *38*, L12603, doi:doi:10.1029/2011GL047722.
- Lenschow, D. H., and M. R. Raupach (1991), The attenuation of fluctuations in scalar concentrations through sampling tubes, *J. Geophys. Res.: Atmosphere*, *96*(D8), 15,259–15,268, doi:10.1029/91JD01437.
- Leuning, R., and K. M. King (1992), Comparison of eddy-covariance measurements of CO₂ fluxes by open- and closed-path CO₂ analysers, *Boundary-Layer Meteorology*, *59*, 297–311.
- Liss, P. S., and P. G. Slater (1974), Flux of gases across the air-sea interface, *Nature*, *247*, 181–184.
- Lorke, A., and F. Peeters (2006), Toward a unified scaling relation for interfacial fluxes, *J. Phys. Oceanogr.*, *36*, 955–961, doi:http://dx.doi.org/10.1175/JPO2903.1.
- Marandino, C. A., W. J. Bruyn, S. D. Miller, and E. S. Saltzman (2007), Eddy correlation measurements of the air/sea flux of dimethylsulfide over the north pacific ocean, *J. Geophys. Res.*, *112*, D03,301.
- McGillis, W., J. Edson, J. Hare, and C. W. Fairall (2001a), Direct covariance air-sea CO₂ fluxes, *J. Geophys. Res.*, *106*(C8), 16,729–16,745.

-
- McGillis, W. R., J. B. Edson, J. D. Ware, J. W. Dacey, J. E. Hare, C. W. Fairall, and R. Wanninkhof (2001b), Carbon dioxide flux techniques performed during gasex-98, *Mar. Chem.*, *75*(4), 267 – 280, doi:[http://dx.doi.org/10.1016/S0304-4203\(01\)00042-1](http://dx.doi.org/10.1016/S0304-4203(01)00042-1).
- McGillis, W. R., J. B. Edson, C. J. Zappa, J. D. Ware, S. P. McKeanna, E. A. Terray, J. E. Hare, C. W. Fairall, W. Drennan, M. Donelan, M. D. DeGrandpre, R. Wanninkhof, and R. A. Feely (2004), Air-sea CO₂ exchange in the equatorial pacific, *J. Geophys. Res.*, *109*(C8), C08S02, doi:10.1029/2003JC002256.
- McMillen, R. (1988), An eddy correlation technique with extended applicability to non-simple terrain, *Boundary-Layer Meteorology*, *43*(3), 231–245, doi:10.1007/BF00128405.
- McVeigh, P. (2009), Micrometeorological and CO₂ fluxes in the coastal environment, Ph.D. thesis, School of Physics, National University of Ireland Galway.
- Miller, S., T. Hristov, J. Edson, and C. Friehe (2008), Platform motion effects on measurements of turbulence and air-sea exchange over the open ocean, *J. Atmos. Oceanic Technol.*, *25*(9), 1683–1694.
- Miller, S., C. Marandino, W. van de Bruyn, and E. S. Saltzman (2009), Air-sea gas exchange of CO₂ and DMS in the north atlantic by eddy covariance, *Geophys. Res. Lett.*, *36*(15), L15,816, doi:10.1029/2009GL038907.
- Miller, S. D., C. Marandino, and E. S. Saltzman (2010), Ship-based measurement of air-sea CO₂ exchange by eddy covariance, *J. Geophys. Res.*, *115*, D02,304, doi:10.1029/2009JD012193.

- Monahan, E. C., and M. C. Spillane (1984), The role of oceanic whitecaps in air-sea gas exchange., in *Gas transfer at water surfaces*, edited by W. Brutsaert and G. H. Jirka, pp. 495–503, Reidel, D.
- Monin, A. S., and A. M. Obukhov (1954), Basic regularity in turbulent mixing in the surface layer of the atmosphere, *Akad. Nauk. S.S.S.R. Trud. Geofiz. Inst.*, 24(151), 163–187.
- Nightingale, P. D., G. Malin, C. S. Law, A. J. Watson, P. S. Liss, M. I. Liddicoat, J. Boutin, and R. C. Upstill-Goddard (2000), In situ evaluation of air-sea gas exchange parameterizations using novel conservative and volatile tracers, *Global Biogeochem. Cycles*, 14, 373–387.
- Oost, W. A., C. W. Fairall, and J. B. Edson (1994), Flow distortion calculations and their application in hexmax, *J. Atmos. Oceanic Technol.*, 11, 366–386.
- O’Sullivan, N., S. Landwehr, and B. Ward (2013), Mapping flow distortion on oceanographic platforms using computational fluid dynamics, *Ocean Science*, 9(5), 855–866, doi:10.5194/os-9-855-2013.
- O’Sullivan, N., S. Landwehr, and B. Ward (2014), Air-flow distortion and wave interactions: An experimental and numerical comparison, *Methods in Ocea.*, (submitted).
- Pedreras, R., G. Dardier, H. Dupuis, H. C. Graber, W. M. Drennan, A. Weill, C. Guerin, and P. Nacass (2003), Momentum and heat fluxes via eddy correlation method on the r/v *L’Atalante* and an asis buoy, *J. Geophys. Res.*, 108, 3339.
- Popinet, S., M. Smith, and C. Stevens (2004), Experimental and numerical

- study of the turbulence characteristics of airflow around a research vessel, *J. Atmos. Oceanic Technol.*, *21*, 1575–1589.
- Prytherch, J., M. J. Yelland, R. W. Pascal, B. I. Moat, I. Skjelvan, and C. C. Neill (2010a), Direct measurements of the CO₂ flux over the ocean: Development of a novel method, *Geophys. Res. Lett.*, *37*(3), L03,607, doi:10.1029/2009GL041482.
- Prytherch, J., M. J. Yelland, R. W. Pascal, B. I. Moat, I. Skjelvan, and M. A. Srokosz (2010b), Open ocean gas transfer velocity derived from long-term direct measurements of the CO₂ flux, *Geophys. Res. Lett.*, *37*, L23,607, doi:10.1029/2010GL045597.
- Quinn, P. K., and T. S. Bates (2011), The case against climate regulation via oceanic phytoplankton sulphur emissions, *Nature*, *480*, 51–56.
- Rannik, Ü., T. Vesala, and R. Keskinen (1997), On the damping of temperature fluctuations in a circular tube relevant to the eddy covariance measurement technique, *J. Geophys. Res.*, *102*, 12,789–12,794.
- Rieder, K. F., J. A. Smith, and R. A. Weller (1994), Observed directional characteristics of the wind, wind stress, and surface waves on the open ocean, *J. Geophys. Res.: Oceans*, *99*(C11), 22,589–22,596, doi:10.1029/94JC02215.
- Rowe, M. D., C. W. Fairall, and J. A. Perlinger (2011), Chemical sensor resolution requirements for near-surface measurements of turbulent fluxes, *Atmospheric Chemistry and Physics*, *11*, 5263–5275, doi:doi:10.5194/acp-11-5263-2011.
- Rutgersson, A., and A. Smedman (2010), Enhanced air–sea CO₂ transfer due

- to water-side convection, *J. Mar. Syst.*, *80*(1-2), 125–134, doi:10.1016/j.jmarsys.2009.11.004.
- Scanlon, B., and B. Ward (2013), Oceanic wave breaking coverage separation techniques for active and maturing whitecaps, *Methods in Ocea.*, *8*, 1–12, doi:10.1016/j.mio.2014.03.001.
- Schulz, E. W., B. G. Sanderson, and E. F. Bradley (2005), Motion correction for shipborne turbulence sensors, *J. Atmos. Oceanic Technol.*, *22*, 55–69, doi:http://dx.doi.org/10.1175/JTECH-1685.1.
- Smith, S. D. (1988), Coefficients for sea surface wind stress, heat flux, and wind profiles as a function of wind speed and temperature, *J. Geophys. Res.*, *93*(C12), 15,467–15,472, doi:10.1029/JC093iC12p15467.
- Soloviev, A. V. (2007), Coupled renewal model of ocean viscous sublayer, thermal skin effect and interfacial gas transfer velocity, *Journal of Marine Systems*, *66*(1–4), 19 – 27, doi:http://dx.doi.org/10.1016/j.jmarsys.2006.03.024.
- Soloviev, A. V., and P. Schlüssel (1994), Parameterization of the cool skin of the ocean and of the air-ocean gas transfer on the basis of modeling surface renewal, *J. Phys. Oceanogr.*, *24*, 1339–1346, doi:http://dx.doi.org/10.1175/1520-0485(1994)024<1339:POTCSO>2.0.CO;2.
- Sutherland, G., B. Ward, and K. H. Christensen (2013), Wave-turbulence scaling in the ocean mixed layer, *Ocean Science*, *9*, 597–608.
- Sutherland, G., K. H. Christensen, and B. Ward (2014), Evaluating Langmuir turbulence parameterizations in the ocean surface boundary layer, *J. Geophys. Res.: Oceans*, *119*, doi:10.1002/2013JC009537.

- Sweeney, C., E. Gloor, A. Jacobson, R. M. Key, G. McKinley, J. L. Sarmiento, and R. Wanninkhof (2007), Constraining global air-sea gas exchange for CO_2 with recent bomb ^{14}C measurements, *Global Biogeochem. Cycles*, *21*, GB2015.
- Takahashi, T., S. C. Sutherland, C. Sweeney, A. Poisson, N. Metzl, B. Tilbrook, N. Bates, R. Wanninkhof, R. A. Feely, C. Sabine, J. Olafsson, and Y. Nojiri (2002), Global sea-air CO_2 flux based on climatological surface ocean pCO_2 , and seasonal biological and temperature effects, *Deep Sea Research Part II: Topical Studies in Oceanography*, *49*(9–10), 1601 – 1622, doi:[http://dx.doi.org/10.1016/S0967-0645\(02\)00003-6](http://dx.doi.org/10.1016/S0967-0645(02)00003-6).
- Taylor, M. J. Y., Peter K. (2000), On the apparent “imbalance” term in the turbulent kinetic energy budget, *J. Atmos. Oceanic Technol.*, *17*, 82–89, doi:[http://dx.doi.org/10.1175/1520-0426\(2000\)017<0082:OTAITI>2.0.CO;2](http://dx.doi.org/10.1175/1520-0426(2000)017<0082:OTAITI>2.0.CO;2).
- Wanninkhof, R. (1992), Relationship between wind speed and gas exchange, *J. Geophys. Res.*, *97*, 7373–7382.
- Wanninkhof, R., and W. R. McGillis (1999), A cubic relationship between air-sea CO_2 exchange and wind speed, *Geophys. Res. Lett.*, *26*, 1889–1892.
- Wanninkhof, R., W. Asher, and E. Monahan (1995), The influence of bubbles on air-water gas exchange: Results from gas transfer experiments during wabex-93, in *Air-Water Gas Transfer: Selected papers from the Third International Symposium on air-water gas transfer*, edited by B. Jähne and E. C. Monahan, pp. 239–255, Aeon-Verlag, Hanau, Germany.
- Ward, B., R. Wanninkhof, W. R. McGillis, A. T. Jessup, M. D. DeGrandpre, J. E. Hare, and J. B. Edson (2004), Biases in the air-sea flux of CO_2

- resulting from ocean surface temperature gradients, *J. Geophys. Res.*, *109*, C08S08, doi:10.1029/2003JC001800.
- Webb, E. K., G. I. Pearman, and R. Leuning (1980), Correction of flux measurements for density effects due to heat and water vapour transfer, *Quart. J. Roy. Meteor. Soc.*, *106*, 85–100.
- Weiss, R. (1974), Carbon dioxide in water and seawater; the solubility of a non-ideal gas, *Mar. Chem.*, *2*, 203–215.
- Wilczak, J., S. Oncley, and S. Stage (2001), Sonic anemometer tilt correction algorithms, *Boundary-Layer Meteorology*, *99*(1), 127–150, doi:10.1023/A:1018966204465.
- Woolf, D. K. (1997), Bubbles and their role in gas exchange, in *The Sea Surface and Global Change*, edited by P. S. Liss and R. A. Duce, pp. 173–206, Cambridge University Press, cambridge Books Online.
- Wyngaard, J. C. (1981), The effects of probe-induced flow distortion on atmospheric turbulence measurements, *J. Appl. Meteor.*, *20*, 784 – 794.
- Yang, M., B. W. Blomquist, C. W. Fairall, S. D. Archer, and B. J. Huebert (2011), Air-sea exchange of dimethylsulfide in the southern ocean: Measurements from so gasex compared to temperate and tropical regions, *J. Geophys. Res.: Oceans*, *116*(C4), n/a–n/a, doi:10.1029/2010JC006526.
- Yelland, M., B. Moat, R. Pascal, and D. Berry (2002), Cfd model estimates of the airflow distortion over research ships and the impact on momentum flux measurements, *J. Atmos. Oceanic Technol.*, *19*(10), 1477–1499, doi:10.1175/1520-0426(2002)019<1477:CMEOTA>2.0.CO;2.

- Yelland, M. J., B. I. Moat, P. K. Taylor, R. W. Pascal, J. Hutchings, and V. C. Cornell (1998), Wind stress measurements from the open ocean corrected for airflow distortion by the ship, *J. Phys. Oceanogr.*, *28*, 1511–1526, doi:[http://dx.doi.org/10.1175/1520-0485\(1998\)028<1511:WSMFTO>2.0.CO;2](http://dx.doi.org/10.1175/1520-0485(1998)028<1511:WSMFTO>2.0.CO;2).
- Yelland, M. J., R. W. Pascal, P. K. Taylor, and B. I. Moat (2009), Autoflux: an autonomous system for the direct measurement of the air-sea fluxes of CO₂, heat and momentum, *Journal of Operational Oceanography*, *2*, 15–23.
- Yelland, P. K. T., Margaret (1996), Wind stress measurements from the open ocean, *J. Phys. Oceanogr.*, *26*, 541–558, doi:[http://dx.doi.org/10.1175/1520-0485\(1996\)026<0541:WSMFTO>2.0.CO;2](http://dx.doi.org/10.1175/1520-0485(1996)026<0541:WSMFTO>2.0.CO;2).
- Yuan, R., M. Kang, S.-B. Park, J. Hong, D. Lee, and J. Kim (2010), Expansion of the planar-fit method to estimate flux over complex terrain, *Meteor. Atmos. Phys.*, p. 123–133, doi:10.1007/s00703-010-0113-9.
- Zappa, C. J., W. R. McGillis, P. A. Raymond, J. B. Edson, E. J. Hintsa, H. J. Zemmelen, J. W. H. Dacey, and D. T. Ho (2007), Environmental turbulent mixing controls on air-water gas exchange in marine and aquatic systems, *Geophys. Res. Lett.*, *34*(10), L10,601, doi:10.1029/2006GL028790.

The Last Page

My PhD involved an extraordinary amount of travel, to conferences, experiments and visits to other labs. Especially at the start I spent more time away than in Galway, where I was often greeted with “Welcome back! How long are you going to stay this time?”

I tried to keep track of all these travels during the last four years and four months and summarised them in Fig. 6.1. The total distance travelled are 218,421 km, 2,240 km and 14,215 km, by plane, train and ship, respectively, plus roughly 10,000 km local commuting on five different bikes - all adds up to a sum of 244,877 km, a little less than two thirds of the average distance from the Earth to the Moon (384,400 km). Assuming a passenger contributes 255 g km^{-1} and 30 g km^{-1} to the CO_2 emissions of a flight and train journey, respectively, I estimated my travel related carbon footprint (excluding the cruises) to be $56 \times 10^3 \text{ kg}$. The global annual anthropogenic emissions in 2014 were 40 Pg (Petagram), making my contribution a fraction of 3.2×10^{-10} .

I am grateful for the experiences I had during this time, the people I met and the amazing places that I was able to see.

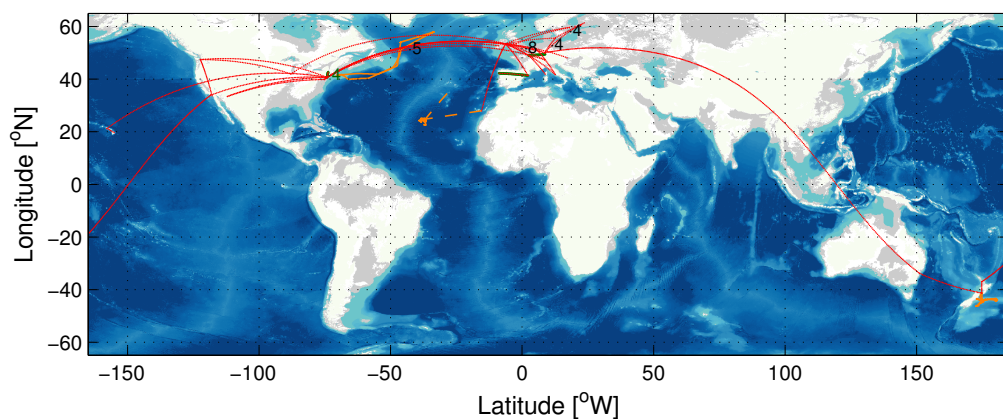


Figure 6.1: Travelling that was involved in this PhD. Flights are marked in red, train rides in green, and cruise tracks in orange, for the MIDAS experiment dashes are used, since I was not on the ship. The numbers indicate routes that I travelled more than twice (return).